Direct Numerical Simulations on Grid-Generated Turbulence

ZHOU Yi

Direct Numerical Simulations on Grid-Generated Turbulence

ZHOU Yi

A thesis presented for the degree of
Doctor of Philosophy

Statistical Fluid Engineering Laboratory

Department of Mechanical Science and Engineering

Nagoya University

2015

DEDICATION

I would like to dedicate this thesis to my mother, Xiaohong Liu and father, Xiaopeng Zhou. They have continuously encouraged me to reach my dream.

I also dedicate this thesis to beloved my wife, Fang Zhou, for her care, understanding, and encouragement during my study at Nagoya University.

Contents

Chapter 1

Introduction

1.1 Background and Objectives

Homogeneous isotropic turbulence (HIT) is probably one of the most critical and extensively investigated turbulence problems and various theories of HIT are proposed by theoretical studies.[1] The term 'isotropic' means that the ensemble average properties of the turbulent flow are independent of the direction. The pioneer investigation of HIT is carried out by Taylor.[2] Based on the assumptions of homogeneity and isotropy, a simple correlation function is obtained, $g = f + 1/2rf'(r)$, where $f(r)$ and $g(r)$ are the longitudinal and lateral velocity functions defined by $f(r) =< u'(r_0 + r)u'(r_0) > / < u'(r_0)^2 >$ and $g(r) = v'(r_0 + r)v'(r_0)/ < v'(r_0)^2 >$, where u' and v' are the longitudinal and lateral fluctuating velocity components, respectively, and r is the longitudinal separation.[3] The definitions of f and g can be seen in Fig. 1.1.

Kolmogorov[4] proposed the famous Kolmogorov's decay laws $u_{rms}^2 \sim t^{-10/7}$, which is based on the Loitsyansky's invariant[5] $I \sim u'^2 l^5$ in isotropic turbulence, where u_{rms} is the root mean square (rms) of the fluctuating longitudinal velocity u' (i.e., $u_{rms} = \sqrt{< u'^2 >}$; $\langle\ \rangle$ denotes ensemble average) and $l = \int_0^\infty f(r)dr$ is the integral length scale. Also, Kolmogorov[6] suggested that at quite large Reynold number Re_λ, $(= \lambda u_{rms}/\nu$, where λ and ν are the Taylor microscale and the kinematic viscosity, respectively), the small-scale statistics are in a locally homogeneous isotropic equilibrium state, which is thought to be universal, where the Taylor microscale λ

is obtained by $\lambda^2 = \langle u'^2 \rangle / \langle (\partial u'/\partial x)^2 \rangle$.

In the past three decades, owning to the rapid development of high performance computer, researchers can carry out numerical simulations of HIT.[7–9] For instance, the DNSs results of Kaneda *et al.*[7] suggested that the energy spectrum in the inertial subrange is quite close to the Kolmogorov $k^{-5/3}$. Also Ishida *et al.*[8] found that the energy decay of HIT follows the well-known Kolmogorov's prediction $u_{rms}^2 \sim t^{-10/7}$. Ishihara[9] performed DNSs of HIT to study the fundamental problem of turbulence; does the dissipation of kinetic energy become zero or remain a finite value when ν approaches zero. Their numerical results strongly supported the hypothesis that the energy dissipation rate remains finite when Re_λ approaches infinity. Note that in the numerical simulations, the periodic boundary conditions are necessary to use the fast Fourier transform (FFT). In the ideal world, the longitudinal correlation $f(r)$ will approach zero at large streamwise separation r, whereas in numerical simulations the profile of $f(r)$ is symmetric. Hence, special attention should be paid when explaining the numerical results, particular those concerning large-scale statistics. Moreover, it is suggested that if the size of the periodic cube L_{box} is less than eight times integral length scale l, ($L_{box} \leq 8l$), the numerical results of large-scale statistics are not meaningful.[10] At last, it should be stressed that in the real world, the perfect HIT can not be found owning to the fact that even the earth itself is finite.

Before the numerical study of Orszag and Patterson,[11] the grid turbulence is the only way to directly obtain the properties of HIT. The usage of regular grid is a more

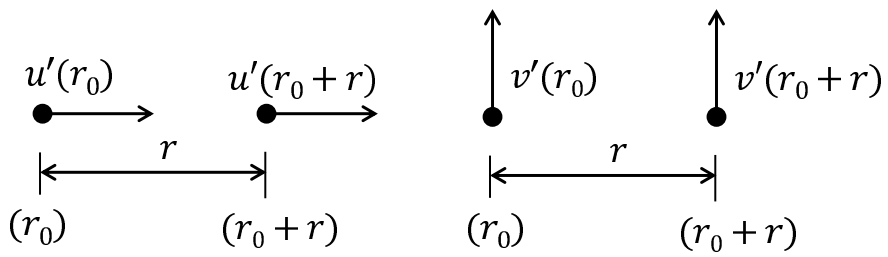

Figure 1.1: The definition of $f(r)$ and $g(r)$. Note that because of homogeneity, $f(r)$ and $g(r)$ are independent of the longitudinal location r_0.

convectional method to generate quasi-homogeneous isotropic turbulence, compared with the numerical simulations of HIT. To increase the validity of the comparison between the grid-generated turbulence and theory estimations of HIT, great effects are made by various researchers. Comte-Bellot and Corrsin[12,13] proposed that the usage of a contraction can improve the isotropy of grid-generated turbulence. Recently, to improve isotropy and reduce sidewall boundary layer effects, Krogstad and Davidson[14] used grid with small meshes and the grid is set upstream of a contraction. Note that even using a contraction section and mounting the grid upstream of the contraction, turbulence behind the regular grid is not perfectly isotropic; u_{rms} is usually 10 percent larger than the rms fluctuations in the other two directs.[12–16]

Immediately behind the grid, wakes and jets can be observed, and in this region the turbulent flow is highly inhomogeneous and the turbulence characteristics highly depend on the grid structures.[12,17,18] In contrast, in the far downstream region, which is approximately homogeneous and the obtained experimental results can be used to compare with theoretical models of homogeneous isotropic turbulence. Corrsin[19] suggested that three requirements should be satisfied to ensure the homogeneity of the grid-generated turbulence. The first one is the value of the blockage ratio σ of the grid. To avoid the large-scale unstable instability of the turbulent flow in the lee of the grid, Tan-Atichat *et al.*[20] suggested that σ should be less than 40%. The second point is that the size of the wind tunnel D should be much larger than the mesh size of the grid M, that is $D/M \gg 1$. For a small D/M, it can be expected the interactions of the wake generated by the grid bar and the solid walls can exert non-negligible influence on the turbulent flow. The third point is that experiment data should be taken in the far downstream location, since reasonable homogeneity can only be obtained in this region ($\geq 40 \sim 50M$). Only simultaneously stratifying the above three conditions, can the numerical results be used to compare with or test theoretical models of HIT. As we shall demonstrate in this thesis, a carefully examination on the previous experimental investigations of the fractal-generated turbulence,[23–27] the latter two conditions are not truthfully fulfilled.

It is interesting to note that only quite recently in 2010 the first direct investigation of the homogeneity of the grid turbulence was carried out by Ertunç *et al.*[21] They suggested that while the inhomogeneity of the mean streamwise velocity U disappear rapidly, the inhomogeneity of the Reynold stresses (e.g., $< u'u' >$ and $< v'v' >$) persist for a much longer distance. Nagata *et al.*[28] investigate the cross-sectional profiles of various turbulence statistics of turbulence generated by the fractal/multiscale grid. Their results are in qualitative agreement with those of Ertunç; that the inhomogeneity of the mean velocity U disappears in the far downstream region and higher order statistics are still inhomogeneous even in the far downstream region. The turbulence energy is effectively transported to the outward region rather than to the central region. In this thesis, we will demonstrate that this inhomogeneity of the fractal-generated turbulence is related to the limited streamwise measurement region.

The above descriptions clearly suggest that considerable care must be taken to ensure reasonable isotropy and homogeneity of the grid-generated turbulence when using the experimental data (e.g., regular or fractal/multiscale grids) to testify the theories of HIT.

To define the inlet condition for the grid-generated turbulence, the dimensionless quantity inlet Reynolds number $Re_{in} = U_{in}M/\nu$ is used, where U_{in} is the inlet mean velocity. To characterize the turbulence flow, previous studies employed the parameters (e.g., root mean square value of streamwise velocity fluctuations u_{rms}, Kolmogorov microscale η, Taylor microscale λ, integral length scale l, and Re_λ). The Kolmogorov microscale η, which is defined by $\eta = (\nu^3/\varepsilon)^{1/4}$ and ε is the kinetic energy dissipation rate per unit mass. The dissipation rate ε is obtained by $\varepsilon = 2\nu \left\langle S'_{ij} S'_{ij} \right\rangle$, where $\langle\ \rangle$ and $'$ denote ensemble average and the fluctuating part of the corresponding variable, respectively. The fluctuating rate of strain S'_{ij} is defined by $S'_{ij} = \frac{1}{2}\left(\partial u'_i/\partial x_j + \partial u'_j/\partial x_i\right)$. The Kolmogorov microscale η is thought to be the smallest length scale in turbulent flow.[22] The integral length scale scale l represent the length of the region, where the velocities are correlated (or the size of the large eddy).[22] The turbulent Reynolds number Re_λ can be interpreted as the ratio of the large-eddy time and the time scale of the strain rate fluctuations.[22]

1.1. Background and Objectives

Recently, the work of Hurst and Vassilicos[23] prompted widespread interest in turbulence generated by multiscale grids. Experimental results[24–28] demonstrated that fractal square grids with relatively low blockage ratio ($\sigma = 25\%$) could produce turbulent flows with unusual properties such as higher levels of intensities u_{rms}/U, and larger values of turbulent Reynolds number Re_λ when compared with those generated by classical/regular grids. For instance, Hurst and Vassilicos[23] demonstrated that for the fractal square grid Re_λ takes the value of approximately 380 at the end of the test section, whereas the corresponding value for the regular grid is much smaller $Re_\lambda \sim 200$ (see Figs. 3 and 38 in their paper). More surprising findings may be the unconventional higher energy decay rates and the approximate constant integral length scales and Taylor microscales in the decay region of the fractal square grid. These unusual behavior does not follow the widely accepted Richardson-Kolmogorov cascade theory.

In this study, we perform the simulations of two turbulent flows (e.g., turbulence generated by the single and fractal square grids). The main objectives of this thesis are as follows:

1. Simulation results of the fractal square grid can directly contribute to the understanding of the fractal-generated turbulence.

2. Previous studies[23–27] suggested that the unusual behaviour of turbulence behind the fractal square grid is related to its multi-scale grid structure; the fractal square grid can produce wakes of different scales. To verify this assumption, we carry out the numerical simulations of the single square grid, as well as the fractal square grid. By comparing the simulation results of the single and fractal square grids, we can estimate the influences of the relatively smaller fractal iterations on the generated turbulence.

3. The present single square grid is a part of the regular grid, which is widely used to generate quasi-homogeneous isotropic turbulence. Moreover, behind the single square and regular grids the wake-interaction patterns are similar. So the numerical investigation of the single-square grid-generated turbulence is also helpful to learn the physical characteristics of the turbulent flow generated by the regular grid, especially in the near-field region.

4. Our research group is now focusing on the mixing rate of multiscale/fractal grids. The numerical findings here can provide insight into the design of high performance industrial devices such as static mixers by using multiscale/fractal grids.

1.2 Single-Square Grid-Generated Turbulence

Since the work of Simmons and Salter,[29] regular grids (i.e., rectangular array of square or cylindrical bars) are widely used to generate quasi-homogeneous isotropic turbulence.[12,14–16,29,30] Probably by now, the usage of regular grid with incoming uniform stream in a contraction tunnel is the simplest way to generate freely decaying homogeneous and isotropic turbulence at large Reynolds number. The investigation of the homogeneous generate quasi-homogeneous isotropic turbulence. turbulence is important. The investigation of grid turbulence is important because the obtained results can provide test for the theory of turbulence, and the data of grid turbulence can contribute to answer the following questions, which are of important role in the theory of turbulence.[10] Here we only list a few: how much does the turbulence remember, the rate of energy destruction in fully developed turbulence, the probability distribution of velocity field (the possibility of closure models), and the energy distribution across the different eddy size (Kolmogorov's theory).

Turbulent flows behind the grid can be roughly divided into two regions. In the near-field of a regular grid, the wakes and jets are observed and they interact with each other. In this region, turbulence is not homogeneous and strongly depends on the structure of the grid. In contrast, in sufficiently far downstream region, turbulence can be regarded as statistically homogeneous. To avoid the effects of the grid bars, in the experiment by Mohamed and LaRue,[30] data at $X \leq 40M$ are eliminated from analysis. Here, X is the streamwise distance from the grid and M is the mesh size for the regular grid. Lavoie *et al.*[15] obtained data at $X \geq 30M$ to investigate turbulence generated by different types of regular grids. Recently, Kitamura *et al.*[16] also investigated turbulence statistics generated by regular grids of different types (square and cylindrical bars) and mesh sizes. To obtain energy

decay exponents, data at $X \geq 50M \sim 60M$ are used in their paper. The boundary between near- and far-fields is blurring and not exactly defined. One consensus for selection data is that at $X \leq 25M$, the regular grids may still have impacts on the fluid motions. Actually, data obtained in this region are seldom used in experimental investigations of regular grid-generated turbulence.

Far downstream turbulence (i.e., at $X \geq 25M$) is extensively studied to explore the characteristics of homogeneous isotropic turbulence (HIT). However, turbulence generations and evolutions just downstream of the grids have not received as much attention as far downstream turbulence. Thus, the characteristics of turbulence in the near-field remain unclear. The single square grid considered in this thesis can be regarded as a special type of regular grid with only one large mesh. In view of this, detailed information on the turbulent flow generated by a single square grid contributes to the understanding of regular grid turbulence in the upstream region. The main difference between the present and all previous studies[12,14–16,29,30] is that particular interest is paid to the turbulent flow in the transition process and the behavior of wake-interactions, which have not been studied before.

The unusual behavior of turbulence behind the fractal square grids is thought to be introduced by the mutiscale wake interactions;[24–26] wakes of the fractal square grid are of different sizes and interact at different streamwise distances depending on the wake pair and wakes of a smaller size interact with neighboring wakes at a shorter distance from the grid and stir turbulence. The interactions furtherest along the centerline are those of wakes generated by the largest grid bars. In this thesis, we perform simulations of the single square and fractal square grids. Note that the largest grid in the fractal square grid is the same size as the singe square grid. The simulations of the singe square grid not only contribute to the understanding of the behaviour of the largest wake interactions but also provide insight into the mutiscale wake interactions (i.e., to clarify the role of the largest wake interactions in mutiscale wake interactions).

Previous studies of grid-generated turbulence mainly focus in the far downstream region (i.e., $X/M \geq 50$), where quasi-homogeneous isotropic turbulence can be found. In contrast, the fractal-generated turbulence are extensively investigated in

the region (i.e., $X/L_0 \leq 14$), where L_0 is the length of the largest grid bar. Note that in our current simulation owning to the limitation of calculation resource, only finite streamwise extent (i.e., $X/L_0 \leq 14$) is possible. Hence, here the numerical results of the single square grid are mainly compared with the experimental results of the fractal square grid.

1.3 Fractal-Generated Turbulence

As mentioned at the very beginning of this chapter, increased attention has been paid to the behavior of turbulence generated by multiscale grids.[17,23–28,31–33] The first ever experiment is performed by Hurst and Vassilicos.[23] They investigated three different families of fractal grids: fractal cross grids, fractal I grids, and fractal square grids. They reported that even with relatively low blockage ratio ($\sigma = 25\%$), fractal square grids produce higher levels of streamwise rms velocity u_{rms} and have unusual larger values of Re_λ than those generated by the regular grids. Moreover, they also demonstrated that for the fractal square grid, the ratio of the integral length scale to the Taylor microscale remains approximately unchanged in the decay region, which is not in accord with the classical Richardson-Kolmogorov cascade theory. Following the study of Hurst and Vassilicos,[23] Seoud and Vassilicos[24] and Mazellier and Vassilicos[25] extensively investigated turbulent flows generated by fractal square grids. Experimental results[24,25] confirmed the findings of Hurst and Vassilicos[23] that unconventional properties could be observed behind the fractal square grid.

Valente and Vassilicos[26] doubled the extent of the decay region and confirmed the persistence of the suppressed Richardon-Kolmogorov cascade for turbulence generated by the fractal square grid. Also, they reported the existence of non-negligible transverse transport of turbulent kinetic energy around the centerline downstream to the very end of the tested region. Gomes-Fernandes *et al.*[27] performed the experimental study in a water tunnel with non-neglibible inlet free-stream turbulence using particle image velocimetry. Their data confirmed previous findings in hot-wire measurements. Nagata *et al.*[28] presented the cross-sectional profiles of various

turbulence statistics to investigate the evolution and decay of fractal-generated turbulence and confirmed the finding of Valente and Vassilicos[26] that the turbulence energy produced in the decay region is efficiently transported to the outward direction, which may introduce the untraditional fast decay of turbulence energy in the central region.

Recent experimental evidence[17,32] has emerged that suggests that turbulent flows generated by the fractal square grid are not as unique as once believed. Krogstad and Davidson,[17,32] for example, have investigated the turbulence generated by two multiscale grids and one regular grid, and they found that the high decay rates of the turbulence energy could be observed in the near field of both grids. However, these remarkably high energy decay rates last for a finite streamwise range. More conventional decay can be recovered within an extended measurement section.

It has also been demonstrated experimentally by Valente and Vassilicos[33] that the nonclassical energy dissipation behavior, found in the lee of the fractal square grid,[24–26] is more general than previously expected. It was shown that at a sufficiently high mesh Reynolds number Re_{in} ($= MU_{in}/\nu$, where M is the mesh size of the regular grid and the mesh size of the largest grid of the fractal square grid) turbulent flows behind all four cases (three regular grids and one fractal square grid) follow a new dissipation law.[24–26,33] Furthermore, Valente and Vassilicos[33] regarded the fractal square grid, which possessed the largest M, as a magnifying lens that caused the high energy decay region to be longer than the total length of the tested tunnel.

Researchers have also carried out DNSs to study the turbulent flows generated by the fractal grids.[34–42] However, owning to present computer limitations, only DNSs of low-Reynolds-number flows are possible. Nagata *et al.*[34,35] numerically investigated flows generated by regular, fractal cross, fractal I, and fractal square grids, at the mesh Reynolds number $Re_{M_{eff}} = 2,500$, which is based on the inflow velocity U_{in} and the effective mesh size M_{eff} proposed by Hurst and Vassilicos.[23] Note that for a regular grid, the effective mesh size is same as the actual mesh size M. They recovered some important characteristics of fractal-generated turbulence. For example, their numerical results indicated that value of Re_λ for turbulence

generated by the fractal square grid in the downstream region is three times larger than the corresponding value of the regular grid. This observation is in qualitative agreement with previous experiment results.[23–25] Using the so-called Incompact 3D numerical strategy, Laizet *et al.*[38–42] also carried out numerical simulations of the fractal square grids and observed both wake-like and jet-like behavior in the lee of the grids.

Note that in addition to these interesting physical properties, fractal grids also have a wide range of practical applications. Both experimental[43,44] and numerical studies[35,36,41] have suggested that fractal structures have a distinctly higher turbulent diffusivity and scalar mixing performance than regular/classical grids, and moreover, Laizet and Vassilicos[41] also demonstrated that the fractal grid greatly enhances scalar mixing with a comparable pressure drop as a regular grid. More recently, Soulopoulos *et al.*[45] showed that when the fractal grid is employed in a burner, there is more intense burning. There are a number of other possible practical applications including flow meters,[46] aircraft spoilers,[47] and fractal fences,[48] and a detailed study of the turbulence generated by the fractal square grid will contribute to the development of such practical applications.

1.4 Outline

This thesis is organized as follows. In chapter 2, numerical details of DNSs and the schematics of the single and fractal square grids are presented. The spatial resolutions for the simulations of the single and fractal square grids are given. In chapter 3, single-square grid-generated turbulence is numerically investigated by means of DNSs. Various turbulence statistical variables (e.g., mean velocity, turbulence intensity, and Taylor microscale, etc.) are obtained. We apply the wake-interaction length scale X_* to the case of the single square grid and confirm the dominant impacts of wakes generated by the square bars in the upstream region (i.e., $X/X_* = 0.2$). We also investigate the spatial development of invariants of the velocity gradient tensor along the centerline. In chapter 4, numerical results of the fractal square grid are obtained. In this chapter, instantaneous streamwise velocity

fields are presented. Our simulation results confirm the existence of the high energy decay region behind the fractal square grid. Also, we show that the use of M_{eff} to characterize the initial mesh Reynolds number for fractal-generated turbulence can be misleading. In chapter 5, an additional simulation, that of turbulence generated by a single square grid subject to additional artificial turbulence, is carried out. With the inclusion of the additional homogeneous isotropic turbulence, the turbulence behind the single square grid has similar characteristics to fractal-generated turbulence. These similarities indicate that the fractal square grid can be regarded as an efficient additional turbulence generator. To make reasonable comparisons, all the simulation cases discussed in this thesis have the same mesh inlet Reynolds number $Re_{in} = L_0 U_{in}/\nu$.

Chapter 2

Numerical Method and Flow Conditions[49,50]

In this chapter, the mathematical model and the numerical methods as well as the schematics of the simulation domain and the single and fractal square grids are given. Following previous experiments, the grid (e.g., single and fractal square grids) is set near the inlet of the domain in the present numerical study. A simple two-dimensional sketch of the geometry can be found in Fig. 2.1 and more detailed descriptions are given in the subsection 2.6.

2.1 Mathematical Model and Numerical Method

The governing equations are the Navier-Stokes and continuity equations for incompressible flows with a constant kinematic viscosity ν:

$$\frac{\partial U_i}{\partial t} + U_j \frac{\partial U_i}{\partial X_j} = -\frac{\partial P}{\partial X_i} + \frac{1}{Re_M} \frac{\partial^2 U_i}{\partial X_j \partial X_j} \tag{2.1.1}$$

and

$$\frac{\partial U_i}{\partial X_i} = 0. \tag{2.1.2}$$

Figure 2.1 shows that the uniform fluid velocity U_{in} is prescribed as the inlet condition in the X-direction. And periodic boundary conditions are adopted in the Y- and Z-directions. By using the periodic boundary conditions, we could avoid the influences of the boundary layers generated by the solid walls in experiments. The

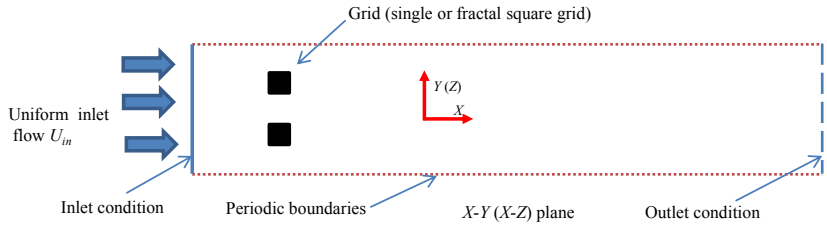

Figure 2.1: Two-dimensional sketch of the geometry. We shall give more detailed descriptions in the subsection 2.6.

following convective outflow condition is used as the outflow boundary condition:

$$\frac{\partial U_i}{\partial t} + U_m \frac{\partial U_i}{\partial X_1} = 0, \tag{2.1.3}$$

where U_m is the convection velocity, which equals to the uniform inlet velocity U_{in}.

The initial velocity fields for all simulation cases are set to $(u_0, v_0, w_0) = (U_{in}, 0, 0)$ everywhere except for the grid bars, just considering a uniform distribution of U_{in} with no fluctuations, where u_0, v_0, and w_0 denote the initial velocity components in the streamwise, vertical, and spanwise directions, respectively.

Numerical simulations for the single and fractal square grids are carried out with 131,072,000 grid points (1280×320×320, in the X-, Y-, and Z-directions). In this numerical study, the rectangular region and Cartesian coordinate are used. The normalized domain sizes by the length of the largest grid bar L_0 in the X-, Y-, and Z-directions are $14L_0$, $2L_0$, and $2L_0$, respectively. We examine the Kolmogorov microscale η, which is defined by $\eta = (\nu^3/\varepsilon)^{1/4}$ and ε is the kinetic energy dissipation rate per unit mass. The dissipation rate ε is obtained by $\varepsilon = 2\nu \left\langle S'_{ij} S'_{ij} \right\rangle$. In experimental studies,[16,26,28] to estimate ε the usage of isotropic hypothesis is necessary. In the present simulations, we obtain the energy dissipation rate without any assumptions. The streamwise evolution of η along the centerline for both grids is shown in Fig. 2.2. For the single square grid, the worst spatial resolution along the centerline is $(\Delta X \Delta Y \Delta Z)^{1/3} \simeq 2.7\eta$, whereas it is $(\Delta X \Delta Y \Delta Z)^{1/3} \simeq 1.6\eta$ at $X/X_* = 1.4$ $(X/L_0 = 13.16)$. For the fractal square grid, the worst spatial resolution is $(\Delta X \Delta Y \Delta Z)^{1/3} \simeq 8\eta$, whereas it is $(\Delta X \Delta Y \Delta Z)^{1/3} \simeq 1.8\eta$ at $X/X_* = 1.4$ $(X/L_0 = 13.16)$. Here, ΔX, ΔY, and ΔZ denote the grid spacings in the streamwise, vertical, and spanwise directions, respectively. The time step is 0.00134 L_0/U_{in}

and averages are taken over 110,000 time steps to obtain converged statistics (e.g., U, u_{rms}/U, λ, Re_λ, etc). Note that owing to the complexity of the turbulent flows, it is difficult for us to propose a simple criterion to judge whether the averaging time is sufficient or not. Here, total averaging time contains more than eight travelling periods. One travelling period is the number of time steps for a fluid point to move from the inlet to the outlet based on the mean velocity. And we confirm that after six periods, the numerical results remain approximately unchanged.

A three-step Runge-Kutta scheme is used for time integration. The fourth-order central difference scheme proposed by Morinishi *et al.*[51] is used for the convective terms. Eighth-order central compact scheme[53] is used for the viscous terms along the X-direction, and Fourier spectral method for the Y- and Z-directions. Note that around the grid owning to the non-uniform mesh arrangement, the approximation of the viscous terms in the streamwise direction, is not eighth order. We shall return to this subject in the subsection 2.4. The resulting Poisson equation for pressure is solved by using a tridiagonal matrix solver in the X-direction and a discrete Fourier transform in two other periodic directions. The mass conservation is ensured up to the machine accuracy ($\sim 10^{-14}$). In this study, we use the numerical scheme proposed by Nagata *et al.*[34,35] and Suzuki *et al.*[36] In this subsection, we just briefly introduce the numerical method. More detailed descriptions can be found in the following subsections. The high accuracy of the numerical method used here is extensively discussed by Nagata *et al.*[35] and Suzuki *et al.*[54]

2.2 Runge-Kutta and Fractal Step Method

The time advancement scheme for Eqs. (2.1.1) and (2.1.2) can be written as[55]

$$\frac{U_i^F - U_i^{F-1}}{\Delta t} = -\alpha_F L(U_i^{F-1}) - \beta_F L(U_i^{F-2}) - \gamma_F N(U_i^{F-1}) - \zeta_F N(U_i^{F-2}) + (\alpha_F + \beta_F)\frac{\delta P^F}{\delta X_i} \tag{2.2.4}$$

and

$$\frac{\delta U_i^F}{\delta X_i} = 0, \tag{2.2.5}$$

where $F = 1, 2, 3$ means number of the substep, U_i^0 and U_i^3 denote the instantaneous velocities at step n and $n+1$, and $L(U_i)$ and $N(U_i)$ are the discretization

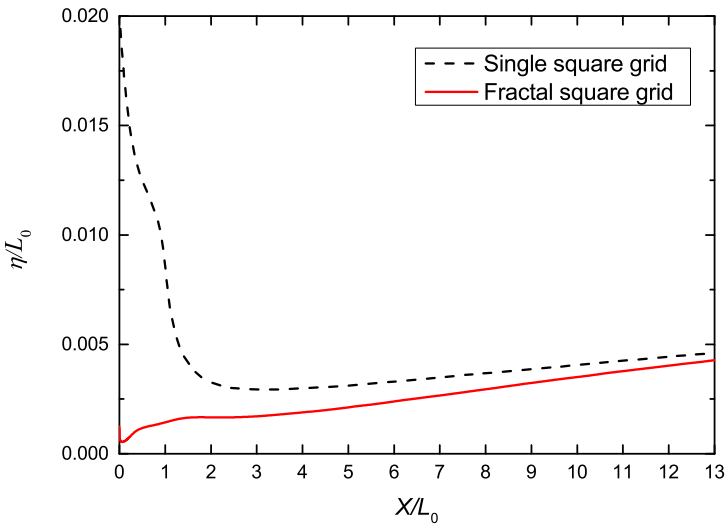

Figure 2.2: Streamwise evolution of the normalized Kolmogorov microscale η/L_0 along the centerline.

approximations for the viscous and convection terms. Throughout this thesis, $\delta/\delta X_i$ is the finite difference operator. Note that for Eqs. (2.2.4) – (2.2.8) the subscripts i (=1, 2, and 3) refer to qualities in the streamwise, vertical, and spanwise directions, respectively. It can be seen from Eq. (2.2.4) that the viscous and convection terms are all treated explicitly to avoid iteration calculation. The values of the coefficients α_F, β_F, γ_F, and ζ_F in Eq. (2.2.4) are listed in Table 2.2.

TABLE 2.2. Values of coefficients α_F, β_F, γ_F, and ζ_F.

sub-step F	α_F	β_F	γ_F	ζ_F
1	8/15	0	8/15	0
2	5/12	-17/60	5/12	-17/60
3	3/4	-5/12	3/4	-5/12

Mass conservation constrain is enforced at every substep $F = 1, 2, 3$ in Eq. (2.2.4). And the following three equations are solved to obtain the velocity and pressure fields.

$$\frac{\hat{U}_i^F - U_i^{F-1}}{\Delta t} = -\alpha_F L(U_i^{F-1}) - \beta_F L(U_i^{F-2}) - \gamma_F N(U_i^{F-1}) - \zeta_F(U_i^{F-2}), \quad (2.2.6)$$

$$\frac{U_i^F - \hat{U}_i^F}{\Delta t} = (\alpha_F + \beta_F)\frac{\delta P^F}{\delta X_i}, \quad (2.2.7)$$

and the Poisson equation for pressure term

$$\frac{1}{\Delta t}\frac{\delta \hat{U}_i^{\,F}}{\delta X_i} = -(\alpha_F + \beta_F)\frac{\delta^2 P^F}{\delta X_i \delta X_i}, \tag{2.2.8}$$

where $\hat{U}_i^{\,F}$ denote the intermediate velocities at the substep F. To solve the resulting discrete Poisson equation (Eq. (2.2.8)), in the periodic boundary conditions (i.e., vertical and spanwise directions) fast Fourier transform are used, whereas in the streamwise direction, the high efficient tridiagonal matrix solver is adopted. In Eqs. (2.2.9) – (2.2.11) the subscripts i, j, and k refer to the streamwise, vertical, and spanwise locations of $P(i, j, k)$. For a pressure point $P(i, j, k)$, $\tilde{\Delta} X_i$ denote the mesh space in the streamwise direction (see Fig. 2.3). ΔY and ΔZ also follow the same definition rule. Note that the subscript in Eqs. (2.2.9)–(2.2.11) does not follow the summation convention. The fourth order central different scheme is adopted to approximate the right side of Eq. (2.2.8) in the periodic directions (i.e., vertical and spanwise directions):

$$\frac{\delta^2 P}{\delta Y \delta Y} = \frac{P_{j-3} - 54P_{j-2} + 783P_{j-1} - 1460P_j + 783P_{j+1} - 54P_{j+2} + P_{j+3}}{576\Delta Y^2} \tag{2.2.9}$$

and

$$\frac{\delta^2 P}{\delta Z \delta Z} = \frac{P_{k-3} - 54P_{k-2} + 783P_{k-1} - 1460P_k + 783P_{k+1} - 54P_{k+2} + P_{k+3}}{576\Delta Z^2} \tag{2.2.10}$$

In the streamwise direction, a non-uniform mesh scheme is adopted and the second order central difference scheme is applied in the streamwise direction:

$$\frac{\delta^2 P}{\delta X \delta X} = \frac{\frac{P_{i+1}-P_i}{\tilde{\Delta} X_i} - \frac{P_i - P_{i-1}}{\tilde{\Delta} X_{i-1}}}{\frac{\tilde{\Delta} X_i + \tilde{\Delta} X_{i-1}}{2}}. \tag{2.2.11}$$

Note that the usage of the pressure P in the fractal step method is to enforce continuity; in other words, P is more likely to be a mathematical agency. Here, we

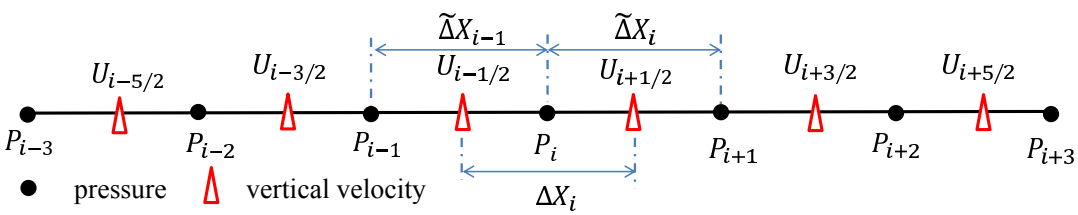

Figure 2.3: One-dimensional grid arrangement in the streamwise direction.

only present the derivation for the one-dimensional case (i.e., in the vertical direction and see Fig. 2.4). The first derivative of P with fourth-order accuracy at substep F is

$$(\frac{\delta P^F}{\delta Y})_{j+1/2} = \frac{P^F_{j-1} - 27P^F_j + 27P^F_{j+1} - P^F_{j+2}}{24\Delta Y}. \tag{2.2.12}$$

The corresponding second derivative of P is

$$\begin{aligned}(\frac{\delta^2 P^F}{\delta Y \delta Y})_j &= \frac{(\frac{\delta P^F}{\delta Y})_{j-3/2} - 27(\frac{\delta P^F}{\delta Y})_{j-1/2} + 27(\frac{\delta P^F}{\delta Y})_{j+1/2} - (\frac{\delta P^F}{\delta Y})_{j+3/2}}{24\Delta Y} \\ &= \frac{P^F_{j-3} - 54P^F_{j-2} + 783P^F_{j-1} - 1460P^F_j + 783P^F_{j+1} - 54P^F_{j+2} + P^F_{j+3}}{576\Delta Y^2}.\end{aligned} \tag{2.2.13}$$

And the discretization expression for the Poisson equation Eq. (2.2.8) becomes

$$\begin{aligned}(\alpha_F + \beta_F)&\frac{P^F_{j-3} - 54P^F_{j-2} + 783P^F_{j-1} - 1460P^F_j + 783P^F_{j+1} - 54P^F_{j+2} + P^F_{j+3}}{576\Delta Y^2} \\ &= -\frac{1}{\Delta t}\frac{\hat{V}^F_{j-3/2} - 27\hat{V}^F_{j-1/2} + 27\hat{V}^F_{j+1/2} - \hat{V}^F_{j+3/2}}{24\Delta Y}.\end{aligned} \tag{2.2.14}$$

Based on the values of P^F_j and $\hat{V}^F_{j+1/2}$, the following equation

$$V^F_j = \Delta t(\alpha_F + \beta_F)\frac{P^F_{j-1} - 27P^F_j + 27P^F_{j+1} - P^F_{j+2}}{24\Delta Y} + \hat{V}^F_j \tag{2.2.15}$$

is used to obtain the velocity field at the substep F. It should be stressed that following the above numerical treatment, the mass conservation for the fourth-order discretization equation at the substep F

$$(\frac{\delta V^F}{\delta Y})_j = \frac{V^F_{j-3/2} - 27V^F_{j-1/2} + 27V^F_{j+1/2} - V^F_{j+3/2}}{24\Delta Y} = 0 \tag{2.2.16}$$

is strictly satisfied ($\sim O^{-14}$). This is why we use Eqs. (2.2.9) – (2.2.11) to approximate the pressure term. It is easy to obtain the derivation for a more complex case (i.e., three-dimensional one).

The pressure P is a periodic function in the vertical and spanwise directions. By using the fast Fourier transform, taking the vertical direction (i.e., the vertical location is represented by the subscript j) for instance it becomes

$$P_j = \sum_{k=1}^{M-1} \hat{P}_k(\cos(\frac{\pi kj}{M}) + \sqrt{-1}\sin(\frac{\pi kj}{M})) \qquad k = 1, 2...., M-1, \tag{2.2.17}$$

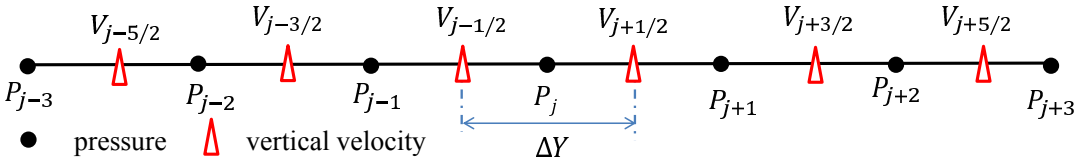

Figure 2.4: One-dimensional grid arrangement in the vertical direction.

where $\hat{P}_k$ is the coefficient corresponding to the wavernumber k. If substituting the sine and cosine series of P into Eq. (2.2.9), it becomes

$$\begin{aligned}\frac{\delta^2 P}{\delta Y \delta Y} &= \frac{1}{288\Delta Y^2}(-730 + 783\cos(\frac{\pi j}{M}) - 54\cos(\frac{2\pi j}{M}) + \cos(\frac{3\pi j}{M}))P_j \\ &= \frac{1}{288\Delta Y^2}(-730 + 783\cos(\frac{\pi j}{M}) - 54\cos(\frac{2\pi j}{M}) + \cos(\frac{3\pi j}{M})) \\ &\qquad (\sum_{k=1}^{M-1} \hat{P}_k(\cos(\frac{\pi k j}{M}) + \sqrt{-1}\sin(\frac{\pi k j}{M}))).\end{aligned} \tag{2.2.18}$$

We can also substitute the sine and cosine series of P into Eq.(2.2.10) (i.e, in the spanwise direction), and then apply two-dimensional FFT transform to left-hand side of the Poisson equation Eq. (2.2.8). Based on the discrete orthogonality property of the sines and cosines, we obtain a tridiagonal system of the coefficients $\hat{P}$ in the steamwise direction, which can be easily solved. After that, the pressure field P is obtain by the inverse two-dimensional FFT transform along the centerline. The above mentioned method is a high efficient way to solve the Possion equation with uniformly distributed mesh arrangement in two periodic directions.[56]

2.3 Difference Scheme for Convective Terms

Previous studies[51,52] stated that discretization equations for convective terms can be expressed in the following three different forms:

$$\text{Advective form:} \quad U_j \frac{\partial U_i}{\partial X_j}, \tag{2.3.19}$$

$$\text{Divergence form:} \quad \frac{\partial U_j U_i}{\partial X_j}, \tag{2.3.20}$$

and

$$\text{Skew-symmetric form:} \quad \frac{1}{2} U_j \frac{\partial U_i}{\partial X_j} + \frac{1}{2}\frac{\partial U_j U_i}{\partial X_j}. \tag{2.3.21}$$

Note that the non-uniform mesh scheme is adopted in the X-direction. To increase the conservation properties of the difference scheme, in the present study, an enhanced approximation scheme based on local Jacobian transformation[52] is employed. And two different domains are used, which are the physical and computational domains (i.e., (X, Y) and (ξ, ζ)), respectively. The computational domain corresponds to a uniform staggered grid arrangement. We take the two-dimensional plane for instance and see Fig. 2.5 for the arrangement of the staggered grid system. The Jacobian operator at the cell center (also pressure point) is $J_{i,j} = \Delta X_i \Delta Y$, and at the cell boundaries (also velocity points) $J_{i+\frac{1}{2},j} = \tilde{\Delta} X_i \Delta Y$ are $J_{i,j+\frac{1}{2}} = \Delta X_i \Delta Y$. To approximate convective terms, we use the following enhanced divergence form

$$\frac{\partial U_j U_i}{\partial X_j} = \frac{1}{J} \frac{\partial J \tilde{U}_j U_i}{\partial \zeta}, \tag{2.3.22}$$

where $J\tilde{U}$ is the inverse Jacobian transformation from the computational domain to physical domain. Good conservation property of kinetic energy can be guaranteed based on the above mentioned numerical scheme.

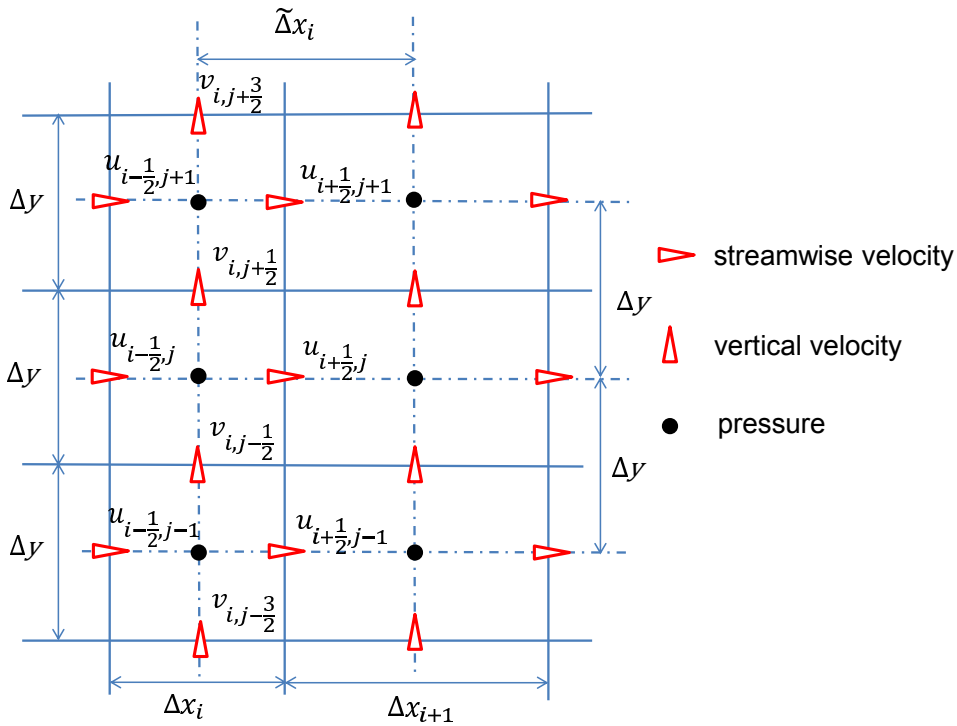

Figure 2.5: Staggered grid system.

2.4 Central Compact Scheme

Based on the well-known Padé differentiation, Lele[53] proposed a family of the finite difference schemes: the so-called central compact scheme (CCS). Central compact scheme is a implicitly discretization scheme with spectral-like resolution. Nagata *et al*[35] and Suzuki *et al*[54] have already confirmed that using the central compact scheme to discretize the viscous terms in the case of the fully developed turbulent channel flow leads to more accurate numerical results compared with using the common central difference scheme. Here, the following eighth order CCS defined on a cell-entered mesh is used for the approximation of the viscous terms in the streamwise direction,

$$\alpha f'_{i-1} + f'_i + \alpha f'_{i+1} = a\frac{-f_{i-1/2} + f_{i+1/2}}{\Delta f_i} + b\frac{-f_{i-3/2} + f_{i+3/2}}{3\Delta f_i} + c\frac{-f_{i-5/2} + f_{i+5/2}}{5\Delta f_i} \tag{2.4.23}$$

and

$$\alpha f''_{i-1/2} + f''_{i+1/2} + \alpha f''_{i+3/2} = a\frac{-f'_i + f'_{i+1}}{\tilde{\Delta} f_i} + b\frac{-f'_{i-1} + f'_{i+2}}{3\tilde{\Delta} f_i} + c\frac{-f'_{i-2} + f'_{i+3}}{5\tilde{\Delta} f_i}, \tag{2.4.24}$$

where $f_{i+1/2}$ denote the variables to be discretized located at node $(i+1/2)$, f'_i and $f''_{i+1/2}$ mean the first and second derivatives of f at the corresponding mesh points, respectively. Note that Δf_i is mesh space between the node $(i-1/2)$ and the node $(i+1/2)$ and $\tilde{\Delta} f_i$ is mesh space between the node (i) and the node $(i+1)$ (see Fig. 2.6). The staggered grid arrangement is adopted in this study. For u, Δf_i and $\tilde{\Delta} f_i$, respectively, denote ΔX_i and $\tilde{\Delta} X_i$, whereas for v (or w), Δf_i and $\tilde{\Delta} f_i$ equal to ΔY (or ΔZ) (see Figs. 2.5 and 2.6). In this study, by concentrating the grid points around the grids (i.e., $X/X_* \leq 0.07$), spatial resolutions around the grids are

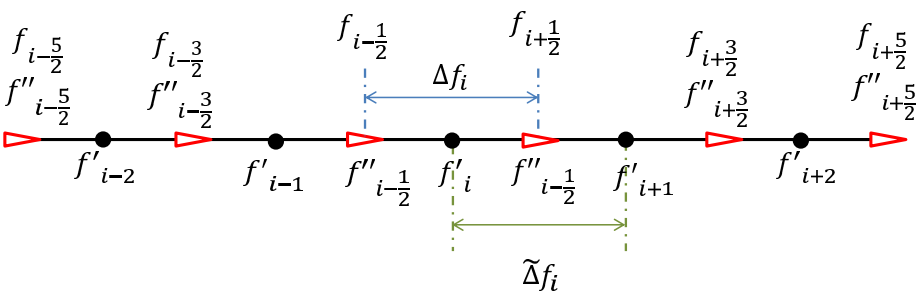

Figure 2.6: Mesh arrangement for the CCS.

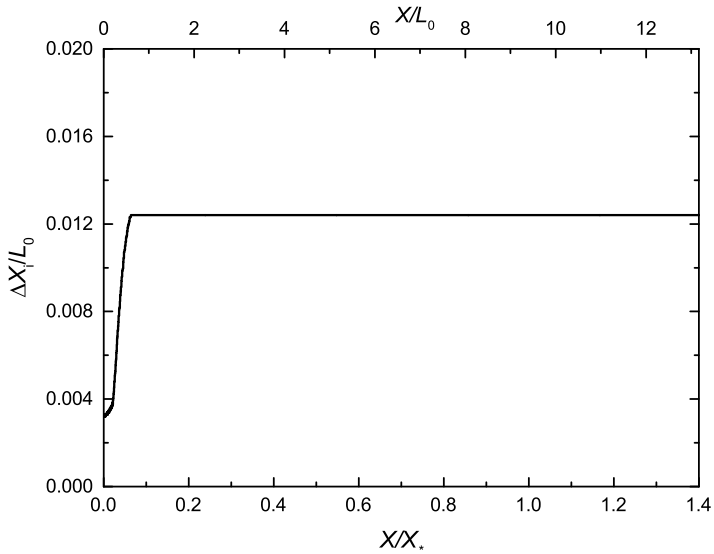

Figure 2.7: Streamwise evolution of ΔX_i in the streamwise direction. For the definition of ΔX_i, refer to Fig. 2.3.

enhanced (see Fig. 2.7). The values of the coefficients α, a, b, and c in the above two equations are listed in Table 2.3. When the constant coefficients α, a, b, and c are used, for the viscous terms, only in the uniform grid region ($X/X_* > 0.07$) the accuracy of Eqs. (2.4.22) and (2.4.23) is eighth order. In contrast, in the lee of the grid (i.e., $X/X_* \leq 0.07$) by using Eqs. (2.4.22) and (2.4.23) the order of the discretisation is lower.

Quite recently, Laizet *et al.*[57] also numerically investigated the single-square grid-generated turbulence, with particular interest in the influence of the spatial resolution on the shape of the joint PDFs of R and Q (the third and second invariants of the velocity gradient tensor). In their study, the so-call Incompact3d solver[38,40] was used. They demonstrated that under different spatial resolutions, the corrsponding profiles of u_{rms} and Re_λ are quite similar. In contrast, the joint PDFs of R and Q strongly depend on the spatial resolution. The joint PDFs of R and Q corresponding to the best resolution obtained by Laizet *et al.*[57] are in good accord with the ones (including those at $X/X_* \leq 0.07$) in our study. Hence, we expect that the lower order of the viscous terms in the region $X/X_* \leq 0.07$ will not significantly influence the accuracy of this simulation. To calculate viscous terms in

TABLE 2.3. Coefficients of the eighth order CCS.

Eighth order	α	a	b	c
Value	$\frac{75}{354}$	$\frac{37950-39275\alpha}{31368}$	$\frac{65115\alpha-3550}{20912}$	$\frac{25669\alpha-6114}{62736}$

the streamwise direction, Eqs. (2.4.22) and (2.4.23) are solved successively to obtain the second derivatives. Note that in the vertical and spanwise directions, periodic boundary condition is adopted for all variables. Hence, the viscous term in the vertical and spanwise directions can be easily approximated by the Fourier spectral method. In this study, DNSs are performed by using the supercomputer NEC SX-9 at the Advanced Fluid Information Research Center, Institute of Fluid Science, Tohoku University. Hence, the FFT libraries (i.e., asl_fft_real) provided by NEC are directly used to realize two-dimensional real-complex/complex-real transforms.

2.5 Grid Arrangement

In this study, fully staggered arrangement is adopted to avoid the possible oscillations in pressure term (see Fig. 2.8). Figure 2.8 shows that the pressure points are directly defined on the grid surface. The pressure on the grid bar can be directly obtained from solving the pressure Passion equation without interpolation. And the velocity points are mostly directly defined on the grid bar to guarantee the nonslip condition of the solid grid bars.

To investigate the dependence of the grid numbers on the faithful generation of the wakes, Nagata *et al*[35] performed three tests. Figure 2.9 shows that they carried out three simulations (using two, three, and five mesh points) to test the arrangement of the grid bar. When using three or five mesh points to arrange the smallest grid bar, the obtained energy spectra of the streamwise and vertical velocity are similar. However, significantly different energy spectra is obtained for smaller mesh number arrangement (i.e., the test of using two mesh points). Hence, they demonstrated that at least three mesh points are required in the Y- and Z-directions of a grid bar to accurately produce the wakes of the smallest grid bar. Note that for the smallest grid bar, the grid armament is the worst situation. More grid points are used to define a larger grid bar.

To investigate flat-plate boundary layer or turbulent channel flow, special attention should be given to the resolution of the near-wall boundary layer (i.e., viscous sublayer). For instance, in a recent numerical study of the flat-plate boundary layer performed by Wu and Moin,[58] there are 10 grid mesh points below $Y_+ = 5$ (viscous sublayer). However, owning to the limitation of current calculation resource, we could not resolve the boundary layer on the grid bar. Instead, Nagata *et al.*[35] have confirmed that the wakes produced by the smallest grid element of the fractal grid are properly reproduced based on current numerical scheme and resolution. Since the main objective of this thesis is to investigate the characteristics of turbulence because of multi-scale wake-interactions, our DNSs simulations are reliable.

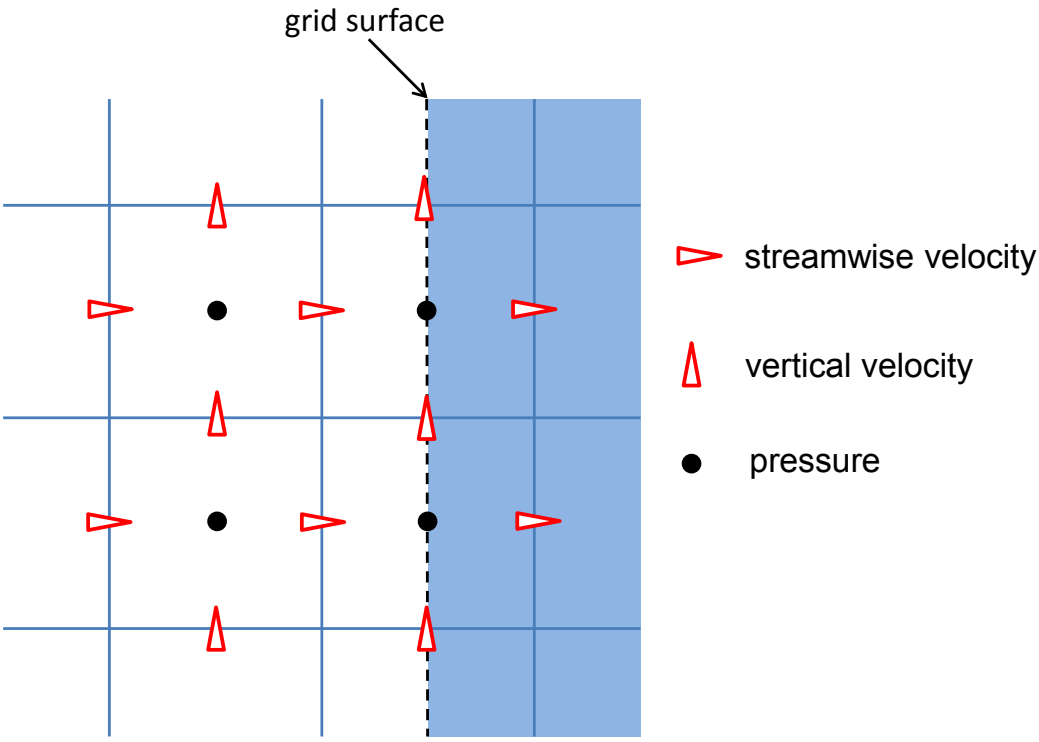

Figure 2.8: Example of the grid surface.

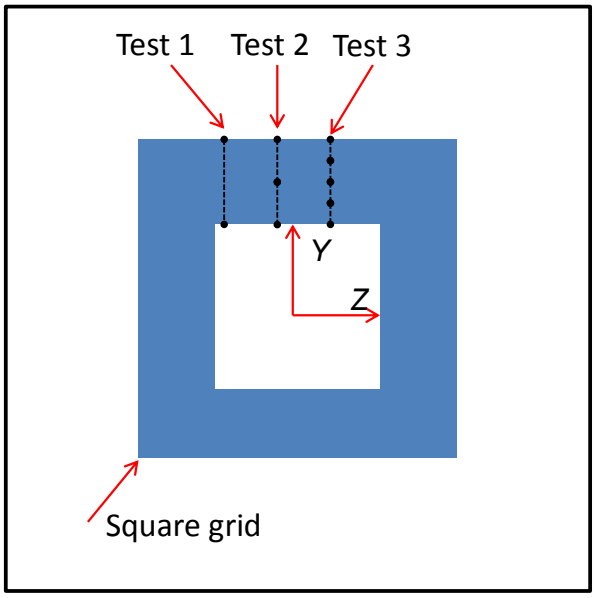

Figure 2.9: Three tests to confirm the independence of grid numbers on wakes.

2.6 Computational Domain and Grid Geometries

The schematic of the computational domain is displayed in Fig. 2.10. The coordinates X, Y, and Z denote the sreamwise, vertical, and spanwise directions, respectively. The origin is placed at the center of the grid. Figure 2.11 shows the schematics of the two grids (the single and fractal square grids), which are placed at $X = 0.04L_X$ from the inlet of the computational domain. Our simulations confirmed that the streamwise separation $0.04L_X$ between the inlet of the domain and the location of the grid will not influence the generated wakes. To make a reasonable comparison, the largest grid in the fractal square grid is the same size as the single square grid; in other words, if we remove the smaller grid iterations of the fractal square grid, the largest remaining element is the single square grid. In this thesis, for grid bar of all scales, the longitudinal (i.e., streamwise direction) thickness is the same as the lateral (i.e., cross-stream direction) one.

Table 2.1 lists the main parameters of the geometries of the single and fractal square grids. Note that the geometry of the fractal square grid is slightly different from that employed in previous experiments.[23–28] In Table 2.1, N is the number of fractal iterations, D_f is the fractal dimension, σ is the blockage ratio, and t_r is the ratio of the thicknesses of the biggest and smallest grid bars. L_0 and t_0 denote, respectively, the length and thickness of the biggest square bars. The inlet Reynolds number Re_{L_0}, which is based on L_0 and U_{in}, is 20,000 in both cases.

The effective mesh size M_{eff}[23] is defined as

$$M_{eff} = \frac{4T^2}{P}\sqrt{1-\sigma}, \tag{2.6.1}$$

where T^2 is the area of the cross section and P is the perimeter. A detailed discussion of M_{eff} will be presented in chapter 4.

TABLE 2.1. Computational conditions and grid parameters.

Grid	Single square[49]	Fractal square[50]
N	1	4
D_f	×	2
t_r	×	8.5
M_{eff} (mm)	×	10
σ	0.11	0.36
L_0(mm)	80	80
t_0/L_0	0.11	0.11
L_X/L_0	14	14
L_Y/L_0	2	2
L_Z/L_0	2	2
U_{in}(m/s)	3.75	3.75
Re_{L_0}	20,000	20,000

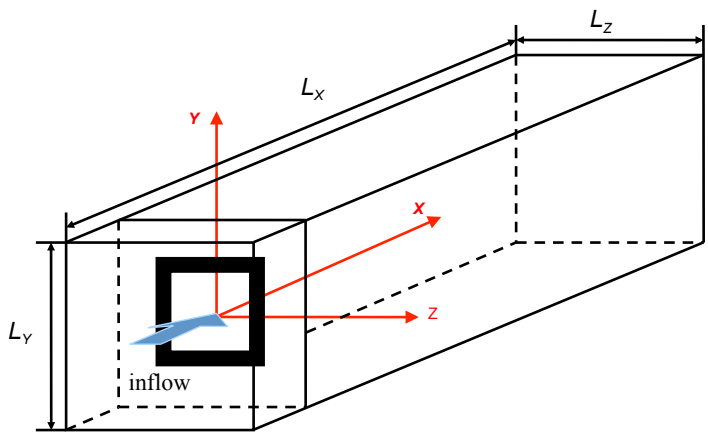

Figure 2.10: Schematic view of the computational domain.

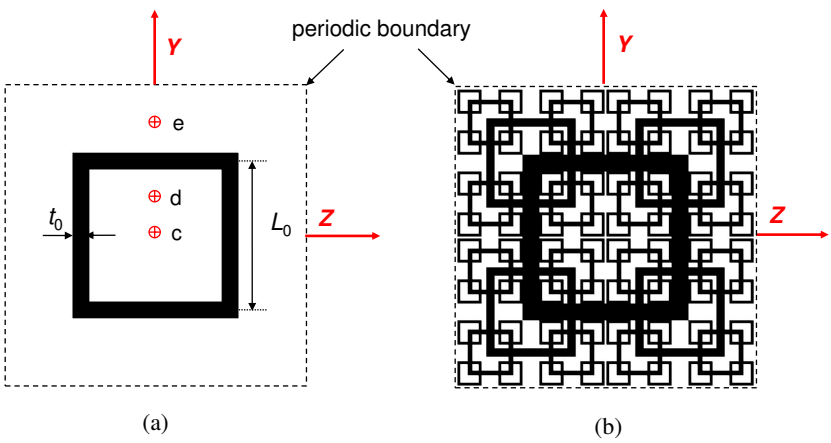

Figure 2.11: Scaled schematics of the two grids used in this thesis. (a) single square grid, (b) fractal square grid. The dotted lines represent periodic boundary conditions in the Y- and Z-directions. In Fig. 3.10, the intermittent factors are evaluated along straight lines, which are parallel to the flow direction and cut the grid plane at points c, d, and e.

Chapter 3

Single-Square Grid-Generated Turbulence[49,50]

In this chapter, the numerical results of the single square grid are presented. Some results are compared with the corresponding data obtained from previous experimental investigations using the regular and fractal square grids. Note that only a few data can be found in previous literature on the regular grid turbulence in the upstream region (i.e., $X/L_0 \leq 14$). As we shall demonstrate in the following sections, the turbulent flow generated by the single square grid indeed possesses some interesting similar characteristics to those generated by the regular and fractal square grids.

3.1 Wake-Interaction Length Scale

The existence of an extended production region was once regarded as one of the most striking characteristics of fractal-generated turbulence.[23,25,40] To evaluate the extent of the production region, where turbulence intensities continuously build up, Mazellier and Vassilicos[25] firstly proposed the wake-interaction length scale X_*. First, they made an important assumption that the influences of the wakes generated by the largest grid bar are dominant. Moreover, Mazellier and Vassilicos, following Townsend,[59] assumed that the evolutions of the half width b of the largest wake follow a $(t_0X)^{1/2}$ power law. Based on the above two hypotheses, they firstly

introduced the wake-interaction length scale X_* to estimate where the largest wakes meets. The wake-interaction length scale X_* is defined as

$$X_* = \frac{L_0^2}{t_0}. \tag{3.1.1}$$

Mazellier and Vassilicos presented that extreme decelerating flow events occur at $X \simeq 0.2X_*$, which is different from the peak intensity location ($X_{peak} \simeq 0.45X_*$). In their paper, however, the explanation for the extreme and intensive events at $X \simeq 0.2X_*$ is not given. The agreement of the skewness and flatness at $X \simeq 0.2X_*$ for various fractal square grid sizes and inlet mean velocities is not trivial because according to Eq. (3.1.1), the wake-interaction length scale is only determined by the largest grid bar. One possible suggestion is that turbulence motions at $X \simeq 0.2X_*$ along the centerline strongly depend on the characteristic of the largest wake interactions. Note that the wake-interaction length scale X_* is widely used to explore the unusual properties of fractal square grid's turbulence.[25,26,28,33] However, the validity of the assumption made by Mazellier and Vassilicos[25] has not been strictly tested and the evolution and decay of large wake interactions remains obscure.

In this thesis, the streamwise distance from both grids (single and fractal square grids) X is non-dimensionalized by the wake-interaction length scale X_* and also by the length of the largest grid bars L_0.

3.2 Flow Visualization

Figure 3.1 shows the instantaneous streamwise velocity field in the X–Y plane at $Z = 0$ for turbulent flow generated by the single square grid. The red color corresponds to a high value of streamwise velocity ($\geq 1.3U_{in}$) and blue one to a small value (≤ 0), respectively. The flow field is highly inhomogeneous and sheared in the near grid region and the homogeneity increases with the development of turbulent flow due to turbulent diffusion. Both jet-like and wake-like behavior can be found in Fig. 3.1. Two large-scale wakes generated by the grid bars are effectively transported to the outward direction instead of moving parallel to the streamwise direction. Laizet *et al.*[40] also reported a similar mean flow away from the centerline in turbulence generated by the fractal square grid. As we shall present later, the

outward direction movement in Fig. 3.1 is associated with the evolution of turbulent jet located at the central region of the computational domain.

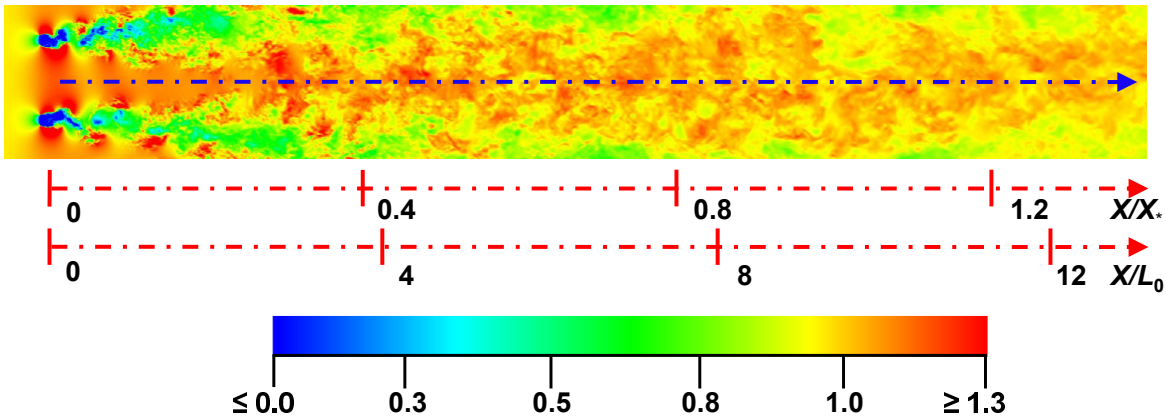

Figure 3.1: Instantaneous streamwise velocity u, normalized by the inflow velocity U_{in}. The red color corresponds to $\geq 1.3U_{in}$ and the blue one to ≤ 0.

3.3 Centerline Statistics

Here, we report on streamwise evolutions of various statistics (e.g., mean velocity U, Taylor microscale λ, and turbulence Reynolds number Re_λ, etc.) for the single square grid along the centerline.

3.3.1 Mean Sreamwise Velocity Profile and Turbulence Intensity

Figure 3.2 shows the streamwise evolution of the normalized mean velocity U/U_{in} along the centerline. Previous studies[25,28] suggested that for fractal–generated turbulence the mean velocity U possesses a plateau in the region $0.10 \leq X/X_* \leq 0.20$ ($0.94 \leq X/L_0 \leq 1.88$). Here, in Fig. 3.2, U also has a plateau at roughly the same region as the fractal square grid, beyond which U starts to decrease (see shaded area in Fig. 3.2). We shall see later, this plateau–like profile for U is due to the obtaining of the classical mean velocity distributions as found in conventional jets. In the downstream region $X/X_* \geq 0.45$ ($X/L_0 \geq 4.23$), the value of U/U_{in} is in the range of 1.06–1.10. This relatively large ratio is consistent with the persistence of jet–like behavior to the furthermost downstream location as shown in Fig. 3.1.

Figure 3.2 also shows the streamwise distribution of the turbulence intensity u_{rms}/U along the centerline. The existence of an extended production region was once regarded as one of the most striking characteristics for fractal-generated turbulence.[23,25,40] Here, we also observe a similar protracted production region. This result is not surprising considering the assumption made by Mazellier and Vassilicos.[25] For the single square grid, the intensity u_{rms}/U reaches its maximum value at the peak point $X_{peak} \simeq 0.45X_*$ and then it begins to decrease. Data from experimental studies[23,25,28] suggested the corresponding peak location for fractal square grids with four fractal iterations locates at $X_{peak} \simeq 0.45X_*$. The agreement of these two peak locations is consistent with the hypothesis proposed by Mazellier and Vassilicos[25] that the value of X_{peak} is mainly determined by the geometry of the largest grid bar. However, we must stress that the exactly the same values of X_{peak}/X_* for the fractal square grid with 4 interactions and the single square grid are more likely

to be a coincidence. Other geometric factors (e.g., blockage ratio σ, number of fractal iterations N, and thickness ratio t_r) may also affect the value of X_{peak}/X_*. A further comparison concerning X_{peak}/X_* for the single and fractal square grids will be presented in chapter 4 of this thesis.

For reference, we also plot u_{rms}/U in previous studies on regular grid turbulence at $Re_M = 2,500$[60], $Re_M = 5,000$[61], and $Re_M = 115,000$[62] in Fig. 3.2. It can be seen that in the decay region close to the grid ($6 \leq X/M, X/L_0 \leq 12$), the profile of the present DNSs for the single square grid is similar to those for previous experimental data for the regular grid[60–62] regardless of different inlet Reynolds numbers and grid patterns. This observation is not surprising because the present single square grid is a part of the regular grid, as mentioned before.

3.3.2 Taylor Microscale and Turbulent Reynolds Number

Figure 3.3 shows the streamwise evolution of the normalized Taylor microscale λ/L_0 along the centerline. Previous experiments[23,25,28] have shown that λ remains approximately constant during decay in high Reynolds number fractal-generated turbulence, whereas it increases slightly with moderate Reynolds numbers. For the single square grid here, λ monotonically increases with X/X_* (or X/L_0) in the region $X/X_* \geq 0.2$ ($X/L_0 \geq 1.88$).

In Fig. 3.3, we also present the streamwise evolution of the Reynolds number Re_λ along the centerline. For turbulent flow generated by the single square grid, Re_λ is around 50 in the decay region. Figure 3.3 shows that Re_λ slightly decreases in the downstream region, which can also be found in regular grid turbulence. In contrast, for the fractal square grid, previous experiments[23,25,28] have shown that Re_λ contains a distinct decay, which is different from the cases of the single square and regular grids.

3.3.3 Skewness and Flatness of the Velocity Fluctuations

Figure 3.4 shows the streamwise evolution of the skewness S_u and flatness F_u of the longitudinal fluctuating velocity component u' along the centerline. The skewness

S_u and flatness F_u are defined as

$$S_u = \frac{\langle u'^3 \rangle}{\langle u'^2 \rangle^{3/2}} \tag{3.3.1}$$

and

$$F_u = \frac{\langle u'^4 \rangle}{\langle u'^2 \rangle^2}. \tag{3.3.2}$$

In the production region corresponding to $X/X_* \leq 0.45$, especially at $X/X_* \simeq 0.2$, the velocity fluctuations are highly non-Gaussian distributions. In other words, extreme/intense events occur in this region. More specifically, the negative signs of S_u at $X/X_* \simeq 0.2$ suggest these extreme/intense events represent locally decelerating flows. In the decay region, S_u and F_u are close to the values corresponding to Gaussian distributions. The DNSs results here are qualitatively in agreement with data for the fractal square grid whose thickness ratio is $t_r = 13$.[25,28] Refer to papers[25,28] for further details. Note that the location $X/X_* \simeq 0.2$, where the most extreme events occur, is nearly the same as the case of the fractal square grid. Once again, we show the similarity between turbulent flows generated by the single square grid and those by the fractal square grids. However, the absolute values of S_u and F_u at $X/X_* \simeq 0.2$ are smaller than the corresponding values for the fractal square grid.

Note that for the single square grid along the centerline, only interactions between wakes generated by the large grid bar exist. This naturally leads to the suggestion that the unusual events at $X/X_* \simeq 0.2$ are introduced by the wake interactions as shown in Fig. 3.1. Considering that the profiles of S_u and F_u in Fig. 3.4 have similar shapes as the fractal square case,[25,28] we could claim that for fractal-generated turbulence, the extreme/intense events are also introduced by the largest wake interactions. This suggestion also explains the agreement of S_u and F_u at $X/X_* \simeq 0.2$ for the fractal square grids with different geometries.[28]

3.3.4 Homogeneity and Isotropy

Figure 3.5 shows the streamwise evolution of the large-scale anisotropy u_{rms}/v_{rms} along the centerline. Here, v_{rms} is vertical rms velocity. Generally speaking, reasonable isotropy could be observed at $X/X_* \geq 0.6$, whereas distinctly large-scale

anisotropy can be observed in the upstream region $X/X_* \leq 0.4$. The value of u_{rms}/v_{rms} is in the range of 0.95–1.0 at $X/X_* \geq 0.6$, which is smaller than the typical value (1.1–1.2) for the regular [12,14–16] and fractal square grids. [23,25–28] The reason for this unconventional small u_{rms}/v_{rms} (smaller than unity) is still an open question and the clarification of which is beyond the scope of this thesis. Figure 3.5 also shows the streamwise evolution of the small-scale anisotropy K along the centerline. The small-scale anisotropy K is defined as

$$K = \frac{< (\partial v'/\partial X)^2 >}{< (\partial u'/\partial X)^2 >}, \tag{3.3.3}$$

where v' denotes the vertical instantaneous fluctuation. According to the local isotropy hypothesis by Kolmogorov, at large enough Reynolds number, turbulence would be isotropic at small scales. It is well-known that for isotropic turbulence, the longitudinal and lateral velocity correlation functions f and g are related by $g = f + \frac{1}{2} r f'(r)$, where r is the streamwise separation. Based on the Taylor series expansion, it is easy to verify that the small-scale anisotropy K equals 2.

In the region $X/X_* \geq 0.2$, K increases with the streamwise distance X/X_* (or X/L_0) and gradually approaches the corresponding value ($K = 2$) for strictly isotropic turbulence. At the end of the computational domain $X/X_* = 1.4$ ($X/L_0 = 13.16$), K equals to 1.7, a little smaller than $K = 2$. Figure 3.5 also shows the corresponding data from the experimental study of the fractal square grid. [26] There is no distinct difference in K between the single square and fractal square grids. Note that other similar findings are also reported for the regular grid [63] and the fractal square grid. [27] A more detailed description of the small-scale anisotropy K for the regular and fractal square grids can be found in a previous paper. [27]

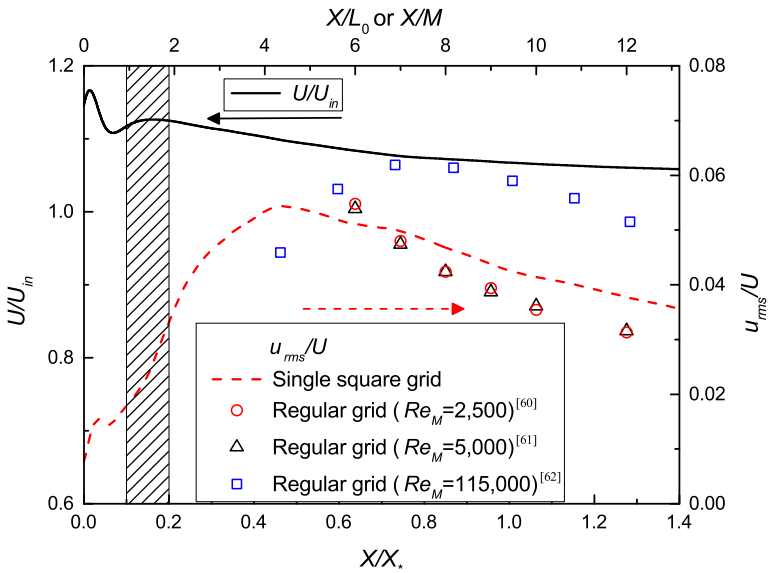

Figure 3.2: Streamwise evolution of the normalized mean velocity U/U_{in} and the turbulence intensity u_{rms}/U along the centerline. For u_{rms}/U: the present simulation (dashed line), the experiment of Komori and Nagata[60] (open circle), the experiment of Komori *et al.*[61] (open triangle), and the experiment of Valente and Vassilicos[62] (open square). Note that in Fig. 3.2, the streamwise distance from the grid X for regular grids is only non-dimensionalized by the mesh size M (see the upper X axis).

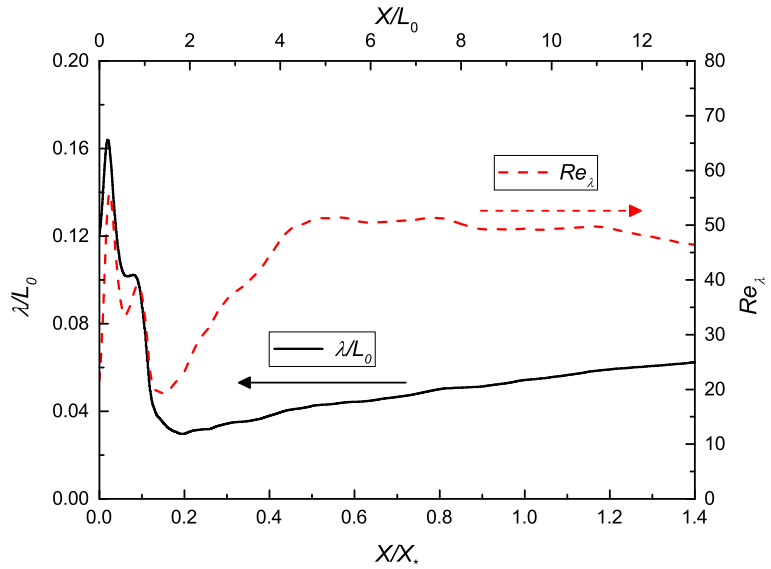

Figure 3.3: Streamwise evolution of the normalized Taylor microscale λ/L_0 and the turbulent Reynolds number Re_λ along the centerline.

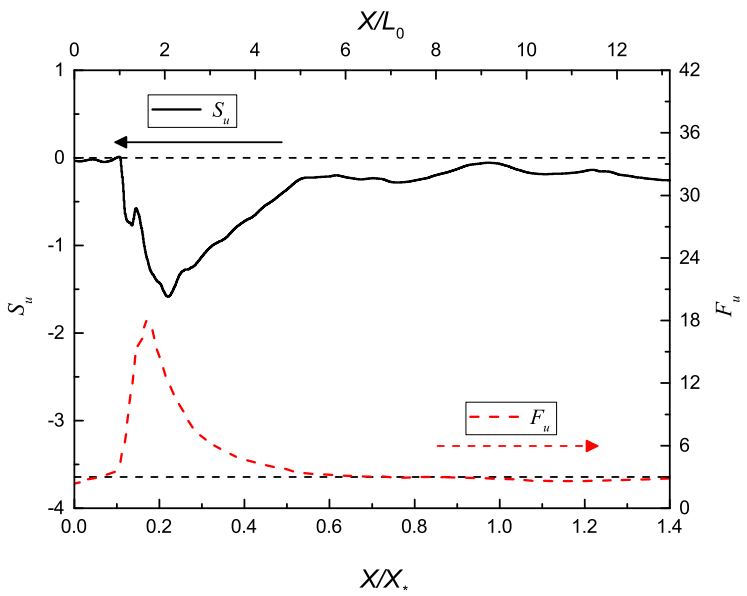

Figure 3.4: Streamwise evolution of the skewness and the flatness of the longitudinal fluctuating component u' along the centerline.

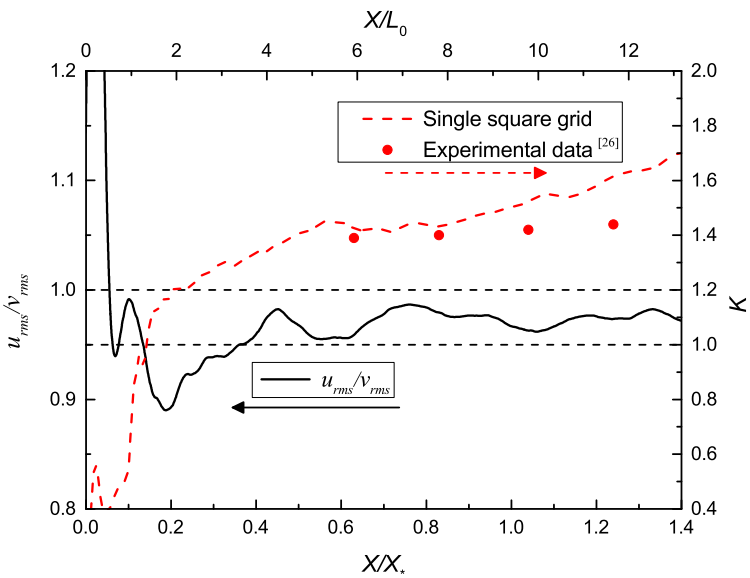

Figure 3.5: Streamwise evolution of the large-scale anisotropy u_{rms}/v_{rms} and the small-scale anisotropy K along the centerline. Symbols: experimental data K for the fractal square grid by Valente and Vassilicos. [26]

3.4 Wake Interactions

Before investigating the characteristics of wake interactions, we begin by stating the outward direction movements in the upstream region $X/X_* \leq 0.4$ (or $X/L_0 \leq 3.76$). Figure 3.6 shows the vertical profiles of mean streamwise velocity U at different downstream locations in the region $Z = 0$. At $X/X_* = 0.1$ ($X/L_0 = 0.94$), turbulent flow exhibits clear imprints of the grid bars and the minimum value points of U are located at roughly the downstream of the grid bar. In Fig. 3.6, jet-like behavior is also observed at the center of the cross-sectional area. Obviously, this jet-like profile is introduced by the large central empty zone and the wake-like profile is generated by the grid bars.

At $X/X_* \leq 0.3$ ($X/L_0 \leq 2.82$), velocity distributions at $Y/L_0 \simeq 0$ have small adjustments. For instance, at $X/X_* = 0.1$ ($X/L_0 = 0.94$), the profile of U is roughly flat at $Y/L_0 \simeq 0$. After a short streamwise distance at $X/X_* = 0.2$ ($X/L_0 = 1.88$), U at $Y/L_0 \simeq 0$ takes a similar Gaussian distribution instead (see the inset in Fig. 3.6). This adoption of typical mean velocity profile for jet explains the plateau of U observed in Fig. 3.2. We expect that the similar plateau of U found in turbulence of the fractal square grid is due to the same evolution mechanism in the upstream region. Note that we could not completely exclude the other possibility since in previous experiments of the fractal square grids, the solid wall can have a similar effect on U. The possible influences of the solid wall are discussed in previous paper.[26]

One can clearly see that due to spread effects of jet, wakes are effectively transported towards the outer boundaries. This outward expansion of the flow, due to the lack of the periodicity found in most classical grid studies, may result in a fast decay rate of turbulent energy.

Note that Fig. 3.6 shows that beyond the location $X/X_* = 0.4$ ($X/L_0 = 3.76$), the wake-like behavior disappears and only jet-like behavior exists at $Z = 0$. This conclusion is in accord with the instantaneous streamwise velocity field shown in Fig. 3.1. When investigating the properties of wake interactions, we need to take into account of this cross-stream movement.

3.4.1 Self-Similarity for Wakes at $X/X_* \leq 0.4$

Figure 3.7 shows the sketch of a turbulent wake where U_s is the maximum wake deficit and b is the half wake width. For the single square grid, U_s/U_{in} is defined by $1 - U_{min}/U_{in}$, where U_{min} is the minimum value of mean streamwise velocity U in the region $0 \leq Y/L_Y \leq 0.5$ and $Z = 0$. And the half wake width b is the vertical distance between U_s and $1/2U_s$ in the region $0 \leq Y/L_Y \leq 0.5$ and $Z = 0$. In the self-similar region, wakes possess the characteristic that U_s and b vary as $X^{-1/2}$ and $X^{1/2}$, respectively. Based on the above definition, we plot the streamwise evolution of U_s and b to check whether the self-preservation property of wakes can be found in turbulence generated by a single square grid.

Figure 3.8 shows the streamwise evolution of U_s/U_{in} and b/L_0. Note that no wake-like behavior exists at $X/X_* \geq 0.4$ (or $X/L_0 \geq 3.76$) (see Figs. 3.1 and 3.6). Hence, the downstream distance from the grid plotted in Fig. 3.8 is limited in the range $0 \leq X/X_* \leq 0.4$ ($0 \leq X/L_0 \leq 3.76$). As shown in Fig. 3.8, the non-dimensionalized wake deficit U_s/U_{in} and the non-dimensionalized half wake width b/L_0 in the range of $0.1 \leq X/X_* \leq 0.2$ ($0.94 \leq X/L_0 \leq 1.88$) fit the power law. When normalized by the thickness of the square grid bar t_0, the above mentioned region $0.1 \leq X/X_* \leq 0.2$ ($0.94 \leq X/L_0 \leq 1.88$) becomes $8.3 \leq X/t_0 \leq 16.5$. This observation is not surprising. At $X/X_* \leq 0.1$ ($X/L_0 \leq 0.94$) immediately behind the single square grid, the generated wakes have not yet reached the self-preservation state, whereas at $X/X_* \geq 0.2$ ($X/L_0 \geq 1.88$), the lack of self-preservation is associated with wake interactions. Note that the self-preservation characteristic can only be found in boundary-free shear flows. In the region $X/X_* \geq 0.2$ ($X/L_0 \geq 1.88$), we guess that wake interactions exert non-negligible effects on the evolution of wakes. Consequently, the above mentioned power laws do not hold at $X/X_* \geq 0.2$ ($X/L_0 \geq 1.88$).

3.4.2 Intermittent Factor γ

To continue our study, a brief review of the characteristics of the turbulent/nonturbulent (T/NT) interface is presented at first. In wakes, jets, and boundary layers, a ran-

domly moving interface exists which separates the turbulent region and the irrotational region. In the turbulent region, the vorticity is non-zero with the appearance of vortex tubes, vortex sheets, and irrotational and viscous dissipations, while in the irrotational region the vorticity is negligible and only viscous dissipation is found.[64,65] The non-dimensionalized instantaneous vorticity $\Omega = (\Omega_i \Omega_i)^{1/2}$ in the X–Y plane at $Z = 0$, is presented in Fig. 3.9. $\Omega_i = \varepsilon_{ijk} \partial u_k / \partial x_j$ is the vorticity field. Note that the instantaneous vorticity field in Fig. 3.9 and the instantaneous velocity field in Fig. 3.1 are obtained at the same time shot. The red color corresponds to a high value of vorticity (≥ 45) and the blue one to a zero value, respectively. As expected, two wakes are observed in the lee of the single square grid. The outward direction movements of the wakes are also visible.

Here, following the work of Bisset *et al.*,[64] we use the vorticity norm to define the T/NT interface. And the detection threshold of $\Omega = 0.7U_{in}/b$ is the same as used by Bisset *et al.*[64] and Silva and Pereira.[65] By detecting the T/NT interface, we could obtain the intermittent factor γ. The intermittent factor γ is defined as the fraction of time that fluid motions are in the turbulent region. The intermittent factor γ would be a good estimator to evaluate the wake interactions along the centerline. For instance, the non-zero value of γ suggests the existence of wake interactions. Generally speaking, a larger value of γ is associated with a higher probability that wake interactions occur. We stress that $\gamma = 1$ represents that the fluid points are totally in the turbulent region and naturally the entrainment process by which irrotational fluid points become turbulent does not exist. This connection indicates that we can study the wake interactions through the corresponding intermittent factors.

Figure 3.10 shows the streamwise evolution of γ for three different streamwise lines. The symbols c, d, and e denote the streamwise lines through the points $(Y = 0, Z = 0)$, $(Y = 1/4L_0, Z = 0)$, and $(Y = 3/4L_0, Z = 0)$, respectively (see Fig. 2.11(a)). For all three profiles, a short range of irrotational region (i.e., $\gamma = 0$) can be observed. The varied locations of the start of non-zero γ are due to different vertical distances from the grid bar. Figure 3.10 shows that the data from the straight lines d and e is considerably different, even the two lines are located at the

same vertical distance from the upper grid bar. Fluid points along the streamwise line e reach the fully turbulent state ($\gamma = 1$) faster than those along the line d. The slight difference between the profiles for streamwise lines d and e is reasonable and can be explained by the outward movement.

For the centerline c beyond the location $X/X_* = 0.1$ ($X/L_0 = 0.94$), γ has a non-zero value, which indicates the appearance of wake interactions. At $X/X_* = 0.2$ ($X/L_0 = 1.88$), γ has a small value of 0.2. It is interesting to note that this relatively small value of γ is associated with the most extreme events (see Fig. 3.4). Figure 3.10 shows that at $0.2 \leq X/X_* \leq 0.4$ ($1.88 \leq X/L_0 \leq 3.76$), the value of γ ranges from 0.2 to 1. In previous subsection, we assume that the non-negligible effects of wake interactions cause the lack of the self-preservation at $X/X_* \geq 0.2$ ($X/L_0 \geq 1.88$). Here, the large values of γ confirm our hypothesis.

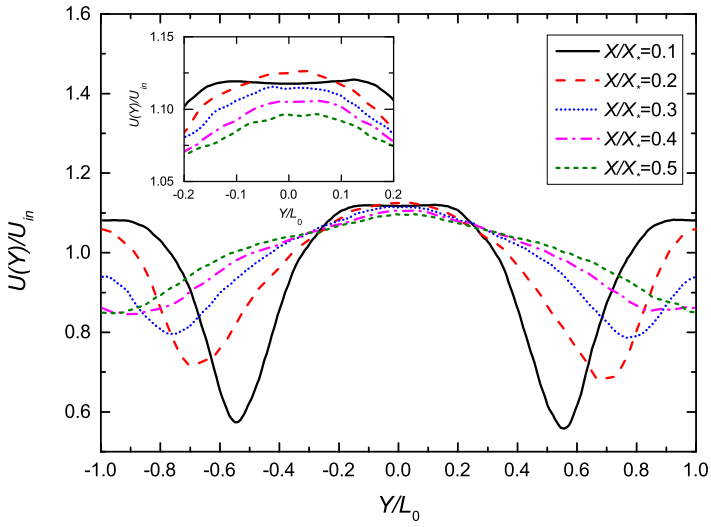

Figure 3.6: Vertical distribution of the normalized mean velocity U/U_{in} at different streamwise locations ($X/X_* = 0.1$, 0.2, 0.3, 0.4, and 0.5).

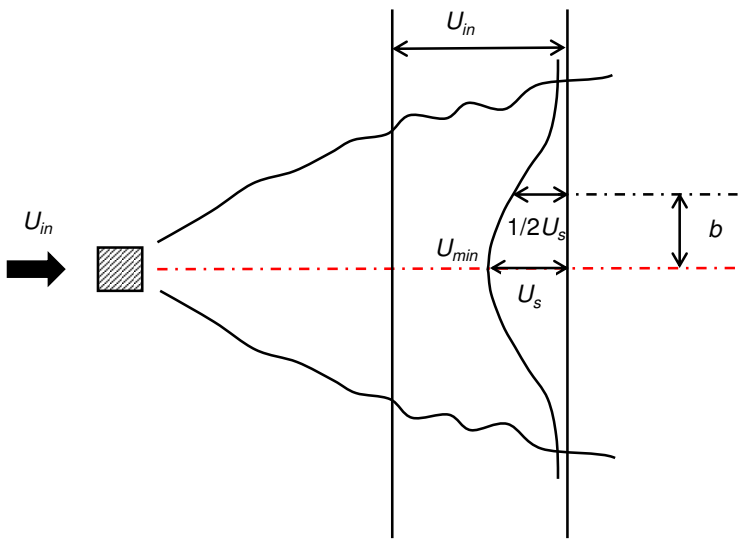

Figure 3.7: Sketch of a turbulent wake.

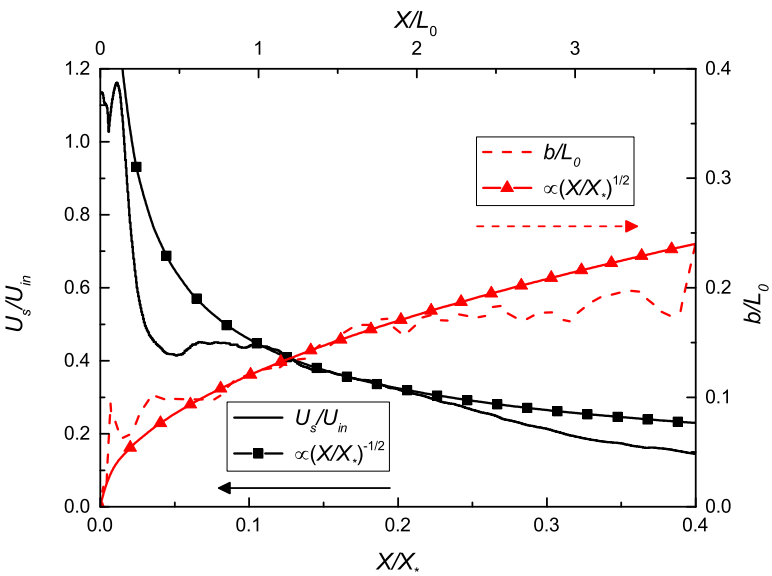

Figure 3.8: Streamwise evolution of U_s/U_{in} and b/L_0 at $X/X_* \leq 0.4$.

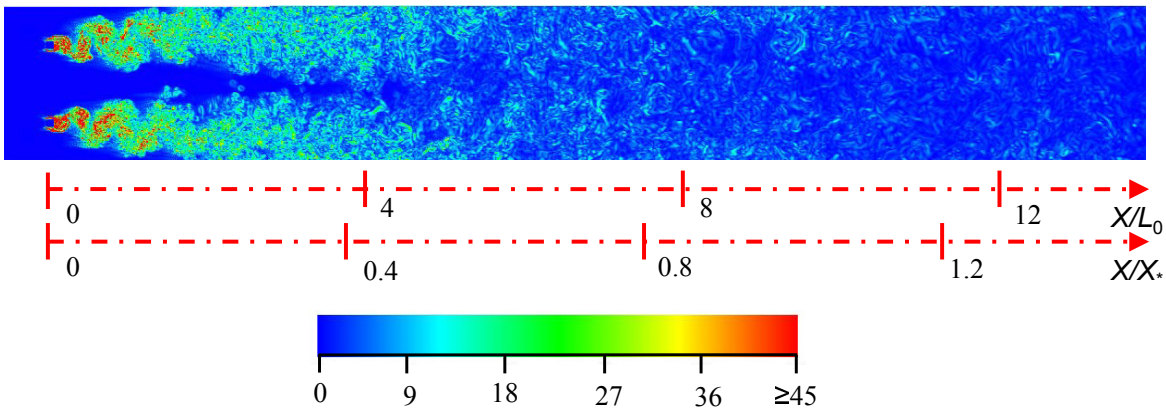

Figure 3.9: Instantaneous vorticity Ω normalized by the inlet velocity U_{in} and the length of the grid bar L_0. The red color corresponds to ≥ 45 and the blue one to 0.

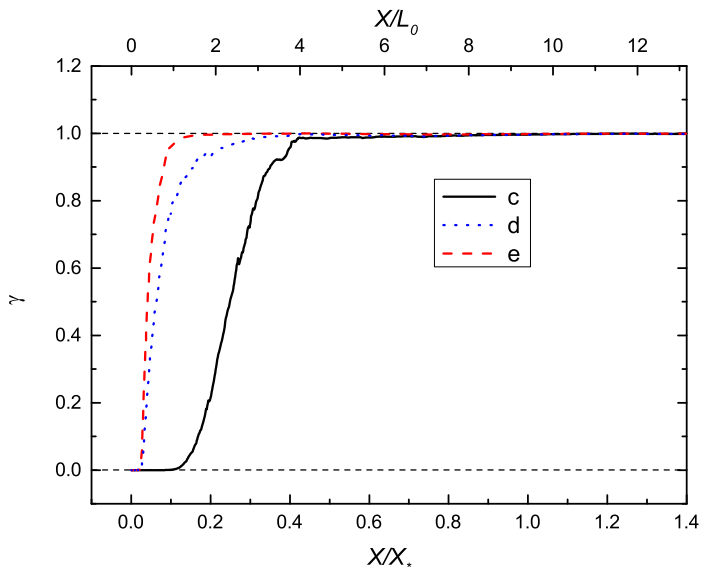

Figure 3.10: Streamwise evolution of the intermittent factor γ along three straight lines.

3.5 Invariants of Velocity Gradient Tensor

The invariants of velocity gradient tensor in turbulent flows have been extensively studied.[65,67,68,84] The velocity gradient tensor $A_{ij} = \partial u_i/\partial x_j$ can be decomposed into two parts,

$$A_{ij} = S_{ij} + \Omega_{ij}, \tag{3.5.1}$$

where $S_{ij} = \frac{1}{2}(\partial u_i/\partial x_j + \partial u_j/\partial x_i)$ and $\Omega_{ij} = \frac{1}{2}(\partial u_i/\partial x_j - \partial u_j/\partial x_i)$ denote the rate-of-strain and rate-of-rotation tensors, respectively. The second and third invariants of the velocity gradient tensor are given by

$$Q = -\frac{1}{2}A_{ij}A_{ji} = \frac{1}{4}(\Omega_i\Omega_i - 2S_{ij}S_{ij}) = Q_W + Q_S \tag{3.5.2}$$

and

$$R = -\frac{1}{3}A_{ij}A_{jk}A_{ki} = -\frac{1}{3}(S_{ij}S_{jk}S_{ki} + \frac{3}{4}\Omega_i\Omega_jS_{ij}) = R_S + R_W, \tag{3.5.3}$$

respectively. The detailed description of the invariants and corresponding physical meanings can be found in previous paper.[65]

Previous numerical studies presented that turbulent flows (e.g., turbulent jets,[65] isotropic turbulence,[84] turbulent channel flows,[67] and turbulent mixing layers[68]) possess a similar "teardrop" shape for the joint probability density function (PDF) of R and Q. Thus, this "teardrop" shape is thought to be a universal feature for turbulent flows. The four different topologies (i.e., stable-focus stretching, unstable-focus contracting, stable-node saddle/saddle, and unstable-node saddle/saddle) in the (R, Q) map are shown in Fig. 3.11. Topologies above the discriminant line, $D = 0$, correspond to spiraling or vortical motions, whereas a combined node-saddle type below the discriminate line. And the $(Q_W, -Q_S)$ map is also a useful tool to analyze the characteristic of fluid motions. In Fig. 3.12, data that fall along the horizontal line defined by $-Q_S = 0$ represent points with high enstrophy ($\Omega^2 = \Omega_i\Omega_i/2$) and little dissipation as found in the case of a solid body rotation around the center of a vertex tube. Data on the 45 degree line, $Q_W = -Q_S$, represent points of both high dissipation and high enstophy density, which is a typical characteristic for vortex sheet structures. Finally, data that fall on the

vertical line, $Q_W = 0$, are associated with points where the dissipation is much greater than the enstrophy density.

First, we present the joint PDFs of the (R, Q) and the $(Q_W, -Q_S)$ maps for homogeneous isotropy turbulence (HIT) [69] at a comparable Reynolds number $Re_\lambda = 83$ as a reference (see Fig. 3.13). The invariants in Fig. 3.13 are non-dimensionalized by $< S_{ij}S_{ij} >$. The dash line in Fig. 3.13(a) is defined by the discriminant $D = (27/4)R^2 + Q^3 = 0$, which divides the (R, Q) map into two parts. Note that the joint PDFs in Figs. 3.13 are quantitatively in good accord with data in previous numerical studies. [65,67,68,84]

It is interesting to observe how the (R, Q) and $(Q_W, -Q_S)$ maps evolve along the centerline and where these maps obtain their well known shapes (i.e., the "teardrop" for the (R, Q) map).

The first finding is that Figs. 3.14, 3.15, and 3.16 indicate that at $X/X_* \leq 0.1$ $(X/L_0 \leq 0.94)$, the contour lines are fundamentally different from the corresponding lines for HIT (see Fig. 3.13). The "teardrop" shape cannot be observed in the (R, Q) maps at $X/X_* \leq 0.1$ $(X/L_0 \leq 0.94)$. Instead, contour lines in the (R, Q) maps are only found at $Q \leq 0$. The shapes of the (R, Q) maps suggest that at $X/X_* \leq 0.1$ $(X/L_0 \leq 0.94)$, for all fluid points, the magnitude of the strain production is larger than enstrophy. Note that the (R, Q) map at X/X_* (or X/L_0) $= 0$ shows a remarked tendency to be aligned with the line, $D = 0$ at $R \leq 0$. At a short distance from the grid $X/X_* = 0.04$ $(X/L_0 = 0.38)$, even not possessing the "teardrop" shape, the contour lines start to be aligned with the line $D = 0$, when $R \geq 0$. The contour lines also contain a slight tendency to be aligned with the line $D = 0$ at $R \leq 0$. The contour lines of the $(Q_W, -Q_S)$ maps in Figs. 3.14, 3.15, and 3.16 exhibit a remarked tendency to be aligned with the vertical line, $Q_W = 0$. This marked tendency indicates the dominance of irrotational dissipation. The results for the $(Q_W, -Q_S)$ maps at $X/X_* \leq 0.1$ $(X/L_0 \leq 0.94)$ are not surprising. In previous section, we have already pointed out that there are no wake interactions at $X/X_* \leq 0.1$ $(X/L_0 \leq 0.94)$. The shapes of the (R, Q) and the $(Q_W, -Q_S)$ maps at $X/X_* = 0.04$ and 0.1 $(X/L_0 = 0.38$ and $0.94)$ are similar to ones from T/NT interface by da Silva and Pereira. [65] It seems that fluid points at $X/X_* \leq 0.1$

($X/L_0 \leq 0.94$) possess some characteristics of the T/NT interface.

Figures 3.17–3.21 show that in the region $0.1 < X/X_* \leq 0.4$ ($0.94 < X/L_0 \leq 3.76$), the shapes of the (R, Q) and $(Q_W, -Q_S)$ maps gradually change to the general shapes as shown in Fig. 3.13. Fluid points of values $Q > 0$ appear at $X/X_* = 0.16$ ($X/L_0 = 1.50$) (see Fig. 3.17(a)). Besides the clear correlation in the region, $R > 0$ and $Q < 0$, the Q and R are also weakly correlated in the region, $R < 0$ and $Q < 0$. Fluid points at $X/X_* = 0.16$ ($X/L_0 = 1.50$) are characterized by a preference of irrotational dissipation as the ones at $X/X_* \leq 0.1$ ($X/L_0 \leq 0.94$). However, there are also points that possess both strong dissipation and high enstrophy density, which are aligned with the line, $Q_W = -Q_S$. This alignment indicates the existence of the structures of vortex sheets. Figure 3.18(b) indicates that at $X/X_* = 0.20$ ($X/L_0 = 1.88$), where extreme/intense events occur, vortex tube structures are not generated yet. At $X/X_* = 0.26$ ($X/L_0 = 2.44$) (Fig. 3.19), there are points that possess high enstrophy density and little dissipation, which are aligned with the line, $-Q_S = 0$. The near solid body rotation (high enstrophy density and little dissipation) is due to the presence of vortex tubes. Note that the structures of the vortex sheets and vortex tubes are firstly found at $X/X_* \simeq 0.16$ and 0.26 ($X/L_0 \simeq 1.50$ and 2.44), respectively. This observation seems to suggest that the vortex tubes need more time to be generated than vortex sheets.

The contour lines in Fig. 3.20(a) are still weakly skewed toward the $D = 0$ at $R \leq 0$. In contrast, Fig. 3.21(a) shows that at $X/X_* = 0.4$ ($X/L_0 = 3.76$), the slight tendency aligned with the line $D = 0$ at $R \leq 0$ disappears. The contour lines of the joint PDFs for the (R, Q) map take the well known "teardrop" shape. Moreover, the contour lines in $(Q_W, -Q_S)$ map at $X/X_* = 0.4$ ($X/L_0 = 3.76$) also acquire the shape similar to a turbulent channel flow,[67] a turbulent jet,[65] and HIT (Fig. 3.13(b)).

As shown in Figs. 3.22 and 3.23, beyond $X/X_* = 0.4$ ($X/L_0 = 3.76$), the overall shapes of the (R, Q) and $(Q_W, -Q_S)$ maps are very similar. A small difference between the joints PDFs at $X/X_* = 0.5$ ($X/L_0 = 4.70$) and $X/X_* = 1.4$ ($X/L_0 = 13.16$) shown in Figs. 3.22(a) and 3.23(a) is that the contour lines are slightly squeezed in the horizontal direction. And the shapes of Figs. 3.22 and 3.23

are similar to those in HIT (see Fig. 3.13).

In summary, fluid points at $X/X_* = 0.04$ and 0.1 ($X/L_0 = 0.38$ and 0.94) exhibit similar characteristics as those located at the turbulent/nonturbulent interface for a jet flow.[65] In the range $0.1 \leq X/X_* \leq 0.4$ ($0.94 \leq X/L_0 \leq 3.76$), the contours in the (R, Q) and $(Q_W, -Q_S)$ maps gradually acquire their characteristics shapes. Finally, at $X/X_* \geq 0.4$ ($X/L_0 \geq 3.76$), even the contour lines in the (R, Q) map and $(Q_W, -Q_S)$ map still have small variations, their general shapes remain unchanged and resemble the corresponding shapes obtained in HIT,[84] a turbulent channel flow,[67] and a jet flow.[65]

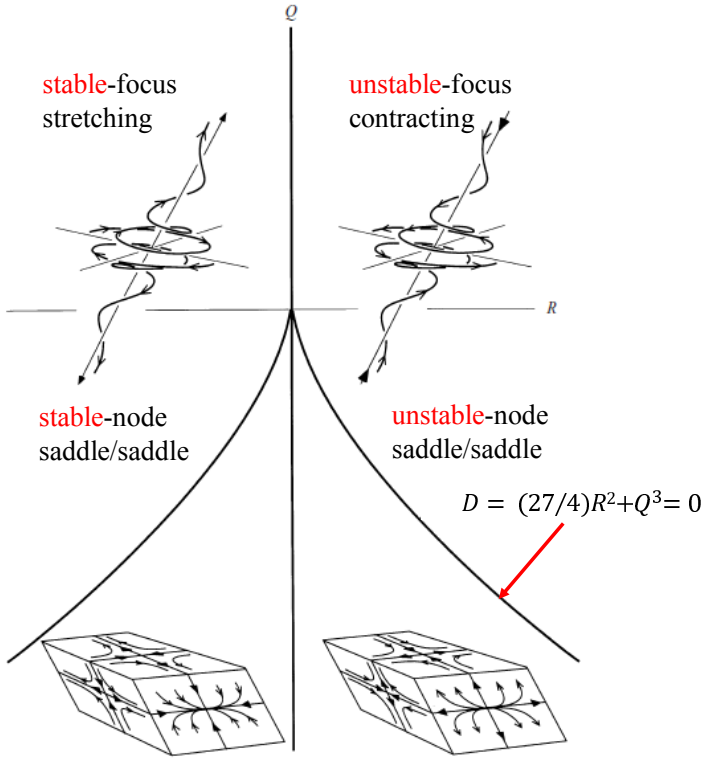

Figure 3.11: Three-dimensional topologies in the (R, Q) map, following Soria *et al.*[68]

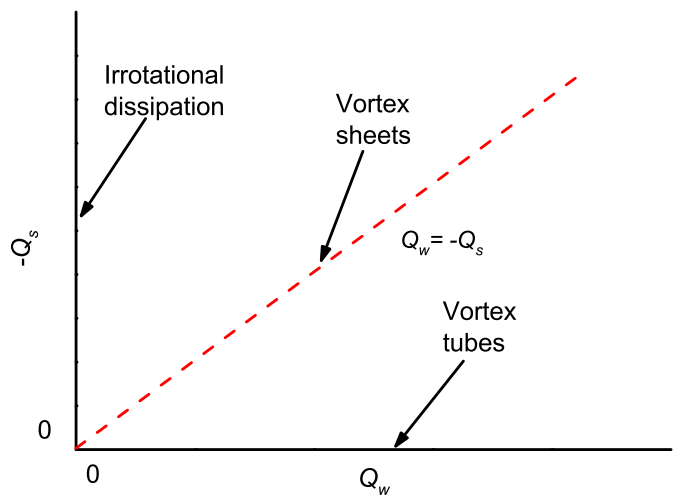

Figure 3.12: Physical interpretation of the $(Q_W, -Q_S)$ map, following Silva and Pereira.[65]

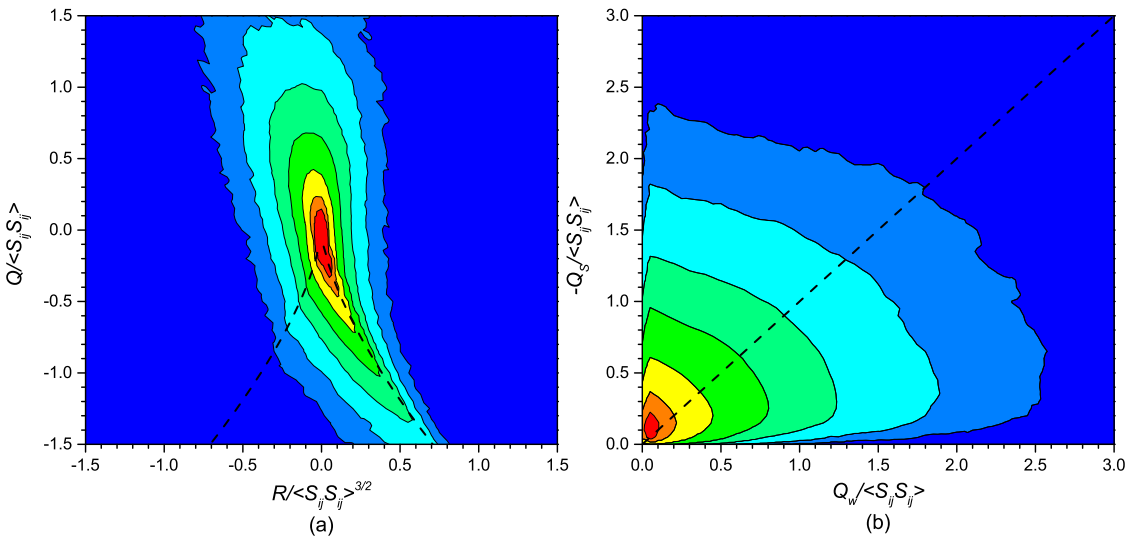

Figure 3.13: Joint PDFs of (a) R and Q and (b) Q_W and $-Q_S$ for homogeneous isotropic turbulence (HIT) at $Re_\lambda = 83$.[69] The contour levels are 0.01, 0.03, 0.1, 0.3, 1, 3, and 6.

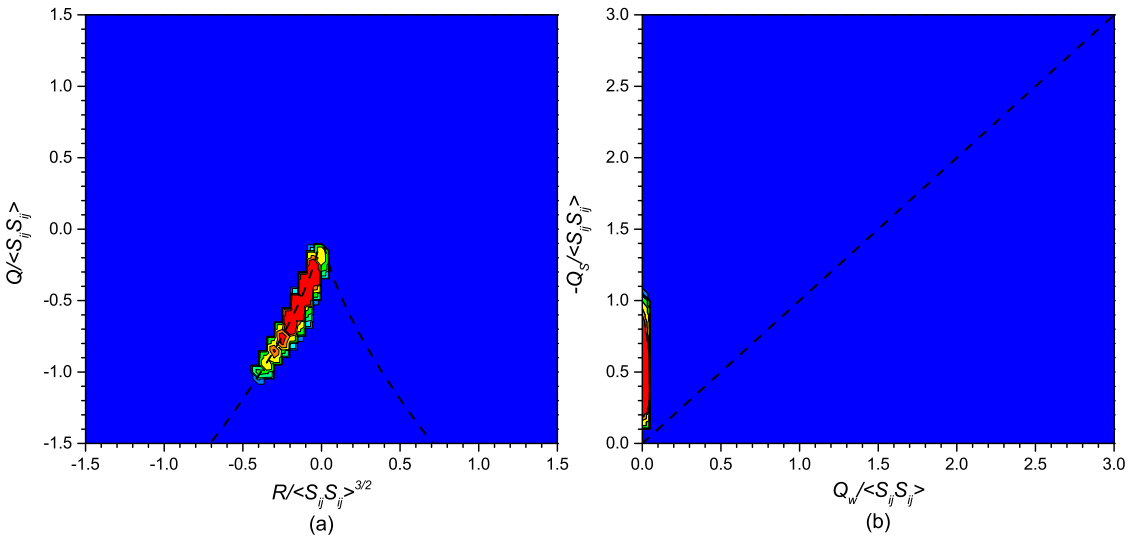

Figure 3.14: Joint PDFs of (a) R and Q and (b) Q_W and $-Q_S$ at $X/X_* = 0.0$ ($X/L_0 = 0.0$). The contour levels are the same as in Fig. 3.13.

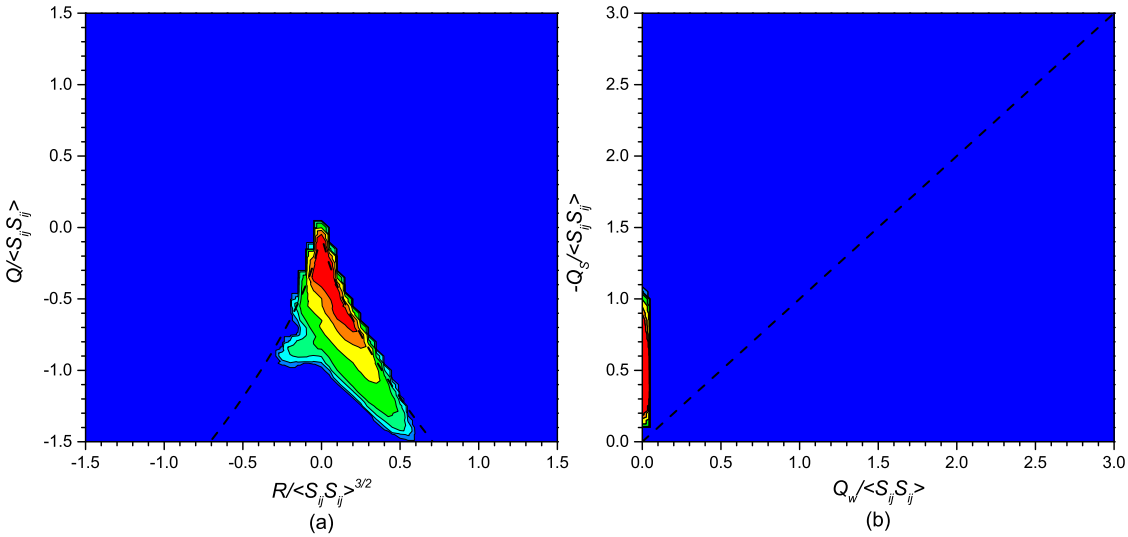

Figure 3.15: Joint PDFs of (a) R and Q and (b) Q_W and $-Q_S$ at $X/X_* = 0.04$ ($X/L_0 = 0.38$). The contour levels are the same as in Fig. 3.13.

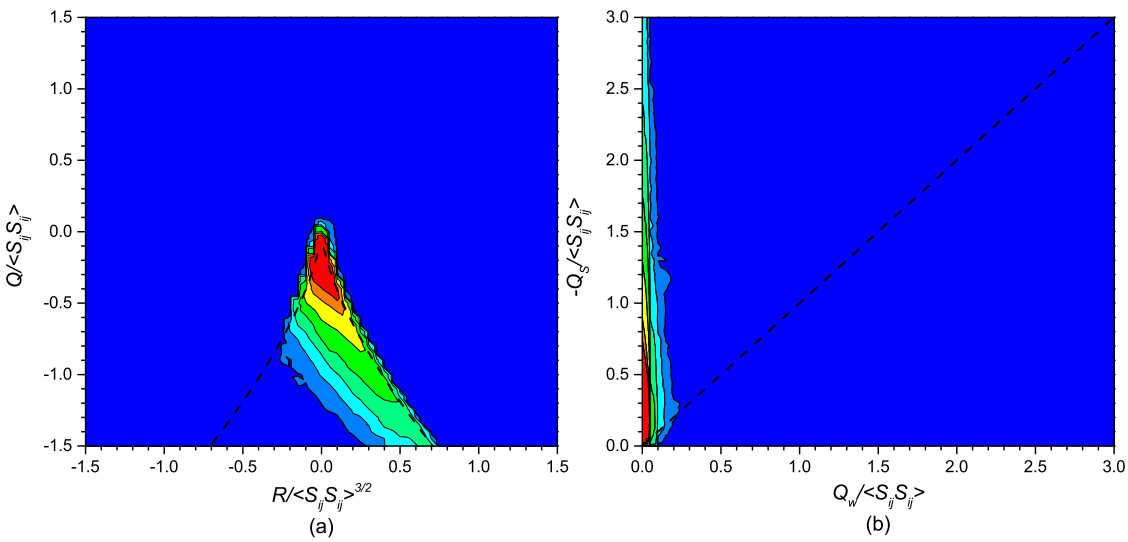

Figure 3.16: Joint PDFs of (a) R and Q and (b) Q_W and $-Q_S$ at $X/X_* = 0.10$ ($X/L_0 = 0.94$). The contour levels are the same as in Fig. 3.13.

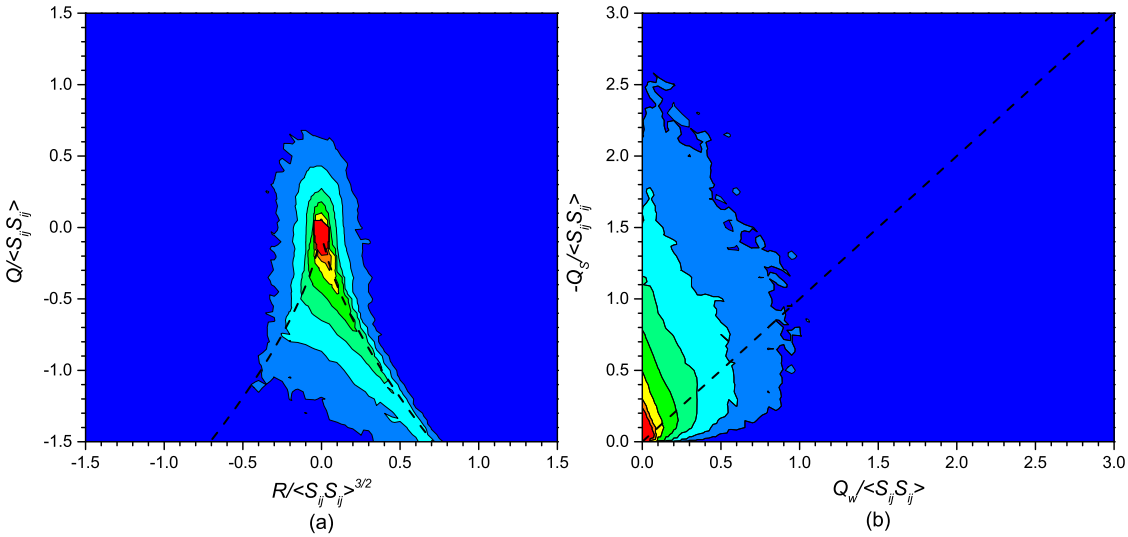

Figure 3.17: Joint PDFs of (a) R and Q and (b) Q_W and $-Q_S$ at $X/X_* = 0.16$ ($X/L_0 = 1.50$). The contour levels are the same as in Fig. 3.13.

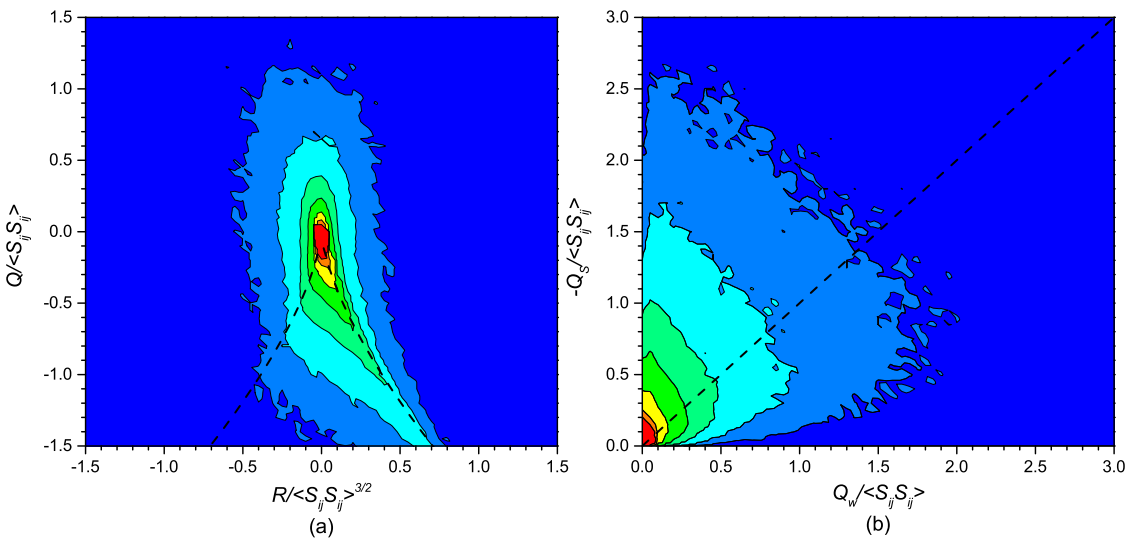

Figure 3.18: Joint PDFs of (a) R and Q and (b) Q_W and $-Q_S$ at $X/X_* = 0.20$ ($X/L_0 = 1.88$). The contour levels are the same as in Fig. 3.13.

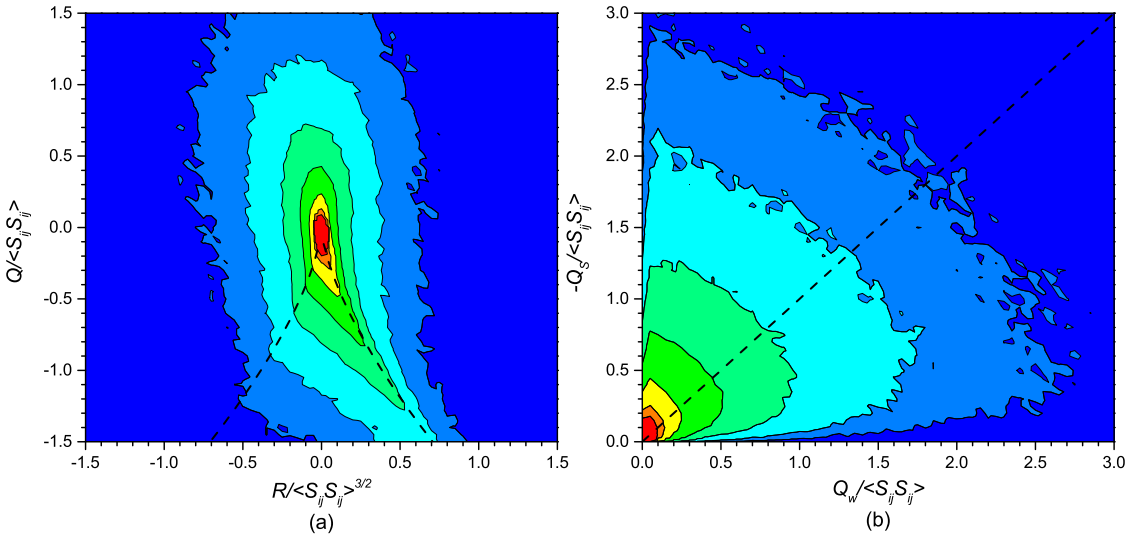

Figure 3.19: Joint PDFs of (a) R and Q and (b) Q_W and $-Q_S$ at $X/X_* = 0.26$ ($X/L_0 = 2.44$). The contour levels are the same as in Fig. 3.13.

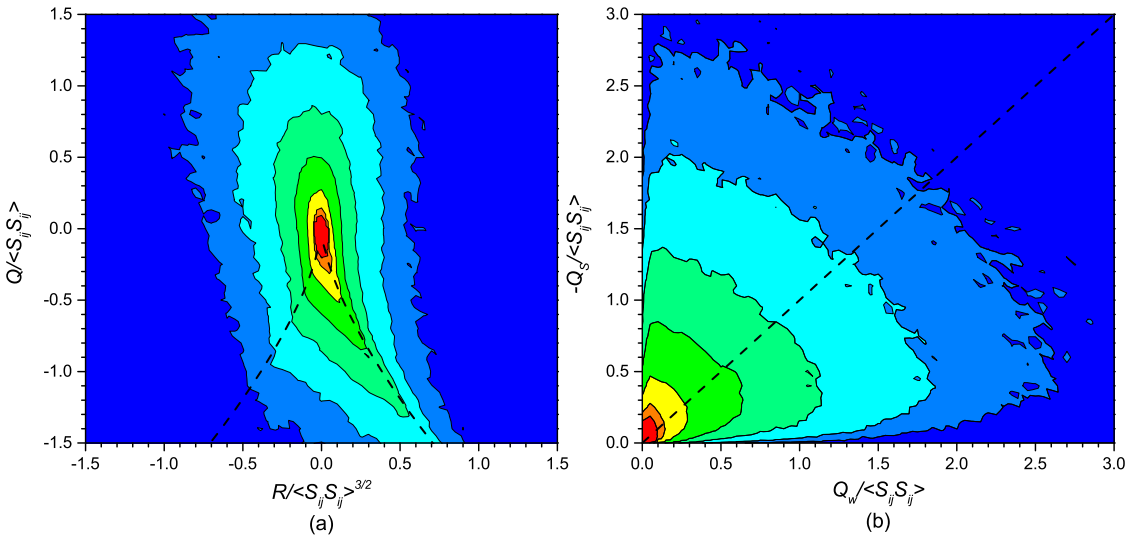

Figure 3.20: Joint PDFs of (a) R and Q and (b) Q_W and $-Q_S$ at $X/X_* = 0.30$ ($X/L_0 = 2.82$). The contour levels are the same as in Fig. 3.13.

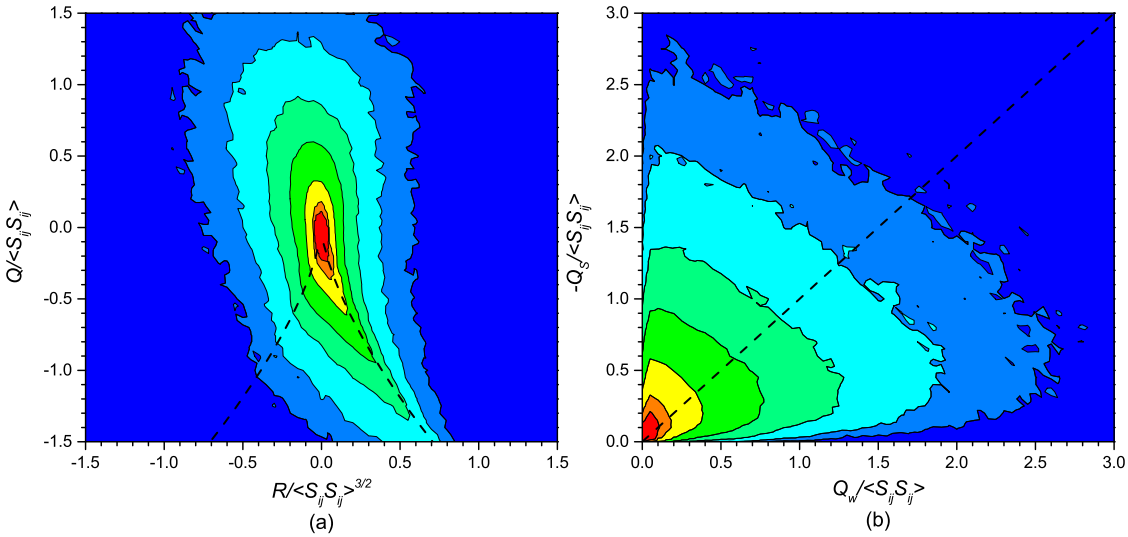

Figure 3.21: Joint PDFs of (a) R and Q and (b) Q_W and $-Q_S$ at $X/X_* = 0.40$ ($X/L_0 = 3.76$). The contour levels are the same as in Fig. 3.13.

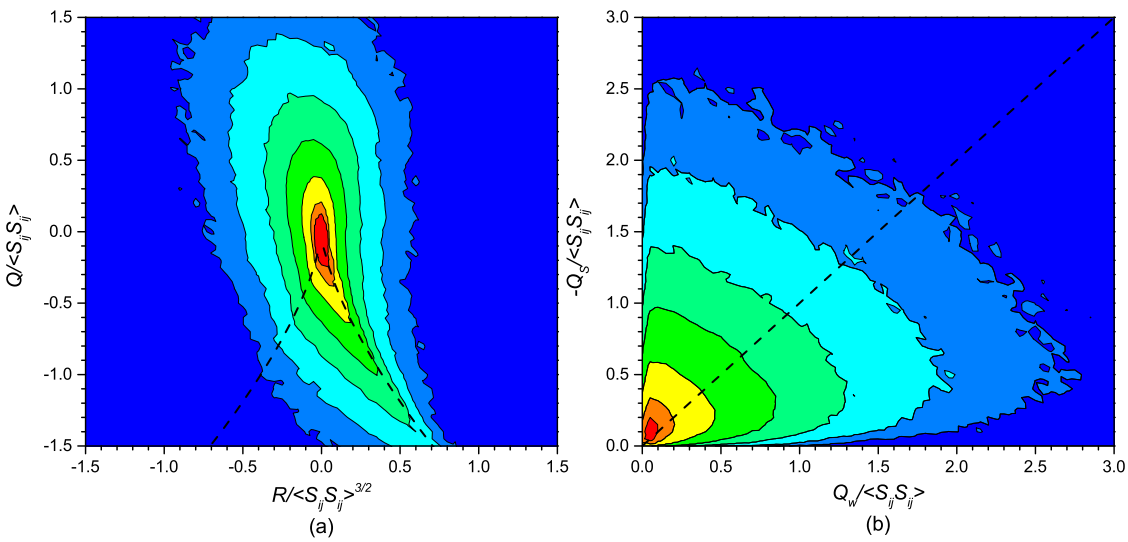

Figure 3.22: Joint PDFs of (a) R and Q and (b) Q_W and $-Q_S$ at $X/X_* = 0.50$ ($X/L_0 = 4.70$). The contour levels are the same as in Fig. 3.13.

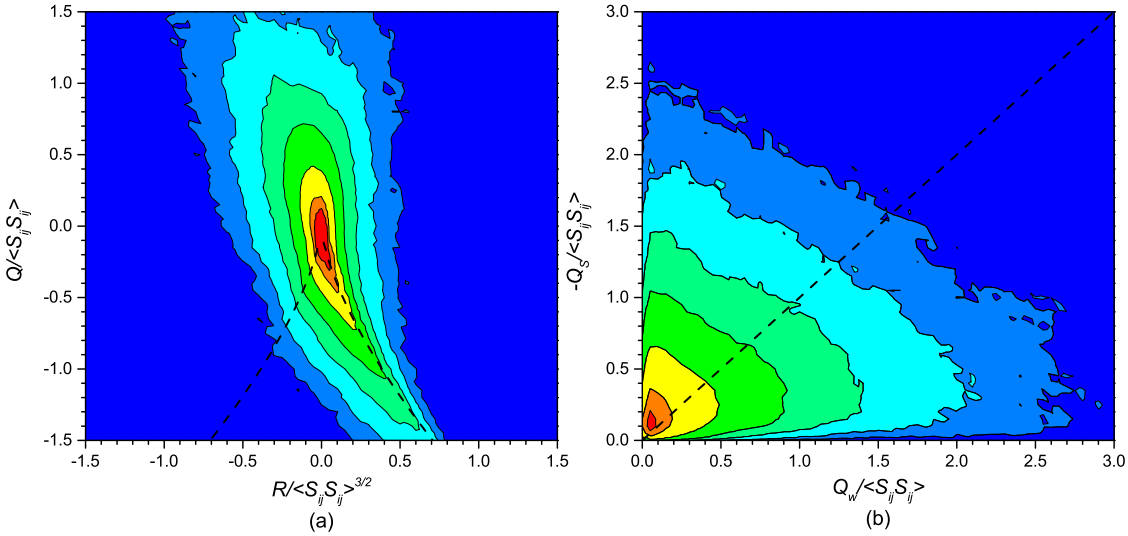

Figure 3.23: Joint PDFs of (a) R and Q and (b) Q_W and $-Q_S$ at $X/X_* = 1.40$ ($X/L_0 = 13.16$). The contour levels are the same as in Fig. 3.13.

3.6 Summary

For turbulent flows generated by a single square grid, we can draw the following conclusions.

1. The intensity u_{rms}/U reaches its maximum value at $X_{peak} \simeq 0.45X_*$, which is similar to the corresponding value for the fractal square grid. Meanwhile, we confirm the hypothesis proposed by Mazellier and Vassilicos that for the fractal square grid, the location of turbulence intensity peak X_{peak} is largely determined by the scale of the largest grid bar.

2. Fluid motions at $X/X_* \simeq 0.2$ ($X/L_0 \simeq 1.88$ in the present case) are strongly dependent on the wake interactions generated by the grid bar. The similar characteristic for turbulent flow generated by the fractal square grid indicates the dominant effects of the interactions of the largest wakes at $X/X_* \simeq 0.2$.

3. The intermittent factor γ shows that the wake interactions begin at $X/X_* \simeq 0.1$ ($X/L_0 \simeq 0.94$ in the present case) downstream of the grid. And the intermittent factor γ approaches 1 at $X/X_* \simeq 0.4$ ($X/L_0 \simeq 3.76$ in the present case).

4. The (R, Q) and $(Q_W, -Q_S)$ maps suggest that at $X/X_* < 0.2$ ($X/L_0 < 1.88$), the fluid motions are distinctly different from those of turbulent channel flows, turbulent mixing layers, and isotropic turbulence. With the spatial development, the joint PDFs of the (Q, R) and $(Q_W, -Q_S)$ maps at $X/X_* = 0.4$ ($X/L_0 = 3.76$) adopt their well known shapes.

Chapter 4

Fractal-Generated Turbulence[49,50]

In this chapter, the DNSs of the fractal square grid are performed. Here, simulation results of the fractal square grid are mainly compared with those of the single square grid presented in chapter 3. Note that in chapter 3, we suggest that for the single and fractal square grids, the turbulence motions at $X/X_* \geq 0.2$ largely depend on interactions of the largest wakes.

4.1 Wake Interaction Patterns

Before discussion, we begin by revisiting the wake interaction patterns for the single and fractal square grids.[25] See Fig. 2.11 and Table 2.1 in chapter 2 for the schematics of the single and fractal square grids, and the corresponding grid parameters. It should be stressed that the description concerning wake interaction pattern in this subsection is based on previous experimental studies.[23,25,26]

As shown in Fig. 4.1, for the single square and regular grids, the generated wakes are of the same size and they meet each other at the same distance from the grid. In contrast, for the fractal square grid, wakes of different sizes are produced and they interact with their pairs at different streamwise distances. For the wakes of smaller sizes, they interact with neighboring wakes at a shorter distance from the grid and stir turbulence. The furthermost interactions along the centerline are those

of the wakes generated by the largest grid bars. In a previous paper,[41] Laizet and Vassilicos regarded the successive wake-interactions of different size wakes with the distance from the grid as the space-scale unfolding (SSU) mechanism.

In chapter 3, we have presented that in the region corresponding to $X/X_* \geq 0.2$, the characteristics of turbulence generated by the fractal square grid largely depend on the largest wake interactions. To some extent, turbulence immediately behind the fractal square grid owning to the smaller wake interactions can be regarded as the additional turbulence. The largest wakes of the biggest grid bars are surrounded by this additional turbulence. Consequently, the development of the largest wakes would be affected by the additional turbulence, at least to some extent.

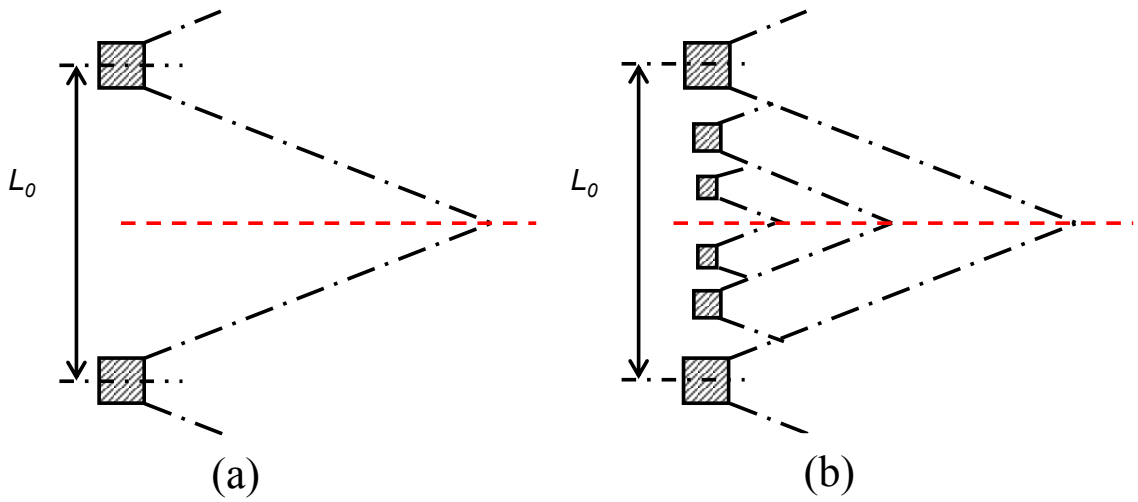

Figure 4.1: Schematics of wake interactions. (a) single square grid and regular grid, (b) fractal square grid, following Mazellier and Vassilicos.[25]

4.2 Flow Visualizations

4.2.1 Instantaneous Streamwise Velocity in the X–Y Plane

Figure 4.2 shows the instantaneous streamwise velocity field in the X–Y plane at $Z = 0$ for turbulent flow generated by the fractal square grid. The red color corresponds to a high value of streamwise velocity ($\geq 1.30U_{in}$) and the blue one to a zero and negative value, respectively.

In both cases (Fig. 3.1 in chapter 3 for the single square grid and Fig. 4.2 for the fractal square grid), the flow fields are highly inhomogeneous and sheared in the upstream region $X/X_* \leq 0.4$ ($X/L_0 \leq 3.76$). For the single square grid, only large scale wakes are observed behind the grid bar. Moreover, the jet-like behavior introduced by the large opening zone persists until the end of the test section (see Fig. 3.1 in chapter 3). As expected, behind the fractal square grid, both jet-like and wake-like behavior is also visible. However, the jet-like behavior does not last for a long streamwise distance. Also, the imprints of the largest grid bars almost disappear at $X/X_* = 1.4$ ($X/L_0 = 13.16$), which is clearly different from the single square case. It seems that the mixing performance is higher in turbulence generated by the fractal square grid than by the single square grid. Figures 3.1 and 4.2 also suggest that immediately behind the largest grid bars, in both cases reverse flows (the blue regions) are observed.

4.2.2 Cross-sectional profiles of Instantaneous Streamwise Velocity

For further investigation of both turbulent flows, we also plot the cross-sectional profiles of instantaneous streamwise velocity at six different locations ($X/X_* = 0.01, 0.1, 0.2, 0.3, 0.6$, and 1.4). In Fig. 4.3, the red color corresponds to a high value of streamwise velocity ($\geq 1.25U_{in}$) and the blue one to a small negative value ($\leq -0.5U_{in}$), respectively.

Figure 4.3 shows that turbulent flows generated by the single square grid possess imprints of the largest grid bar at $X/X_* = 1.4$ ($X/L_0 = 13.16$). For the fractal

square grid, at $X/X_* = 0.01$ ($X/L_0 = 0.09$) immediately behind the fractal square grid, wakes of all four different sizes are visible. Then, wakes start to merge into their surroundings and the turbulent flow gradually loses the imprints of relatively smaller grids bars owning to turbulent mixing. At $X/X_* = 0.3$ ($X/L_0 = 2.82$), the wakes generated by the second largest grids almost vanish and only the ones corresponding to the largest grids still exist. As expected, for the fractal square grid, the imprints of the largest grid are more persistent than those of smaller square grids.

One interesting finding is that at $X/X_* = 0.3$ ($X/L_0 = 2.82$), for both cases, only influences of the largest grid bars are visible. Here, once again we verify the implicit assumption of Mazellier and Vassilicos[25] that in turbulence generated by the fractal square grid, the dominant effects are those generate by the largest grid bars, since the smaller wakes almost emerge into their surroundings beyond $X/X_* = 0.3$ ($X/L_0 = 2.82$).

Another interesting finding is that at $X/X_* = 1.4$ ($X/L_0 = 13.16$), the cross-sectional instantaneous velocity distributions of the fractal square grid are fundamentally different from the case of the single square grid. For turbulence generated by the single square grid, in the central zone of the Y–Z plane, the velocities are slightly larger than the inlet velocity U_{in}, whereas for the fractal square grid, the corresponding values seem to be a little smaller than U_{in}. Hence, different from the single square grid, the fractal square grid possesses a wake-like velocity distribution at $X/X_* = 1.4$ ($X/L_0 = 13.16$) instead of the jet-like distribution for the single square grid. Note that a similar wake-like velocity distribution at the end of the simulation region is also reported by Nagata *et al.*[34] and Laizet *et al.*[42]

4.2.3 Vortex Structure

Following the work of Dubief and Delcayre,[70] the Q criterion is also employed to investigate the coherent vortices in the turbulence generated by the single and fractal square grids.

Figure 4.4 shows the isosurfaces of Q in the regions $11 \leq X/L_0 \leq 13$ and $-1 \leq Y/L_0, Z/L_0 \leq 1$ for both grids; red and yellow surfaces are isosurfaces of $QL_0^2/U_{in}^2 = 9$ and $QL_0^2/U_{in}^2 = -9$, respectively. In both cases, worm-like struc-

tures[70,71] can be observed, but the vortex structures in the fractal-generated turbulence (see Fig. 4.4(b)) are more uniformly and densely distributed than those in the turbulence generated by the single square grid (see Fig. 4.4(a)). This difference is related to the different turbulence generation mechanisms; for the single square grid, only interactions of the largest wakes exist, whereas for the fractal square grid, turbulence can be produced by the interactions of multiscale wakes (see Fig. 4.1).

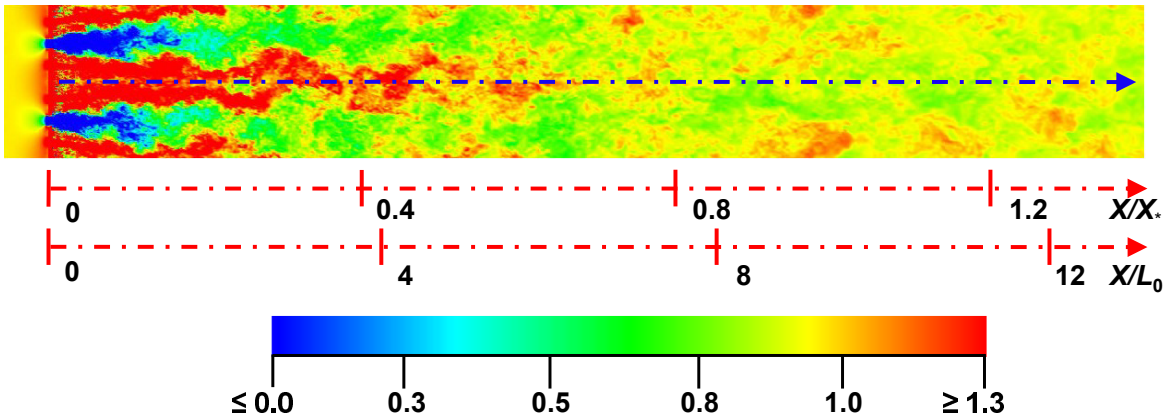

Figure 4.2: Instantaneous streamwise velocity u, normalized by the inflow velocity U_{in}. The red color corresponds to $\geq 1.3U_{in}$ and the blue one to ≤ 0.

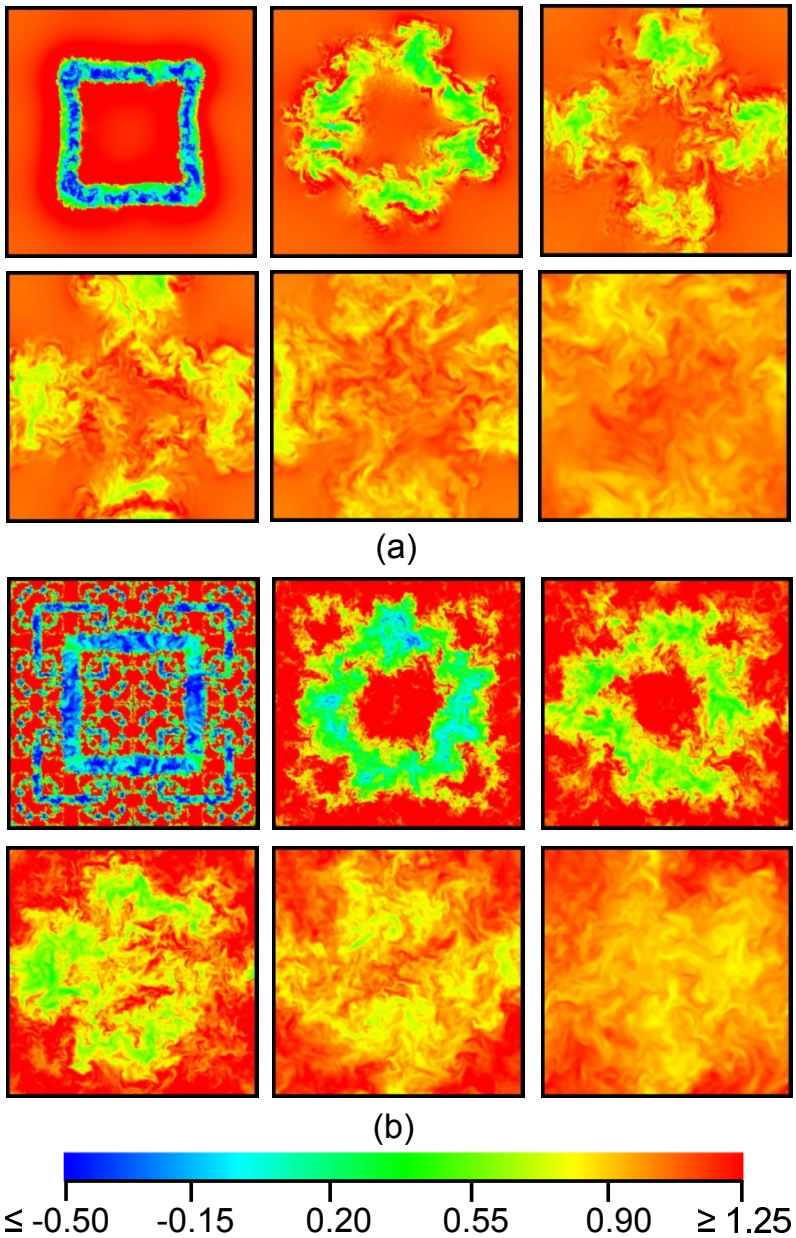

Figure 4.3: Instantaneous streamwise velocity u, normalized by the inflow velocity U_{in} in the Y–Z planes. From the upperleft to the lower right, the locations are $X/X_* = 0.01, 0.1, 0.2, 0.3, 0.6$, and 1.4. (a) single square grid and (b) fractal square grid. The red color corresponds to $\geq 1.25U_{in}$ and the blue one to $\leq -0.5U_{in}$.

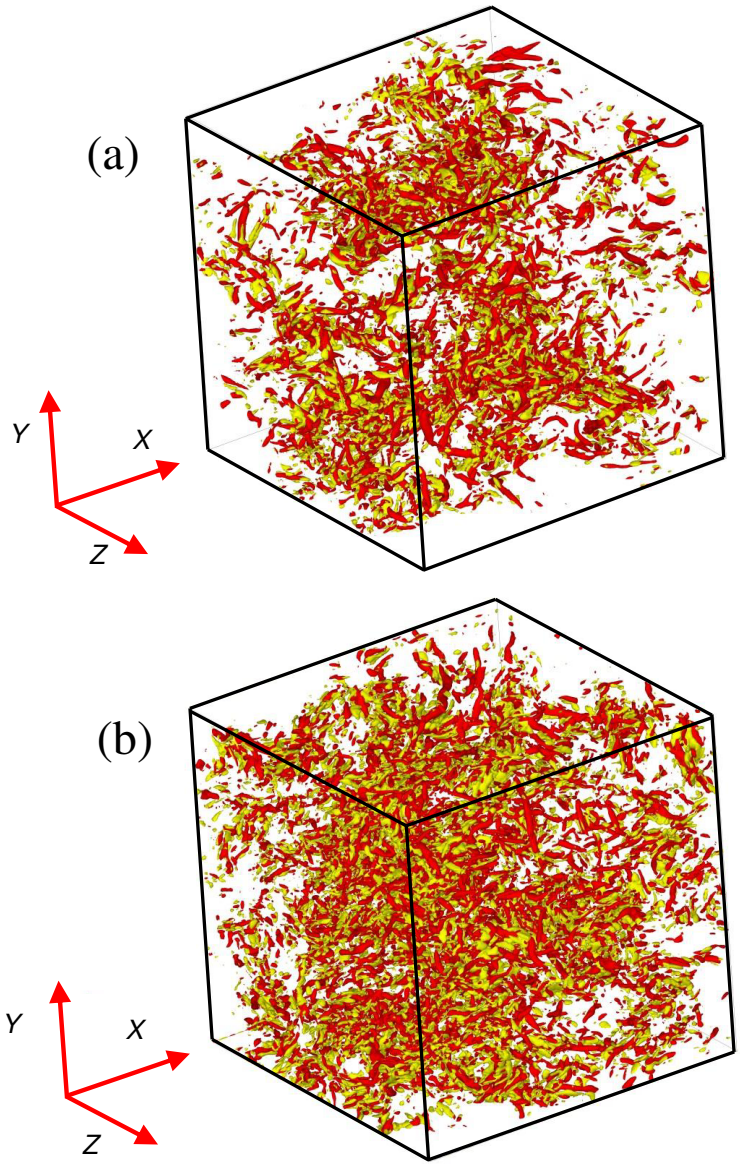

Figure 4.4: Isosurfaces of Q in the regions $11 \leq X/L_0 \leq 13$ and $-1 \leq Y/L_0, Z/L_0 \leq 1$: (a) single square grid, and (b) fractal square grid. Values of $QL_0^2/U_{in}^2 = 9$ (red) and $QL_0^2/U_{in}^2 = -9$ (yellow) are shown.

4.3 Vertical Distributions

The vertical distributions of mean velocity U and rms velocity u_{rms} are presented in this section to study the evolutions of turbulent flow generated by the fractal square grid, with particular emphasis in the near field region $X/X_* \leq 0.6$ ($L/L_0 \leq 5.64$). To make a detailed comparison, the profiles of the single square grid are also plotted.

Figures 4.5 and 4.6, respectively, show the vertical profiles of the normalized mean streamwise velocity U/U_{in} and the normalized turbulence intensity u_{rms}/U_{in} at five different streamwise locations ($X/X_* = 0.1, 0.2, 0.3, 0.6$, and 1.4). As might be expected, Fig. 4.5 shows that the profiles of mean velocity at $X/X_* = 0.1$ ($X/L_0 = 0.94$) for both grids are highly non-uniformly distributed. And both jet-like and wake-like behavior is obtained. Note that at $X/X_* = 0.1$ ($X/L_0 = 0.94$), the vertical variations of the mean flow are more conspicuous for the fractal square grid owning to the smaller square grids. However, after a relatively short distance at $X/X_* = 0.6$ ($X/L_0 = 5.64$), the mean velocity behind the fractal square grid becomes more homogeneous. The same conclusion can also be made for the turbulence fluctuations as shown in Fig. 4.6. Therefore, the fractal square grid indeed has a better mixingperformance in the upstream region.

Our findings are in qualitative agreement with the experimental data of Krogstad and Davidson,[17] who studied turbulent flows generated by two fractal cross grids and one regular grid. It was shown that immediately behind the grid at $X = 50$ mm, all the grids have roughly the same level of inhomogeneity in the mean velocity (see Fig. 2 of their paper). However, at a distance of $X = 150$ mm in the near field, the U of both fractal cross grids was considerably more uniformly distributed (see Fig. 3 of their paper). These results led Krogstad and Davidson[17] to regard the fractal grids as efficient mixers of the mean momentum in the near field. A more detailed discussion concerning the mixing performance of the fractal square grid is given later.

A detailed examination of Fig. 4.5 reveals that the vertical locations of the minimum value vary with the streamwise location. This suggests that in both cases there is a mean flow away from the centerline, although the cross-stream movement is more discernible for the single square grid.

The other point to note in Fig. 4.6 is that the fluctuation levels are distinctly higher for the fractal square grid at least in the region $X/X_* \leq 0.6$ ($X/L_0 \leq 5.64$). There are two possible reasons for this: the higher blockage ratio of the fractal square grid (36%) compared with the single square grid (11%), and, less evident, the additional turbulence generated by the smaller wake interactions. Krogstad and Davidson[17] have already demonstrated that even if the two grids have the same blockage ratio, multiscale grids generate distinctly higher turbulence levels in the near field region (see Fig. 2 of their paper). Moreover, Gomes-Fernandes *et al.*[27] showed that the turbulence intensity behind the fractal square grid would be enhanced with a 5% free-stream turbulence intensity compared with those without inlet free-stream turbulence. Hence, we can infer that the additional turbulence generated by the smaller wake interactions also contributes to the higher turbulence intensities close to the fractal square grid.

Note that in spite of the different turbulence intensity levels at $X/X_* = 0.6$ ($X/L_0 = 5.64$), the single and fractal square grids have a comparable u_{rms}/U_{in} at $X/X_* = 1.4$ ($X/L_0 = 13.16$). This would suggest that the two turbulent flows have quite different energy decay rates in the region $0.6 \leq X/X_* \leq 1.4$ ($5.64 \leq X/L_0 \leq 13.16$).

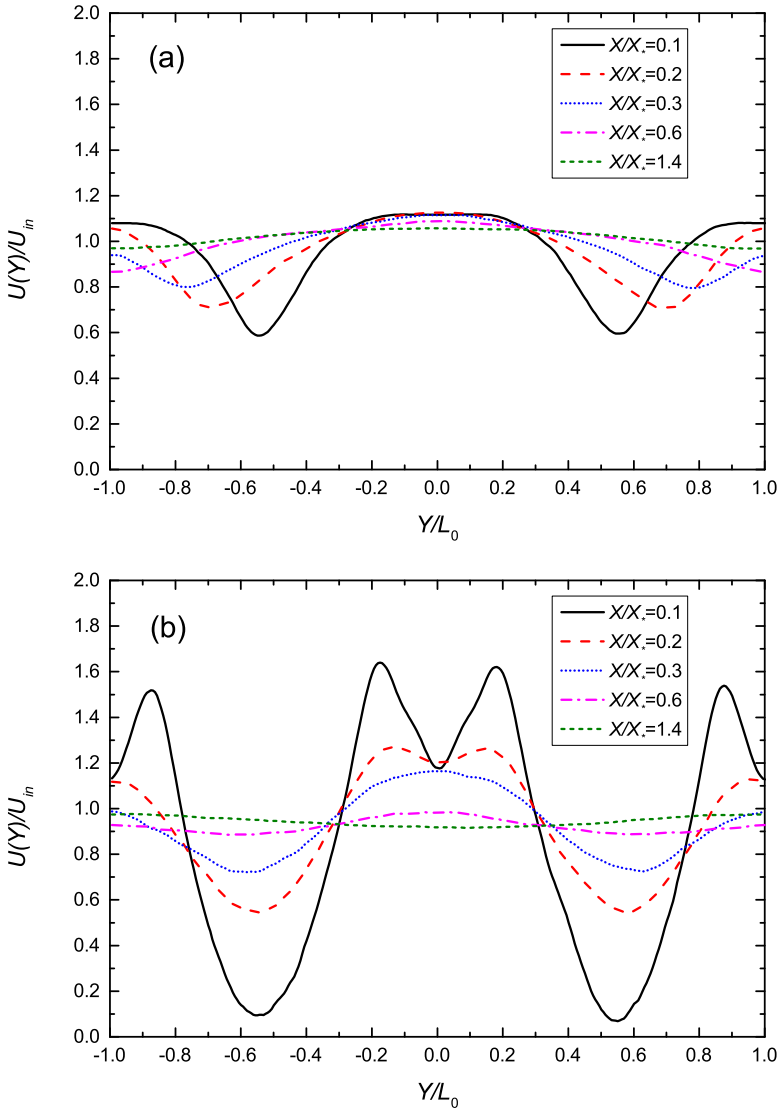

Figure 4.5: Vertical distribution of the normalized mean velocity $U(Y)/U_{in}$ at $X/X_* = 0.1, 0.2, 0.3, 0.6$, and 1.4 for the region $Z = 0$. (a) single square grid and (b) fractal square grid.

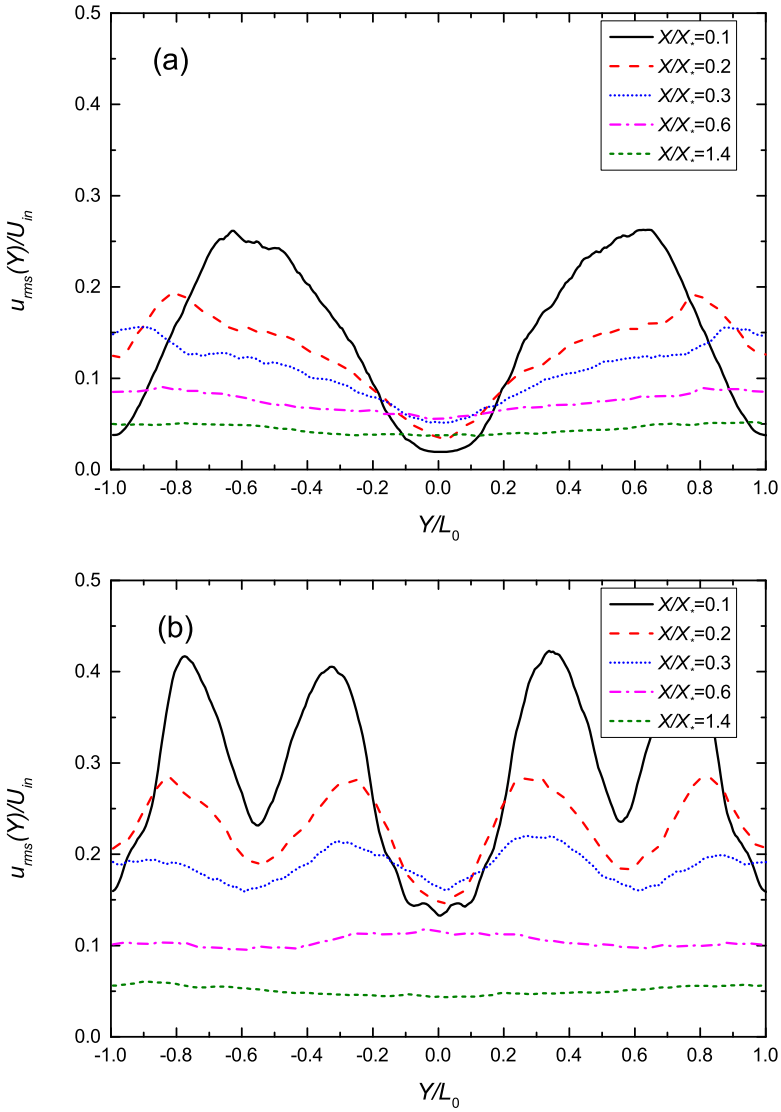

Figure 4.6: Vertical distribution of the normalized turbulence intensity $u_{rms}(Y)/U_{in}$ at $X/X_* = 0.1, 0.2, 0.3, 0.6$, and 1.4 for the region $Z = 0$. (a) single square grid and (b) fractal square grid.

4.4 Centerline Statistics

In this section, the streamwise evolution of various statistics (e.g., mean velocity U, Taylor microscale λ, and turbulence Reynolds number Re_λ, etc.) along the centerline are discussed.

4.4.1 Mean streamwise velocity

Figure 4.7 shows the streamwise evolution of the normalized mean velocity U/U_{in} for the single and fractal square grids along the centerline. The development of mean velocity is quite different and strongly depends on the geometry of the grid used. Immediately behind the fractal square grid, U/U_{in} is considerably larger than 1, which is introduced by the relatively small opening zone close to the centerline (see Fig. 2.11). At the end of the simulation section X/X_*= 1.4 (X/L_0= 13.16), the values of U/U_{in} are 1.05 and 0.92 for the single grid and fractal square grids, respectively. The relatively large values of U/U_{in} observed in the case of the single square grid are due to the persistence of jet-like behavior to the furthermost downstream. Obviously, this jet-like behavior is introduced by the large opening in the center of the single square grid. See chapter 3 for more detailed information.

Our simulation result of U/U_{in} along the centerline for the fractal square grid is inconsistent with the experimental result for the fractal square grids; the typical values of U/U_{in} are found to be a slightly larger than 1.0 in previous experiments. [23,25,28] In Fig. 4.3, there is a wake-like velocity distribution at $X/X_* = 1.4$ ($X/L_0 = 13.16$). In contrast, experimental data from Nagata *et al.*[28] suggest a fundamentally different distribution; in the central region away from the boundary layer, a slight jet-like velocity distribution is found at $X/X_* \geq 0.45$ ($X/L_0 \geq 6.3$). We guess that this inconsistency is introduced by the different boundary conditions in the simulation and experiments. In current study, the periodic boundary conditions are used and the effects of the boundary layers on the solid walls in wind tunnel experiments do not exist here. Nagata *et al.*[28] reported a non-negligible influence of the displacement thickness of the wall boundary layer on the profile of the mean velocity along the centerline (but not on the profiles of other turbulence statistics along the center-

line). Valente and Vassilicos[26] also demonstrated that the effective chocking of the wind tunnel because of the developing boundary layers may affect the turbulence development to some extent.

One interesting finding is that in spite of different boundary conditions and blockage ratios in current numerical simulations and previous experiments, the turbulent flows generated by the fractal and single square grids have a plateau of mean velocity as found in previous experiments of fractal square grids.[23,25,28] This observation is not surprising since in chapter 3, we suggest that the generation of the plateau is associated with the adoption of typical mean velocity profile for jet in the near field region.

4.4.2 Turbulence Intensity and Turbulence Intensity Peak

Figure 4.8 shows the streamwise evolution of the turbulence intensity u_{rms}/U along the centerline for the single and fractal square grids. Figure 4.8 suggests that the fractal square grid produces much higher turbulence intensity u_{rms}/U in the near field region than that of the single square grid. One interesting finding is that even the two grids possess quite different blockage ratios, the difference in u_{rms}/U is small at the end of the simulation section $X/X_* = 1.4$ ($X/L_0 = 13.16$), as already shown by the vertical profiles in Fig. 4.6.

In the present DNSs, the turbulence peak locations X_{peak}/X_*, beyond which u_{rms}/U starts to decrease, are 0.45 and 0.35 for the single and fractal square grids, respectively. The comparable values of X_{peak}/X_* in Fig. 4.9 are consistent with the assertion by Mazellier and Vassilicos[25] that the location of turbulence peak for the fractal square grid is mainly decided by the wake interactions of the largest grid bars. Note that the first peak of turbulence intensity just behind the fractal square grid in the present DNS result is due to the wake interactions of the smallest grid bars located close to the centerline (see Fig. 2.11(b) in chapter 2). In Fig. 4.9, the corresponding experimental data from Mazellier and Vassilicos[25] and Nagata *et al.*[28] are also plotted to make a comparison.

Our simulation results indicate that X_{peak}/X_* for the fractal square grid is slightly smaller than for the single square grid. Owning to the multiscale structure

of the fractal square grid, wakes of different sizes are generated. Figure 4.1 shows that before the interactions of the largest wakes, the wakes of small grid bars have already met and stirred turbulence. Note that Gomes-Fernandes *et al.*[27] presented that the development of wakes would be enhanced with 5% free-stream turbulence intensity compared with those with no inlet free-stream turbulence. For the case of a fractal square grid, the additional turbulence contribute to the development of the largest wakes and these wakes meet closer to the grid. Hence, the slight smaller X_{peak}/X_* for the fractal square grid is reasonable.

In Table 4.1, we list X_{peak}/X_* for the single square, regular, and fractal square grids. Note that Table 4.1 suggests that, similar to the case of the single square grid, a relatively larger value of X_{peak}/X_* is also found for the regular grid. We expect that the lack of the additional turbulence is responsible for this large X_{peak}/X_*.

4.4.3 Large-Scale and Small-Scale Anisotropy

Figure 4.10 shows the streamwise evolution of the large-scale anisotropy u_{rms}/v_{rms} along the centerline. For both grids, u_{rms}/v_{rms} are close to 1 at $X/X_* \geq 0.6$ (see Fig. 3.5 for the single square grid). The large-scale anisotropy for turbulence generated by the single square grid is in the range of 0.95–1.0 at $X/X_* \geq 0.6$ (also see Fig. 3.5), whereas a relatively large and more conventional value (1.05–1.10) is obtained in the fractal square grid case. The simulation result here for the fractal square grid is close to the corresponding experimental values for the fractal square grid[23–26,28] and the regular grid.[12,14–16]

Figure 4.10 also shows the streamwise evolution of the small-scale anisotropy K along the centerline. Data from the fractal square grid experiment of Valente and Vassilicos[26] are also presented to make a comparison. According to the hypothesis proposed by Kolmogorov, for turbulent flow at sufficiently large Reynolds numbers, the small scales are locally isotropic and K equals to 2. As shown in Fig. 4.10, our simulation results are in good agreement with the experimental data, especially in the region $X/X_* \geq 0.8$. Generally speaking, our simulation results of K for the single square grid (see Fig. 3.5) and the fractal square grid are comparable.

4.4.4 Skewness and Flatness

Owning to the energy decay, for grid turbulence the values of the skewness S_u and the flatness F_u are slightly different from the corresponding values of the Gaussian distribution. Previous experiments of the fractal square grids[25,28] suggested that in the downstream region, S_u is a bit larger than 0 and F_u is slight smaller than 3. Note that Kitamura *et al.*[16] demonstrated that for regular grids, S_u approaches 0 at far downstream of $X/M \simeq 50$. Figure 4.11 shows that for the fractal-generated turbulence, S_u and F_u are close to the corresponding values of Gaussian distributions in the region corresponding to $X/X_* \geq 0.6$ ($X/L_0 \geq 5.64$). Moreover, we have already presented that reasonable isotropy and homogeneity are also found in this region. Hence, in the following investigation of the decay rates, data in this region are used.

Another finding is that for the fractal square grid at $X/X_* \simeq 0.2$, S_u and F_u possess relatively large magnitude, which suggests the existence of extreme/intense events. And the shapes of the profiles of S_u and F_u are similar to those of the single square grid (see Fig. 3.4). This result is not surprising, considering the conclusion in chapter 3 that the turbulence characteristics are mainly determined by the largest wake interactions at $X/X_* \geq 0.2$. Since both two grids have exactly the same biggest square grid, the similar tendencies of S_u and F_u are reasonable.

4.4.5 Taylor Microscale

Figure 4.12 shows the streamwise evolution of the normalized Taylor microscale λ/L_0 along the centerline for the single square grid and the fractal square grid. The most interesting finding in Fig. 4.12 is that in spite of different grid patterns, there is excellent agreement of λ/L_0 beyond $X/X_* = 0.2$ ($X/L_0 = 1.88$). Experimental results suggested that there is good agreement of the normalized Taylor microscale λ/L_0 in the region $X/X_* \geq 0.2$ ($X/L_0 \geq 1.88$) along the centerline for fractal square grids even with different geometric parameters (see Fig. 7 in previous paper[28]). Here, for the single and fractal square grids, we have the similar observation. Note that the two grids have the same largest grids (but have quite different blockage ratio σ).

Hence, the relatively good agreement of λ/L_0 in our numerical study and previous experiments confirm our conclusion again that beyond $X/X_* = 0.2$ ($X/L_0 = 1.88$), turbulent motions are mainly determined by the largest wake interactions. The small grid bars of the fractal square grid exert a negligible effect on the normalized Taylor microscale λ/L_0 at $X/X_* \geq 0.2$ ($X/L_0 \geq 1.88$).

4.4.6 Turbulent Reynolds Number

In Fig. 4.13, we compare the turbulent Reynolds number $Re_\lambda (= u_{rms}\lambda/\nu)$ for the single square case with that for the fractal square case along the centerline. Since in the region corresponding to $X/X_* \geq 0.2$ ($X/L_0 \geq 1.88$), the profiles of the Taylor microscale λ of the single and fractal square grids are approximately similar, the difference in Re_λ is only introduced by the different values in u_{rms}. Similar to u_{rms}, near the grid, Re_λ of the fractal square grid is distinctly higher than that of the single square grid, whereas at $X/X_* = 1.4$ ($X/L_0 = 13.16$) comparable values are found because of the different decay rates.

Previous study[15] suggested that for the homogeneous and isotropic turbulence, we can roughly estimate the power law decay exponent n through the profile of Re_λ (see Eq. (4.2) in their paper). For instance, the energy decay exponent n takes the value of 1, corresponding to a constant value of Re_λ with the streamwise distance X/X_*. In the following subsection, a more detailed description of n will be given. When n is close to 1, the decay rate of Re_λ is small. In contrast, if n is much larger than 1, a remarked high decay rate of Re_λ is expected. For the single square grid, Fig. 4.13 shows that Re_λ remains roughly constant, which seems to suggest that the corresponding decay exponent does not deviate significantly from 1. However, in the case of the fractal square grid, Re_λ possesses a distinctly larger decay rate than that of the single square grid, which implies that the corresponding n is considerably larger than 1. A detailed discussion of n for the two grids will be presented in the next section.

Table 4.1: Turbulence intensity peaks X_{peak} for the single square, fractal square, and regular grids.

Grid type	Ref.	Re_M ($\times 10^{-3}$)	Re_{L_0} ($\times 10^{-3}$)	σ (%)	M (mm)	L_0 (mm)	U_{in} (m/s)	X_{peak}/X_*
Single square	Fig. 4.8	–	20	11	–	80	3.75	0.45
Fractal square	Fig. 4.8	–	20	36	–	80	3.75	0.35
Regular	Ref. 33	230	–	17	230	–	15	0.63
Fractal square	Ref. 25	–	82	25	–	238	5.2	0.45
Fractal square	Ref. 28	–	160	25	–	164	15	0.45
Fractal square	Ref. 33	–	237	25	–	238	15	0.45

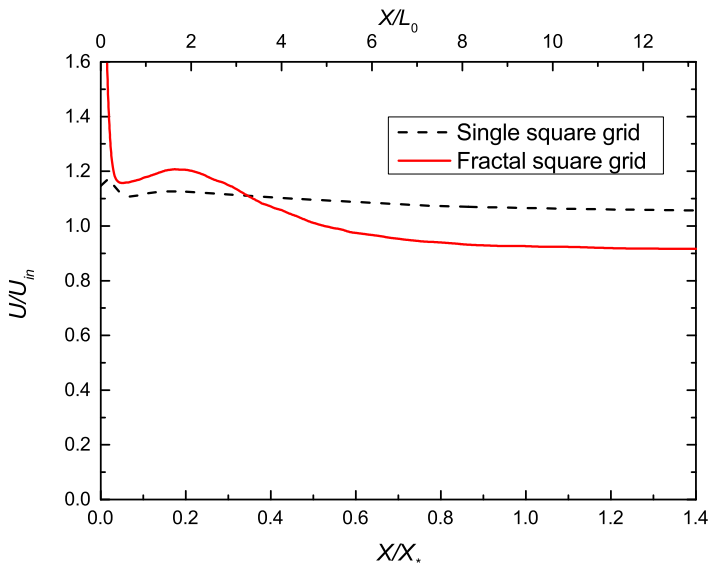

Figure 4.7: Streamwise evolution of the normalized mean velocity U/U_{in} along the centerline for both grids.

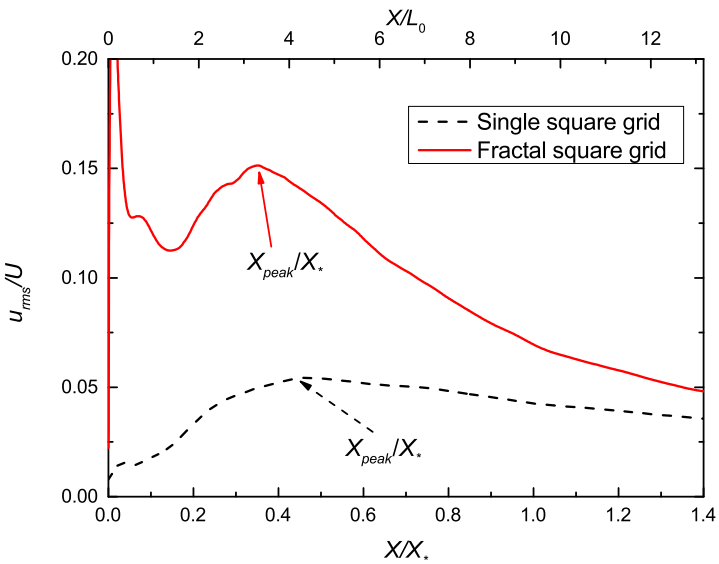

Figure 4.8: Streamwise evolution of the turbulence intensity u_{rms}/U along the centerline for both grids.

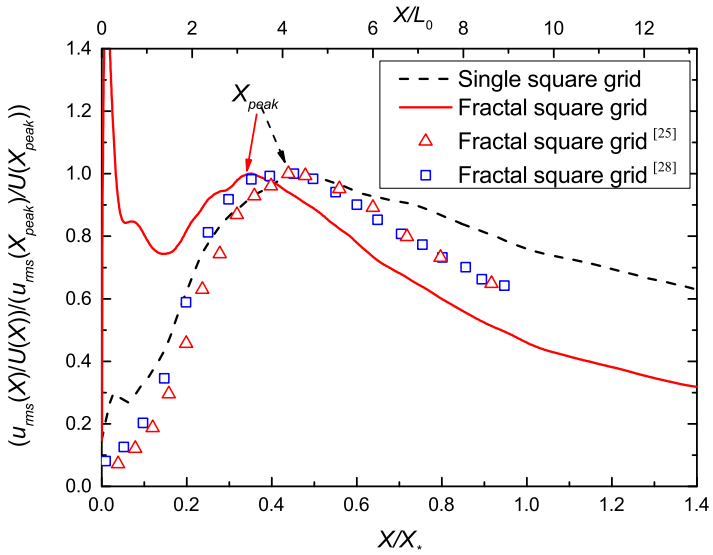

Figure 4.9: Streamwise evolution of the turbulence intensity along the centerline, normalized by its value at $X = X_{peak}$. For the normalized turbulence intensity: the single square grid in chapter 3 (dashed line), the fractal square grid in this chapter (solid line), the experiment of Mazellier and Vassilicos [25] (open triangle), and the experiment of Nagata *et al.* [28] (open square). Note that in Fig. 4.9, the streamwise distance from the grid X for regular grids is only non-dimensionalized by the interaction length scale X_* (see the lower X axis). Detailed experimental conditions of Mazellier and Vassilicos [25] and Nagata *et al.* [28] are listed in Table 4.1.

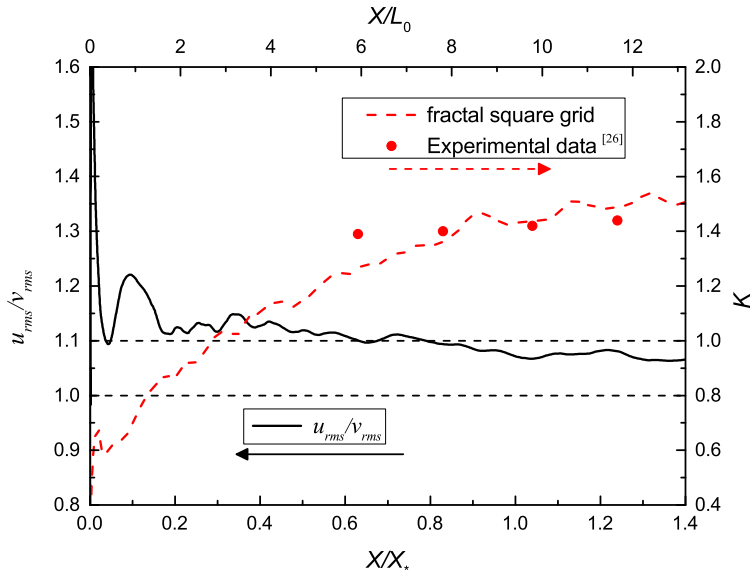

Figure 4.10: Streamwise evolution of the large-scale anisotropy u_{rms}/v_{rms} and the small-scale anisotropy K along the centerline for turbulence generated by the fractal square grid. Symbols: experimental data K for the fractal square grid by Valente and Vassilicos.[26]

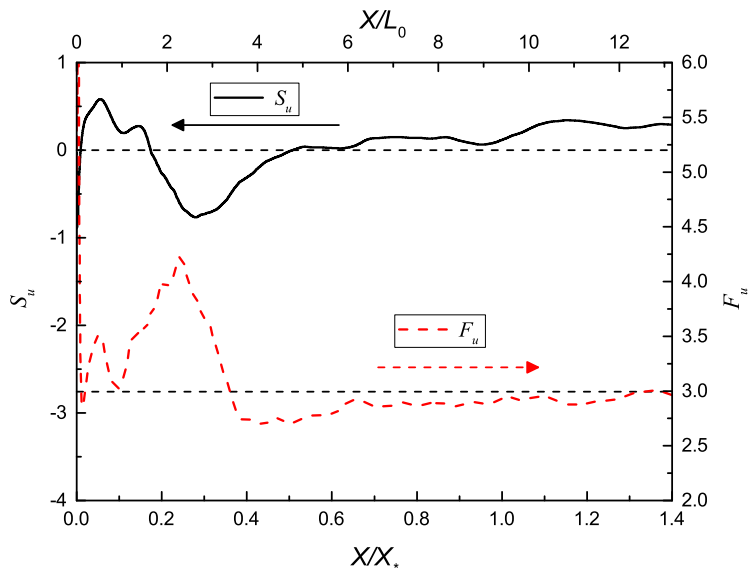

Figure 4.11: Streamwise evolution of the skewness and the flatness along the centerline for turbulence generated by the fractal square grid.

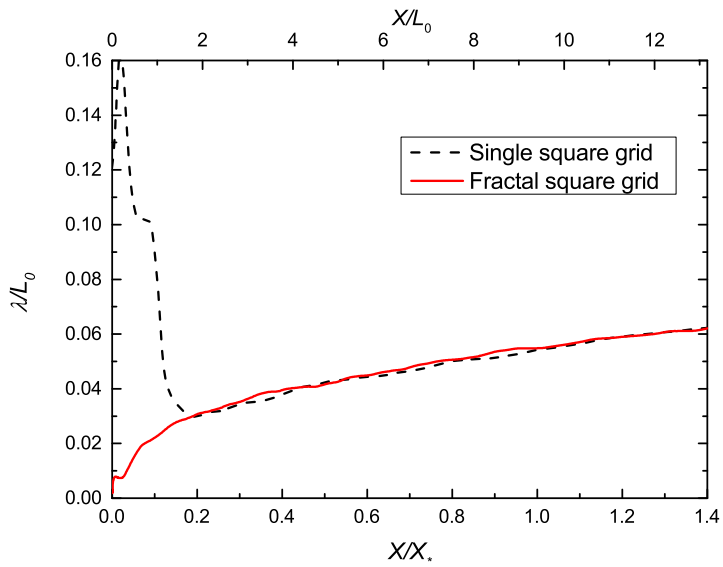

Figure 4.12: Streamwise evolution of the normalized Taylor microscale λ/L_0 along the centerline for both grids.

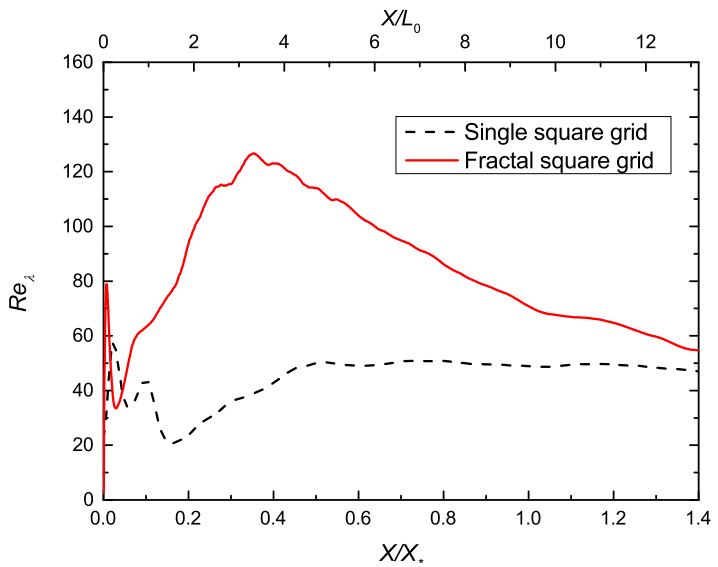

Figure 4.13: Streamwise evolution of the turbulent Reynolds number Re_λ along the centerline for both grids.

4.5 Energy Decay Rate

In this section, we will estimate the energy decay exponents n for both grids. The following power law is widely used to study the energy decay rate for the grid turbulence.

$$\frac{u_{rms}^2}{U_{in}^2} = a(X/L_0 - X_0/L_0)^{-n}, \tag{4.5.1}$$

where a is a constant and X_0 is the virtual origin. Previous studies[15,30] have shown that it is difficult to obtain the reliable values of n in the power decay law. Sometimes, a wide range of values of a, X_0, and n may exist that can lead to virtually the same level of fitting accuracy.[15] To make things worse, in our study owning to the finite streamwise range of X/L_0, the decay exponent n is really sensitive to the choice of X_0. Here, two different methods are used to determine X_0/L_0 and then estimate the decay exponent n.

The first method (method 1) is based on the linear fitting method used by Valente and Vassilicos.[26] In homogeneous isotropic turbulence, we can obtain the following equation

$$\frac{\lambda^2}{L_0^2} = \frac{1}{L_0}\frac{10\nu}{nU}(X/L_0 - X_0/L_0), \tag{4.5.2}$$

Detailed derivation of this equation can be found in previous paper.[26] When applying this method to determine X_0, first we need to confirm the linear variation of $U\lambda^2$ with the streamwise distance. Figure 4.14 shows that for both grids, $U\lambda^2$ indeed exhibits reasonable linear growth. Note that the very good agreement of λ is found in the region $0.6 \leq X/X_* \leq 1.4$ for the single and fractal square grids as shown in Fig. 4.12. Hence the difference in $U\lambda^2$ between the single square grid and the fractal square grid is related to the different profiles of the mean velocity U along the centerline (see Fig. 4.7). Then, X_0 is obtained by the linear fit of $U\lambda^2$ in the above equation. Based on the value of X_0, we can determine the exponent n by another linear fit to the power decay law Eq. (4.5.1).

In our second method (method 2), the assumption $X_0/L_0 = 0$ is made. Note that there is no proof that the virtual origin will coincide with the grid location. Hence, this method would return a biased decay exponent n as shown by Valente and Vassilicos.[26] However, based on this assumption, we have a robust method to

obtain first order estimate of the decay exponent and the result is not far from the predictions when adopting other estimation methods.

Figure 4.15 shows the streamwise evolution of kinetic energy along the centerline and the power law fits. As shown in Fig. 4.15, the corresponding data are well fitted using both methods. And the values of X_0 and n for the single and fractal square grids following these two methods are listed in Table 4.2. As expected, Table 4.2 shows that the decay exponents obtained by two methods are not the same. Decay exponents for the single and fractal square grids from the method 1 are relatively larger than those from the method 2. Nevertheless, these differences would not meaningfully change our conclusion; the decay exponent for the single and fractal square grids are clearly different. The decay exponent n of turbulence generated by the fractal square grid is much larger than the corresponding value in the case of the single square grid.

The unusual large value of n for the fractal square grid is not surprising. Note that previous experiments have shown that at sufficiently large inlet Reynolds number, turbulence generated by various kinds of grids (e.g., regular grid,[17,33,62] fractal square grid,[23,25,28,33] and fractal cross grid[17]) possess high energy decay rate immediately beyond the turbulence intensity peak X_{peak}. This region is also referred to as the non-equilibrium region.[33] In this region, the classical power decay law does not hold. Our simulation result for the fractal square grid verifies the existence of the so called non-equilibrium region.

However, for the single square grid, the generated turbulent flow possesses a more conventional decay exponent n; n takes the value of 1.25 or 0.97 depending on the estimation method used. We guess that this relative small n for the single square grid may be associated with the relatively low local Reynolds number Re_λ. Figure 4.13 shows that the fractal square grid has much higher Re_λ than that of the single square grid at X_{peak}. Future study is required to clarify the dependence of Re_λ on n for the single square grid.

Table 4.2: Estimates of decay exponents using two different methods.

Grid type	Method 1		Method 2	
	n	X_0/L_0	n	X_0/L_0
Single square	1.25	-2.07	0.97	0.00
Fractal square	3.31	-3.95	2.23	0.00

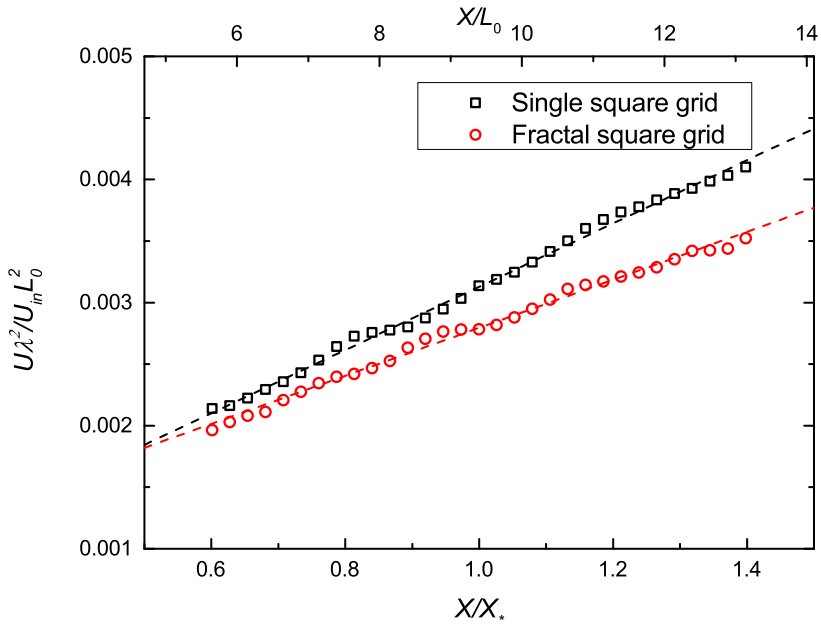

Figure 4.14: Streamwise evolution of $U\lambda^2/U_{in}L_0^2$ along the centerline and the corresponding linear fit (dashed line).

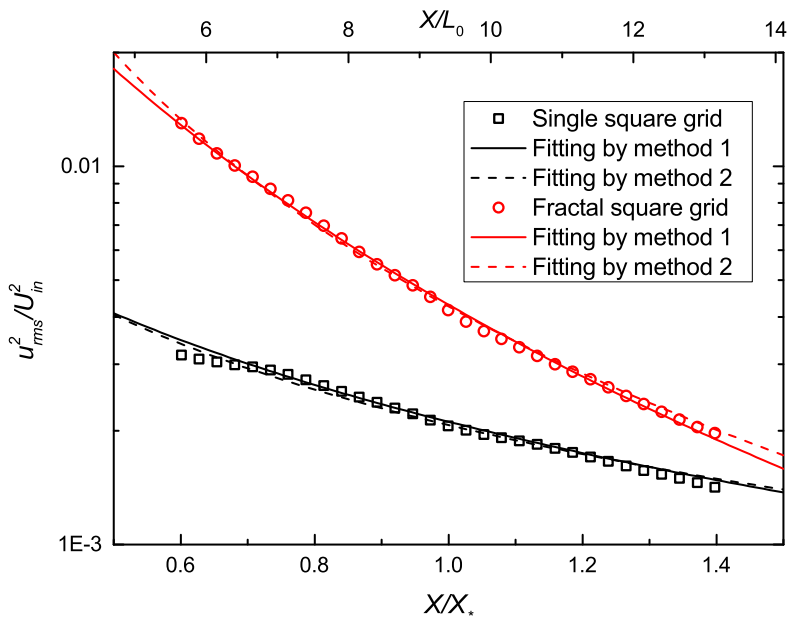

Figure 4.15: Streamwise evolution of kinetic energy along the centerline and the power law fit using method 1 (solid line) and method 2 (dashed line).

4.6 Characteristic Length Scale

Figure 4.1 shows that for the regular and single square grids, each mesh produces same wakes and jets. And all these generated wakes meet each other at the same downstream location. Thus, we can simply use the mesh size M to describe the structure of a regular grid. Based on the mesh size M, the definition of the inlet Reynolds number is explicit. In previous experiments, to study regular grid turbulence at different inlet Reynolds numbers, researchers can either manipulate the inlet velocity U_{in} or the mesh size M.

Behind the fractal square grid, in contrast, wakes and jets of different sizes are found. Wakes generated by grid bars of different sizes interact at different distances from the grid. Previous studies[25,26,28,34,41] suggested that there are more than one length scale for the fractal square grid depending on what we want to scale. For instance, Laizet and Vassilicos[41] showed that the cross-sectional averaged turbulence intensity peaks at one M_{eff} from both regular and fractal grids. Nagata *et al.*[34] also found that both cross-sectional averaged turbulent kinetic energy and enstrophy reach their peaks at approximately one M_{eff} from both regular and fractal grids. The wake-interaction length scale X_* is a good estimator of turbulence intensity peak location along the centerline.[25,28] Actually, Nagata *et al.*[28] presented that when the distance from the grid X is normalized by X_*, data from other statistics (e.g., the skewness S_u, the flatness F_u, the Taylor microscale λ, and the integral length scale L_u) along the centerline are also similar for fractal square grids with different geometric characteristics. And the longitudinal integral length is approximately one fifth of the length of the largest grid bar L_0 and remains unchanged in the decay region.

Hence, it is difficult to give a clear definition of the inlet Reynolds number for turbulence generated by the fractal square grid. To solve this problem, Hurst and Vassilicos[23] firstly proposed the effective mesh scale M_{eff} for characterizing the geometry of the fractal square grid. For regular grids, the effective mesh size M_{eff} reduces to the mesh size M. Consequently, there comes the same results when using M_{eff} or M to describe the inlet Reynolds number of the regular grid. Note that this definition just takes into account of the geometrical factors of a fractal grid

(see Eq. (2.1.1)). In chapter 3 and this chapter, it has been repeatedly confirmed that for the fractal square grid, the largest wakes play a dominant role in turbulence development. Therefore, we propose that it is the length of the largest bar L_0, not the effective mesh size M_{eff}, which may give a physical description of the inlet Reynolds number.

Note that this discussion on the characteristic length scale for the inlet Reynolds number is not trivial. It is associated with probably the two most important properties of turbulence generated by the fractal square grid.

First, it is related to the debate of the possibility of a new type of turbulence. See papers[17,32,33] for more information on the unusual energy decay for fractal-generated turbulence. As mentioned in chapter 1, in previous studies of regular grid turbulence, data were measured at $X/M > 25$–30 to avoid the influences of the non-equilibrium region near the grid. To our knowledge, the furthermost downstream location investigated for the fractal square grid is $X \simeq 202M_{eff}$,[26] which corresponds to $X \simeq 22.3L_0$. When applying the above mentioned conventional measurement criteria that data should be obtained at $X/M > 25$–30 to the case of the fractal square grid, the streamwise extent of tested region[26] ($X \simeq 22.3L_0$) is still in the near field region. Owing to the large value of L_0 (i.e., $L_0/D = 1/2$), the investigations of fractal-generated turbulence do not meet the requirements proposed by Corrsin.[19] Corrsin[19] suggested that the size of the wind tunnel D should be much larger than the mesh size of the grid M, that is $D/M \gg 1$, and experiment data should be taken in the far downstream location. Hence, for the fractal-generated turbulence the classical theories of homogeneous isotropic turbulence cannot be applied.

Experimental evidences[17,33] suggested for both regular and multiscale grids (i.e., the fractal square grid and the multiscale cross grid), unusual high decay behavior is found in the near field regions. Moreover, Krogstad and Davidson[17] presented that in the tested region far away from multiscale cross grids, the classical decay law can be recovered. Based on previous discussions, we could make the conclusion that the nonclassical fast energy dissipation behavior for the fractal square grid is associated with a finite measurement region. We expect that in sufficiently far downstream

region of the fractal square grid (i.e., $X/L_0 = 50$), the well known power decay law as observed by Comte-Bellot and Corrsin[12] can be found.

Second, the discussion of the characteristic length scale is associated with the unusual high turbulent Reynolds number Re_λ and turbulent energy levels downstream of the fractal square grid. Both experimental and numerical studies[23–25,34,35,38–40] suggested that fractal square grids can generate unusual higher turbulence intensities and Re_λ than the regular grids with a higher blockage ratio σ. Note that previous studies use the effective mesh size M_{eff} to describe the inlet Reynolds numbers for the regular grid and the fractal square grid. Compared with the length of the largest grid bar L_0, the effective mesh size based Reynolds number $Re_{M_{eff}} = U_{in}M_{eff}/\nu$ significantly underestimates the inlet Reynolds number. As we shall see in Table 4.3, the single square grid, the fractal square grid, and the regular grid have comparable Re_λ and u_{rms}/U_{in} at X/L_0 or $X/M \simeq 13$, if choosing L_0 to characterize the inlet Reynolds number.

Finally, we stress that the validity of using the length of largest grid bar L_0 to characterize the fractal square grid is based on the dominance of the largest wakes. It is expected that for the fractal square grid with a thickness ratio t_r much smaller than 8.5, immediately behind the grid, similar wakes are generated from all grid elements. The lack of the dominance of wakes generated by the largest grid may result in different turbulence generation mechanism.

Table 4.3: Re_λ and u_{rms}/U_{in} for the single square, regular, and fractal square grids.

Grid type	Ref.	Re_M ($\times 10^{-3}$)	Re_{L_0} ($\times 10^{-3}$)	σ (%)	t_r	M (mm)	L_0 (mm)	U_{in} (m/s)	X/M X/L_0	u_{rms}/U_{in} (%)	Re_λ
Single square	Chapter 3	–	20	11	–	–	80	3.75	13.2	3.8	47
Fractal square	Chapter 4	–	20	36	8.5	–	80	3.75	13.2	4.4	54
Regular	Ref. 33	153	–	17	–	230	–	10	13.7	4.8	200
Fractal square	Ref. 23	–	158	25	13	–	238	10	13.8	4.5	200
Fractal square	Ref. 28	–	160	25	13	–	164	15	13.2	4.8	220
Regular grid	Ref. 33	230	–	17	–	230	–	15	13.7	4.8	258
Fractal square	Ref. 33	–	237	25	17	–	238	15	13.5	5.0	249
Regular	Ref. 33	268	–	17	–	230	–	17.5	13.7	4.8	281
Fractal square	Ref. 33	–	277	25	17	–	238	17.5	13.5	5.0	275

4.7 Summary

The main findings of this chapter can be summarized as follows.

1. Our simulation results confirm the existence of the unusual energy decay behavior behind the fractal square grid, where turbulent flows have unusual high decay exponents n.

2. The fractal square grid can indeed stir higher turbulence levels in the near field region, whereas the values of Re_λ and u_{rms}/U_{in} of the single and fractal square grids at the end of simulation section (i.e., $X/X_* = 1.4$ or $X/L_0 = 13.2$) are comparable.

3. We assume that the turbulence owning to the small wake interactions just behind the fractal square grid can be regarded as the additional turbulence.

Although persisting for a finite streamwise extent downstream of the grid, the remarkably high turbulent Reynolds numbers and fluctuation levels generated by the fractal square grid are appealing for industrial applications. Currently, our research group have observed a high mixing rate for the multiscale/fractal grid.[43,44] We believe that the findings presented in this paper contribute to the development of a high-performance industrial devices such as a static mixer.

Chapter 5

Single-Square Grid-Generated Turbulence with Additional Turbulence[49,50]

In chapters 3 and 4, we confirm the assumption proposed by Mazellier and Vassilicos[25] that the wakes in the lee of the fractal square grid, which exert dominant influences, are those generated by the largest grid bars. Hence, it is suggested that for a typical fractal square grid, turbulence fluctuations because of the small grid bars can be regarded as additional turbulence. And the evolution of the largest wakes behind the biggest grid bars, at least to some extent, can be affected by this additional turbulence. For further investigation, in this chapter we carry out the simulation of the single square grid subject to additional turbulence.

5.1 Additional Turbulence Generation

The homogeneous and isotropic additional turbulence is generated by the inverse Fourier transform[72,73] using the following spectrum

$$E(k) \sim k^4 \exp(-2(k/k_0)^2), \tag{5.1.1}$$

where k is the wavenumber and k_0 is the most energetic wavenumber; here, $k_0 = 5$.

Note that the inlet random velocity field obtained from this procedure is periodic

in all three directions, and to solve this problem, a special treatment is required.[74] Following Lee *et al.*,[75] the phase factor ϕ_r is changed by a random small amount $\Delta\phi_r$ in a given time interval T_r to generate nonperiodic fluctuations in the streamwise direction. The random variation obeys the relationship $|\Delta\phi_r| \leq \Delta\phi_{max} = 1/5\pi$, and the time interval is $T_r = 2\pi/k_0$. The values of $\Delta\phi_{max}$ and T_r are similar to those selected by Lee *et al.*[75] The velocity fluctuations are obtained by two-dimensional Fourier transforms in the Y- and Z-directions followed by a sum over all wavenumbers. Note that because of the temporal dependence of ϕ_r the generated spectrum is not the same as the target spectrum. Here, we confirm that the presence of a k^{-2} tail in the high-k region and a deviation from the target spectrum is found at nonenergetic wavenumbers (for more numerical details, see the paper of Lee *et al.*[75]). The inlet velocity is obtained by adding the artificial homogeneous and isotropic disturbance field to the uniform inlet velocity U_{in}.

The influence of the additional turbulence largely depends on its characteristics, and a previous study[82] suggested that there are two major additional-turbulence parameters that affect the evolution of the embedded wakes. Below, the subscript "et" denotes inflow data values. The first major parameter is the rms velocity $u_{rms,et}$, which is also referred to as the "strength" of the additional turbulence. Here, the turbulent levels of the present mean streamwise velocity U_{in} in the X-, Y-, and Z-directions were 0.097, 0.097, and 0.098, respectively. The second major parameter is the integral length scale L_{et}, which is defined through the longitudinal two-point correlation of the additional turbulence as

$$L_{et} = \int_0^\infty \frac{\langle u'_{et}(x) u'_{et}(x+r) \rangle}{\langle u'_{et}(x)^2 \rangle} dr, \tag{5.1.2}$$

where u'_{et} is the streamwise fluctuation in the artificial homogeneous and isotropic turbulence field. Here, L_{et} is comparable to the thickness of the largest grid bar t_0 ($L_{et} = 1.29t_0$).

5.2 Inclusion of Additional Turbulence

Unless otherwise stated, in this chapter, case 1 and case 2 denote the simulation of turbulence generated by the fractal and single square grids, respectively. An

additional simulation, that of turbulence generated by a single square grid subject to additional artificial turbulence (homogeneous isotropic turbulence with $u_{rms,et}/U_{in} = 0.097$), is performed and is referred to hereafter as case 3. For case 3, the turbulent field near the grid is similar to that of case 1 in that large wakes are embedded in the additional turbulence (fluctuations due to the relatively smaller grids in case 1 and additional artificial turbulence in case 3).

5.2.1 Vertical Distribution of the Mean Velocity

Figure 5.1 shows the vertical distributions of the normalized mean velocity $U(Y)/U_{in}$ at different streamwise locations $X/X_* = 0.1$, 0.2, 0.3, 0.6, and 1.4 for case 3. Compared with the results in Fig. 4.5(a), the wakes in case 3 are flatter than those in case 2, especially at $X/X_* \leq 0.3$ ($X/L_0 \leq 2.82$). Since both case 2 and case 3 have exactly the same grid geometry, we infer from this that the additional turbulence increases the expansion of the large wakes in the upstream region.

It is interesting to note that there has been past research concerning the effects of the additional turbulence on the spatial evolution of the pure wake (wake generated by a solid sphere[76–80] and cylinder[81]and axisymmetric wake[82]). These investigations[76–82] revealed that the additional turbulence can enhance the decay rate of the embedded wakes to some extent. And with the additional turbulence, the wake merges into the surrounding flow within a shorter streamwise distance. Hence, the results in Fig. 5.1 are consistent with previous proposals[76–82] that the additional turbulence can increase the spread of the embedded wakes and lead to a higher mixing speed in the initial region $X/X_* \leq 0.3$ ($X/L_0 \leq 2.82$).

Note that similar additional turbulence is also found behind the multiscale grid, and the existence of this additional turbulence explains the high mixing performance reported by Krogstad and Davidson.[17] One experimental study[26] of the fractal square grid briefly mentioned that the additional turbulence generated by the smaller grids contributes to the development of the largest wakes. The simulation results here support this conclusion.

5.2.2 Centerline Statistics

Figure 5.2 shows the streamwise evolution of the turbulence intensity u_{rms} along the centerline for all three cases. To focus on the decay rates and the values of X_{peak}, we examine the normalized turbulence intensities along the centerline (see Fig. 5.3). The turbulence peaks are at $X_{peak}/X_* = 0.35$, 0.45, and 0.26 (or $X_{peak}/L_0 = 3.3$, 4.2, and 2.4) for cases 1, 2, and 3, respectively.

It is clear that in case 1 and 3, the largest wakes meet and interact at a downstream location closer to the grid than that in case 2. We assume that the large-wake interactions occur further upstream in case 1 and 3 due to a similar physical mechanism; the additional turbulence (the fluctuations generated by the smaller bars in case 1 and the artificial turbulence in case 3) enhances the spreading of the largest wakes. Thus, we have again demonstrate that the presence of additional turbulence increases the spreading of the embedded wakes in the vicinity immediately behind the grid, which indicates a high mixing rate of momentum.

Figure 5.4 shows the streamwise variation of the normalized Taylor microscale λ/L_0 of case 3 along the centerline along with those of case 1 and 2 for comparison. Good agreement is again found in the region $X/X_* \geq 0.3$ ($X/L_0 \geq 2.82$) for case 3, and it would seem that in this region, λ/L_0 is not significantly dependent on the wake-generation patterns shown in Fig. 4.1 but is mainly determined by the geometry of the largest grid.

5.2.3 Energy Decay Rate

Following the two estimation methods used in chapter 4, we estimate the values of X_0 and n in case 3 (see Figs. 5.5 and 5.6) and the obtained results are listed in Table 5.1. For the corresponding values in case 1 and 2, refer to Table 4.2.

The energy decay rates in both case 1 and 3 are considerably larger than the classical observations of Comte-Bellot and Corrsin.[12] Behind the single square grid (case 2), however, the turbulent flow has a more conventional decay rate. It is interesting to note that when additional turbulence is included, a high energy decay region emerges. The existence of this high energy decay region is thus general; it

Table 5.1: Estimates of decay exponents n in case 3 using two different methods.

Grid type	Method 1		Method 2	
	n	X_0/L_0	n	X_0/L_0
Case 3	1.83	-1.21	1.62	0.00

includes but is not limited to the case of the fractal square grid. This conclusion is in agreement with recent experimental findings;[33,62] previous experiments have shown that at a sufficiently large inlet Reynolds number, the turbulence generated by various types of grids (e.g., regular grid,[17,33,62] fractal square grid,[23,25,28,33] and fractal cross grid[17]) possesses a high energy decay rate in the near field.

At last, we need to stress that in case 3, the artificial additional turbulence is homogeneous and isotropic. However, for a typical fractal square grid, the additional turbulence possesses multi-length scales and is far from homogeneous and isotropic. Future study is required to reveal the different impacts of the two types of additional turbulence.

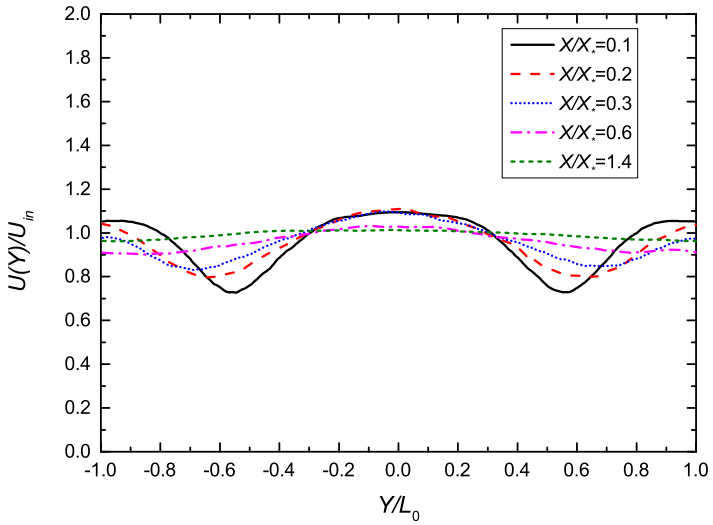

Figure 5.1: Streamwise variation of the vertical distribution of the normalized mean velocity $U(Y)/U_{in}$ at $Z = 0$ for the single square grid with additional turbulence.

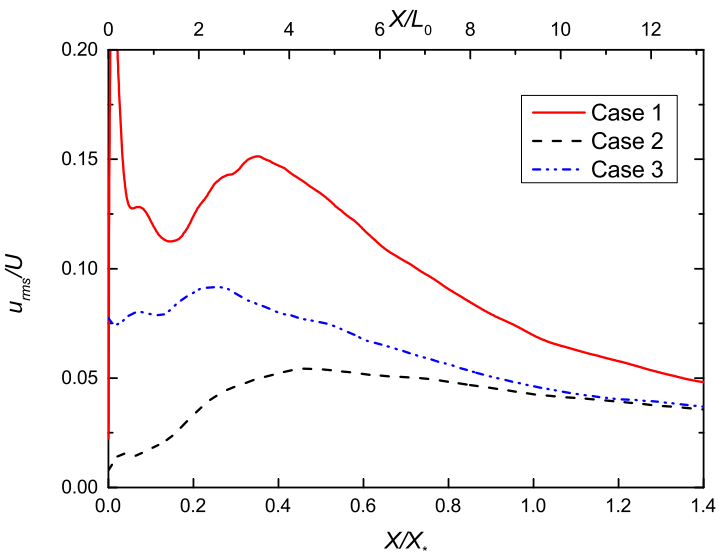

Figure 5.2: Streamwise evolution of the normalized turbulence intensity u_{rms}/U along the centerline for the fractal square grid (case 1), single square grid (case 2), and single square grid with additional turbulence (case 3).

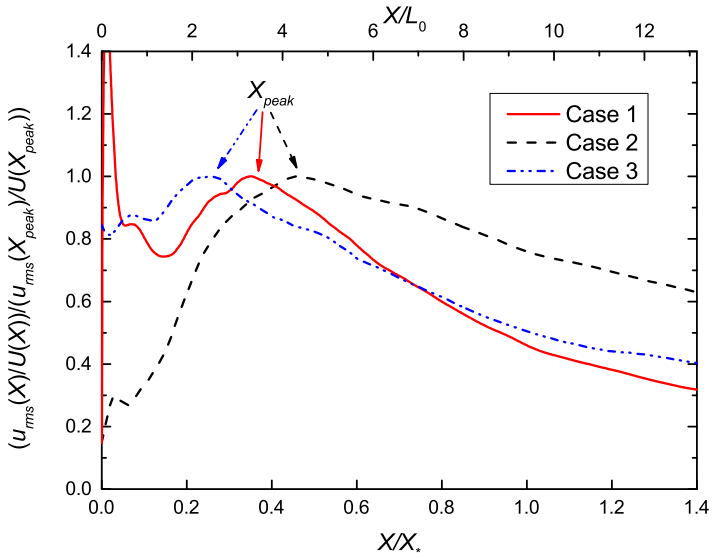

Figure 5.3: Streamwise evolution of the turbulence intensity along the centerline normalized by the maximum value at X_{peak} for the fractal square grid (case 1), single square grid (case 2), and single square grid with additional turbulence (case 3).

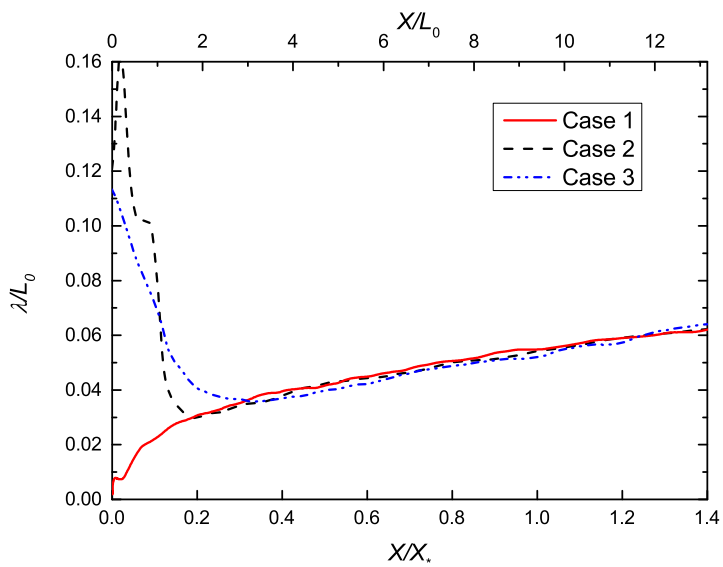

Figure 5.4: Streamwise evolution of the normalized Taylor microscale λ/L_0 along the centerline for the fractal square grid (case 1), single square grid (case 2), and single square grid with additional turbulence (case 3).

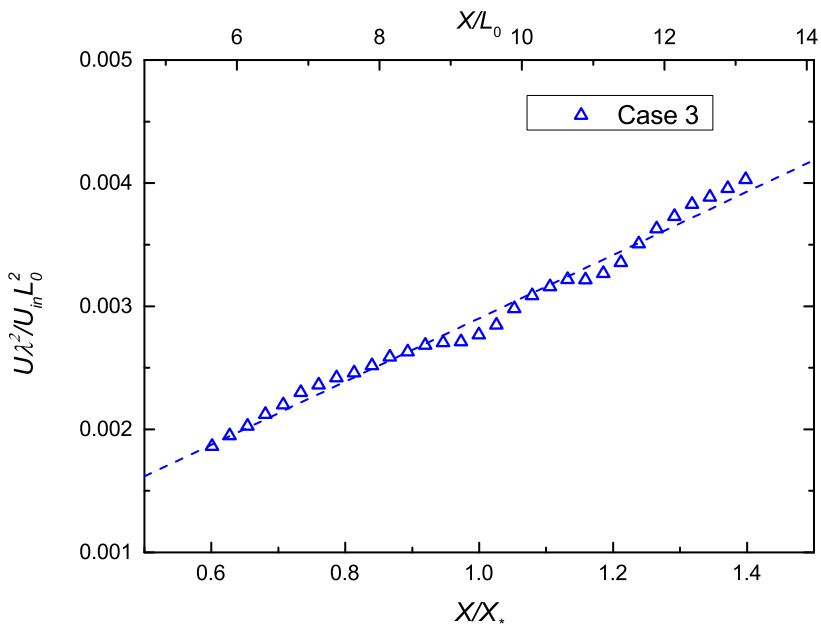

Figure 5.5: Streamwise evolution of $U\lambda^2/U_{in}L_0^2$ along the centerline and the corresponding linear fit (dashed line) for single square grid with additional turbulence (case 3).

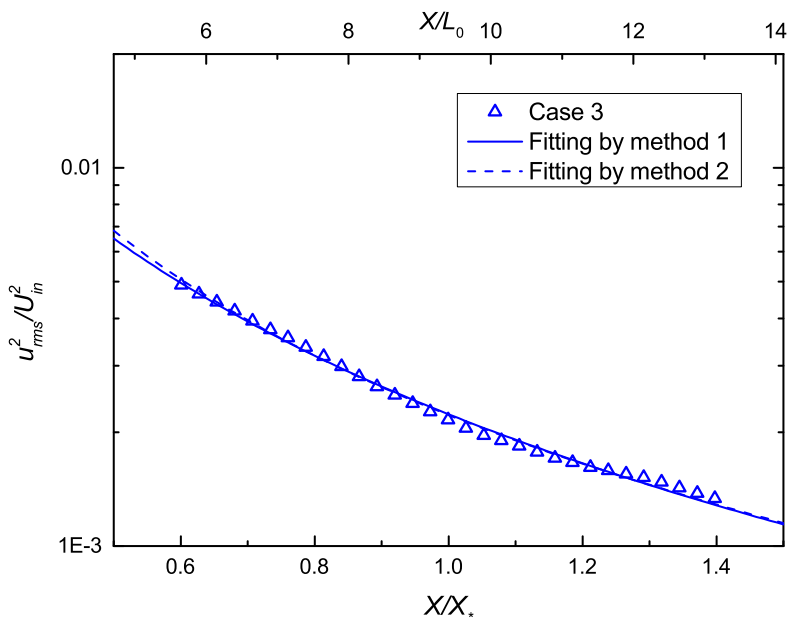

Figure 5.6: Streamwise evolution of kinetic energy along the centerline and the power law fit using method 1 (solid line) and method 2 (dashed line) for single square grid with additional turbulence (case 3).

5.3 Summary of Fractal-Generated Turbulence

A typical fractal square grid consists of various-size square grids that are self-similar. In the light of above discussion in chapters 3–5, the fractal square grid can effectively be split into two parts: a main part containing the largest square grid and a supplementary part containing smaller fractal iterations. The roles of each part are discussed here.

5.3.1 Largest Square Grid

The influence of the largest square grid persists for a much longer streamwise distance than that of the smaller grids. Turbulence characteristics (e.g., λ, u_{rms}, and Re_λ) at $X/X_* = 1.4$ ($X/L_0 = 13.16$) are mainly determined by the largest wake interactions. In chapter 4, we demonstrate that L_0 gives a physical description of the fractal square grid; note that L_0 is usually taken to be half the size of the whole fractal square grid. In contrast, a regular grid contains a considerably larger number of meshes to ensure homogeneity. Therefore, for a given wind tunnel, L_0 is much larger than the M of a regular grid. Under the same U_{in} conditions, a fractal square grid can have a much larger inlet Reynolds number because of the remarkably large value of L_0. Therefore, it is not surprising that the fractal square grid produces a high Re_λ and high turbulent energy levels that are comparable to those of the active grid.

In addition, this large L_0 leads to an extended production region in which turbulence intensities increase and peak. It should be noted that even though there is usually only one largest square grid in the fractal square grid reasonable homogeneity and isotropy in the downstream region was seen in our simulations and has been reported in previous studies.[23,25,26,28] This is partly due to the existence of smaller wake interactions immediately behind the grid.

5.3.2 Small Fractal Iterations

In regard to the small fractal iterations, we can make the following conclusions. The existence of the small fractal square grids can greatly increase the blockage

ratio, and behind grids with a relatively large blockage ratio, more severely sheared turbulent flow and stronger wake interactions are expected. Hence, the significantly higher turbulence intensity close to the fractal square grid is not surprising.

Furthermore, additional turbulence generated by the smaller grids can affect the development of the largest wakes. It is well known that turbulence generated by small-wake interactions appear in the vicinity immediately behind the grid, whereas those of the largest wakes occur further downstream. Hence, the largest wakes are surrounded by additional turbulence (see Fig. 5.7), and this additional turbulence leads to stronger largest-wake interactions and contributes to the fluctuation levels in the near-field region. Krogstad and Davidson[17] demonstrated that multiscale grids generate distinctly higher turbulence levels in the near-field region when compared to those generated by a regular grid with the same blockage ratio. Thus, we can safely conclude that in addition to the effects of a high blockage ratio, the distinctly higher fluctuation levels and mixing performance of the fractal square grid, shown in Figs. 4.3, 4.5, and 4.6, are also partly due to the additional turbulence.

Moreover, small fractal iterations provide a high mixing rate in the region close to the grid. In fact, Krogstad and Davidson[17] demonstrated that in the near-field region, a higher mixing performance is found behind multiscale grids. In this chapter, we confirm the above assumption and study the possible influences of the additional turbulence via an additional simulation (case 3).

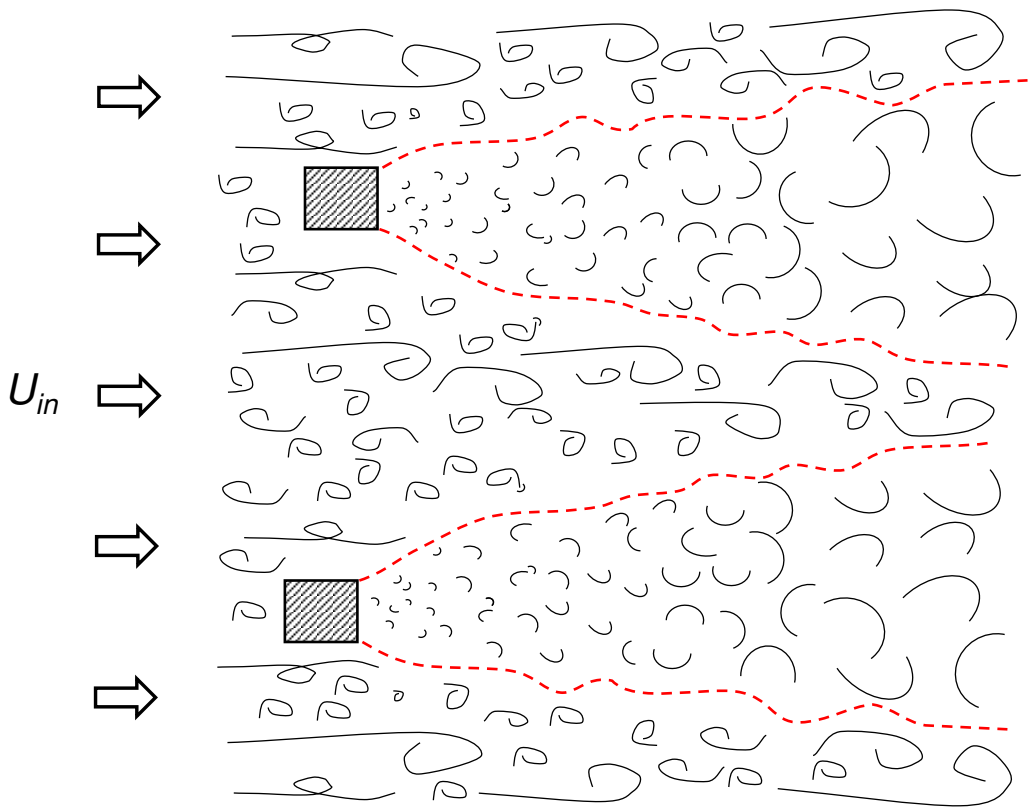

Figure 5.7: General schematic of the wake interactions behind a fractal square grid.

Chapter 6

Conclusions and Future Prospects

6.1 Conclusions

We perform simulations of turbulence generated by the fractal and single square grids with the uniform inlet velocity. Moreover, a third simulation, that of turbulence generated by a single square grid subject to additional artificial turbulence (homogeneous isotropic turbulence with $u_{rms,et}/U_{in} = 0.097$), is also carried out. In Chapter 2, the numerical details and the flow conditions are presented. The main research contributions of this thesis can be summarized as follows.

In chapter 3, we numerically investigate the turbulence generated by the single square grid. The main findings drawn from the simulation in this chapter can be summarized as follows.

1. For the single square grid with mean inlet velocity, the intensity u_{rms}/U reaches its maximum value at $X_{peak} \simeq 0.45X_*$, which is similar to the corresponding value for the fractal square grid. Hence, we confirm the hypothesis proposed by Mazellier and Vassilicos that for the fractal square grid, the location of turbulence intensity peak X_{peak} is largely determined by the scale of the largest grid bar.

2. Fluid motions at $X/X_* \simeq 0.2$ ($X/L_0 \simeq 1.88$ in the present case) are strongly dependent on the wake interactions generated by the grid bar. The similar characteristic for turbulent flow generated by the fractal square grid indicates the dominant effects of the interactions of the largest wakes at $X/X_* \simeq 0.2$.

3. The intermittent factor γ shows that the wake interactions begin at $X/X_* \simeq$

0.1 ($X/L_0 \simeq 0.94$ in the present case) downstream of the grid. And the intermittent factor γ approaches 1 at $X/X_* \simeq 0.4$ ($X/L_0 \simeq 3.76$ in the present case).

4. Behind the single square grid, the (R, Q) and (Q_W, Q_S) maps suggest that at $X/X_* < 0.2$ ($X/L_0 < 1.88$), the fluid motions are distinctly different from those of turbulent channel flows, turbulent mixing layers, and isotropic turbulence. With the spatial development, the joint PDFs of the (Q, R) and $(Q_W, -Q_S)$ maps at $X/X_* = 0.4$ ($X/L_0 = 3.76$) adopt their well known shapes.

In chapter 4, we perform the simulation of turbulence generated by the fractal square grid. For the fractal-generated turbulence, we can draw the following conclusions.

1. A fractal square grid contains two parts, the main part (largest square grid) and the supplement part (relatively small ones). The influences of the supplement part only last for a short distance from the grid, whereas the largest square grid mainly determines the turbulence characteristics in the downstream region.

2. Our simulation results confirm the existence of the high energy decay region behind the fractal square, where turbulence has unusual high decay exponent n.

3. A fractal square grid can indeed stir higher turbulence levels in the near field region, whereas the values of Re_λ and u_{rms}/U_{in} of the single and fractal square grids at the end of simulation section (i.e., $X/X_* = 1.4$ or $X/L_0 = 13.2$) are comparable. The widely held belief that the fractal square grid can generate unconventional high levels of turbulence fluctuations is related to the improper use of the effective mesh size M_{eff}.

In chapter 5, we propose that a typical fractal square grid, which consists of various-size square grids that are self-similar, can effectively be split into two parts: a main part containing the largest square grid and a supplementary part containing smaller fractal iterations. Turbulence because a supplementary part can be regarded as the additional turbulence. To confirm this hypothesis, we perform an additional simulation, that is the simulation of turbulence generated by a single square grid with additional artificial turbulence. The main findings are as follows.

1. With the inclusion of additional homogeneous isotropic turbulence ($u_{rms,et}/U_{in} = 0.097$), the turbulence behind the single square grid has similar characteristics to

fractal-generated turbulence (e.g., a faster wake decay rate, small value of X_{peak}/L_0, excellent agreement of λ/L_0, and high energy decay rate).

2. The fractal square grid can be regarded as an efficient additional turbulence generator in the near field region.

6.2 Future Prospects

In this work, physical characteristics of turbulent flows behind the single and fractal square grids are thorough studied. Also a conceptual model for multiscale/fractal grid is proposed to explain the unusual behavior of the fractal-generated turbulence.

The joint PDFs of the invariants R and Q is a useful tool to investigate the instantaneous characteristics of fluid motions. In this thesis, we investigate the variation of the joint PDFs of R and Q along the centerline behind the single square grid. Note that the evolution of the invariants of R and Q is important to obtain the dynamic information of turbulent flows.

In our future work, we will study the conditional mean trajectories (CMTs) of R and Q of the single-square grid-generated turbulence. By now, the investigations of the evolution of the invariants R and Q are limited in the turbulent flows, in which the joint PDFs of R and Q exhibit the well-known "teardrop" shape in the R–Q plane.[83–88] It is interesting to explore the Lagrangian dynamics of turbulence, in which the "teardrop" shape does not appear. Note that the joint PDFs of R and Q at $X/X_0 = 0.04$ and 0.1 (X/L_0= 0.38 and 0.94) are quite similar to the ones observed at the T/NT interface of free shear flows (e.g., mixing layer, wake, and jet); at the T/NT interface, the fluid motions are also characterized by the dominance of irrotational dissipation. Hence, we expect that the future investigation concerning the CMTs of the invariants in the single-square grid-generated turbulence can also contribute to a better understanding of the characteristics at T/NT interface of free shear flows.

Acknowledgements

I must thank my supervisor, Prof. Sakai. The completion of this thesis is impossible for me without his support and encouragement. I owe my deepest gratitude to Nagata sensei for his helpful suggestions through my time in Nagoya University. He is a supportive advisor and I really learned a lot from the invaluable discussions with him. It is my great honor to perform my Ph.D. studies under the supervision of Prof. Sakai and Nagata sensei. I would like to thank all group members at Statistical Fluid Engineering Laboratory. I am also grateful to Prof. Ishii and Prof. Sasoh for reviewing this thesis and for their valuable comments.

I acknowledge Dr. R. Onishi from Japan Agency for Marine-Earth Science and Technology for offering his simulation results. I would like to thank the Institute of Fluid Science of Tohoku University for providing computational resource. I thank valuable comments from Professor J. C. Vassilicos and Dr. S. Laizet (Imperial College London) on this study.

At last, I would like to acknowledge the financial support provided by the Chinese Scholarship Council (CSC).

Bibliography

[1] A. S. Monin and A. M. Yaglom, *Statistical Fluid Mechanics. Vol. 2* (MIT Press, 1975).

[2] G. I. Taylor, "Statistical theory of turbulence," Proc. R. Soc. London, Ser. **A151**, 421 (1935).

[3] G. K. Batchelor, *The theory of homogeneous turbulence* (Cambridge University Press, 1953).

[4] A. N. Kolmogorov, "Energy dissipation in locally isotropic turbulence," Dokl. Akad. Nauk SSSR **32**, 19 (1941).

[5] L. F. Loitsiantskii, "Some basic laws of isotropic turbulent flow," Cent. Aero. Hydro. Inst. Moscow, 440 (1939).

[6] A. N. Kolmogorov, "Local structure of turbulence in an incompressible fluid for very large Reynolds numbers," Dokl. Akad. Nauk SSSR **30**, 19 (1941).

[7] K. Kaneda, T. Ishihara, M. Yokokawa, K. Ikatura, and A. Uno, "Energy dissipation rate and energy spectrum in high resolution direct numerical simulations of turbulence in a periodic box," Phys. Fluids **15**, L21 (2003).

[8] T. Ishida, P. A. Davidson, and Y. Kaneda, "On the decay of isotropic turbulence," J. Fluid Mech. **564**, 455 (2006).

[9] T. Ishihara, T. Gotoh, and Y. Kaneda, "Study of high Reynolds number isotropic turbulence by direct numerical simulation," Annu. Rev. Fluid Mech. **41**, 65 (2009).

[10] P A. Davidson, *Turbulence: An Introduction for Scientists and Engineers: An Introduction for Scientists and Engineers* (Oxford University Press, 2004).

[11] S. A. Orszag and G. S. Patterson, Jr., "Numerical simulation of threedimensional homogeneous isotropic turbulence," Phys. Rev. Lett. **28**, 76 (1972).

[12] G. Comte-Bellot and S. Corrsin, "The use of a contraction to improve isotropy in grid-generated turbulence," J. Fluid Mech. **25**, 657 (1966).

[13] G. Comte-Bellot and S. Corrsin, "Simple Eulerian time correlation of full and narrow-band velocity signals in grid-generated isotropic turbulence," J. Fluid Mech. **48**, 273 (1971).

[14] P.-Å. Krogstad and P. A. Davidson, "Is grid turbulence Saffman turbulence?" J. Fluid Mech. **642**, 373 (2010).

[15] P. Lavoie, L. Djenidi, and R. A. Antonia, "Effects of initial conditions in decaying turbulence generated by passive grids," J. Fluid Mech. **585**, 395 (2007).

[16] T. Kitamura, K. Nagata, Y. Sakai, A. Sasoh, O. Terashima, and T. Harasaki, "On invariants in grid turbulence at moderate Reynolds numbers," J. Fluid Mech. **738**, 378 (2014).

[17] P.-Å. Krogstad and P. A. Davidson, "Near-field investigation of turbulence produced by multi-scale grids," Phys. Fluids **24**, 035103 (2012).

[18] H. Mikata, "Realization of a large-scale turbulence field in a small wind tunnel," Fluid Dyn. Res. **8**, 53 (1991).

[19] S. Corrsin, *Turbulence: Experimental methods* (Springer, 1963).

[20] J. Tan-Atichat, H. M. Nagib, and R. I. Loehrke, "Interaction of free-stream turbulence with screens and grids: a balance between turbulence scales," J. Fluid Mech. **114**, 501 (1982).

[21] Ö. Ertunç, N. Özyilmaz, H. Lienhart, F. Durst, and K. Beronov, "Homogeneity of turbulence generated by static-grid structures," J. Fluid Mech. **654**, 473 (2010).

[22] H. Tennekes, J. L. Lumley, *A first course in turbulence* (MIT press, 1972)

[23] D. Hurst and J. C. Vassilicos, "Scalings and decay of fractal-generated turbulence," Phys. Fluids **19**, 035103 (2007).

[24] R. E. Seoud and J. C. Vassilicos, "Dissipation and decay of fractal-generated turbulence," Phys. Fluids **19**, 105108 (2007).

[25] N. Mazellier and J. C. Vassilicos, "Turbulence without Richardson–Kolmogorov cascade," Phys. Fluids **22**, 075101 (2010).

[26] P. C. Valente and J. C. Vassilicos, "The decay of turbulence generated by a class of multiscale grids," J. Fluid Mech. **687**, 300 (2011).

[27] R. Gomes-Fernandes, B. Ganapathisubramani, and J. C. Vassilicos, "Particle image velocimetry study of fractal-generated turbulence," J. Fluid Mech. **711**, 306 (2012).

[28] K. Nagata, Y. Sakai, T. Inaba, H. Suzuki, O. Terashima, and H. Suzuki, "Turbulence structure and turbulence kinetic energy transport in multiscale/fractal-generated turbulence," Phys. Fluids **25**, 065102 (2013).

[29] L. F. G. Simmons and M. A. Salter, "Experimental investigation and analysis of the velocity variations in turbulent flow," Proc. R. Soc. London, Ser. A **145**, 212 (1934).

[30] M. S. Mohamed and J. LaRue,"The decay power law in grid-generated turbulence," J. Fluid Mech. **219**, 195 (1990).

[31] R. Stresing, J. Peinke, R. E. Seoud, and J. C. Vassilicos, "Defining a new class of turbulent flows," Phy. Rev. Lett. **104**, 194501 (2010).

[32] P.-Å. Krogstad and P. A. Davidson, "Freely decaying, homogeneous turbulence generated by multi-scale grids," J. Fluid Mech. **680**, 417 (2011).

[33] P. C. Valente and J. C. Vassilicos, "Universal dissipation scaling for non-equilibrium turbulence," Phys. Rev. Lett. **108**, 214503 (2012).

[34] K. Nagata, H. Suzuki, Y. Sakai, T. Hayase, and T. Kubo, "Direct numerical simulation of turbulence characteristics generated by fractal grids," Int. Rev. Phys. **2**(6), 400 (2008).

[35] K. Nagata, H. Suzuki, Y. Sakai, and T. Hayase, "Direct numerical simulation around complex geometries and scalar transfer using the immersed boundary method and fully conservative higher-order finite-difference schemes," *Numerical Simulations, Applications, Examples and Theory* (INTECH 2010), Chap. 3.

[36] H. Suzuki, K. Nagata, Y. Sakai, and T. Hayase, "Direct numerical simulation of turbulent mixing in regular and fractal grid turbulence," Phys. Scr. **T142**, 014065 (2010).

[37] H. Suzuki, K. Nagata, Y. Sakai, T. Hayase, Y. Hasegawa, and T. Ushijima "Direct numerical simulation of fractal-generated turbulence," Fluid Dyn. Res. **45**, 061409 (2013).

[38] S. Laizet and J. C. Vassilicos, "Multiscale generation of turbulence," J. Multiscale Modelling **1**(1), 177 (2009).

[39] S. Laizet, E. Lamballais, and J. C. Vassilicos, A numerical strategy to combine high-order schemes, complex geometry and parallel computing for high resolution DNS of fractal generated turbulence," Comput. Fluids **39**, 471 (2010).

[40] S. Laizet and J. C. Vassilicos, "DNS of fractal-generated turbulence," Flow, Turbul. Combust. **87**, 673 (2011).

[41] S. Laizet and J. C. Vassilicos, "Fractal space-scale unfolding mechanism for energy-efficient turbulent mixing," Phys. Rev. E **86**, 046302 (2012).

[42] S. Laizet, J. C. Vassilicos, and C. Cambon, "Interscale energy transfer in decaying turbulence and vorticity-strain-rate dynamics in grid-generated turbulence," Fluid Dyn. Res. **45**, 061408 (2013).

[43] H. Suzuki, K. Nagata, Y. Sakai, and R. Ukai, "High-Schmidt-number scalar transfer in regular and fractal grid turbulence," Phys. Scr. **T142**, 014069 (2010).

[44] H. Suzuki, K. Nagata, Y. Sakai, and Y. Hasegawa, "Fractal analysis of turbulent mixing in fractal-generated turbulence by PLIF," Phys. Scr. **T155**, 014062 (2013).

[45] N. Soulopoulos, J. Kerl, T. Sponfeldner, F. Beyrau, Y. Hardalupas, A. M. K. P. Taylor, and J. C. Vassilicos, "Turbulent premixed flames on fractal-grid-generated turbulence," Fluid Dyn. Res. **45**, 061404 (2013).

[46] F. C. G. A. Nicolleau, S. M. M. Salim, and A. F. Nowakowski, "Experimental study of a turbulent pipe flow through a fractal plate," J. Turbul. **12**, N44 (2011).

[47] J. Nedić, B. Ganapathisubramani, J. C. Vassilicos, J. Borée , L. Brizzi, and A. Spohn, "Aeroacoustic performance of fractal spoilers," AIAA J. **50**(12), 2695 (2012).

[48] C. J. Keylock, K. Nishimura, M. Nemoto, and Y. Ito, "The flow structure in the wake of a fractal fence and the absence of an inertial regime," Environ. Fluid Mech. **12**, 227 (2012).

[49] Y. Zhou, K. Nagata, Y. Sakai, H. Suzuki, Y. Ito, O. Terashima, and T. Hayase, "Development of turbulence behind the single square grid," Phys. Fluids **26**, 045102 (2014).

[50] Y. Zhou, K. Nagata, Y. Sakai, H. Suzuki, Y. Ito, O. Terashima, and T. Hayase, "Relevance of turbulence behind the single square grid to turbulence generated by regular- and multiscale-grids," Phys. Fluids **26**, 075105 (2014).

[51] Y. Morinishi, T. S. Lund, O. V. Vasilyev, and P. Moin, "Fully Conservative Higher Order Finite Difference Schemes for Incompressible Flow," J. Comput. Phys. **143**, 90 (1998).

[52] T. Kajishima, "Finite-difference method for convective terms using non-uniform grid," Trans. JSME, Series B, **65**, 1607 (1999) (in Japanese).

[53] S. K. Lele, "Compact finite difference schemes with spectral-like resolution," J. Comput. Phys. **103**, 16 (1992).

[54] H. Suzuki, K. Nagata, Y. Sakai, T. Hayase, Y. Hasegawa, and T. Ushijima, "An attempt to improve accuracy of higher-order statistics and spectra in direct numerical simulation of incompressible wall turbulence by using the compact schemes for viscous terms," Int. J. Numer. Meth. Fluids **73**, 509 (2013).

[55] H. Le and P. Moin, "An improvement of fractional step methods for the incompressible Navier-Stokes equations," J. Comput. Phys. **92**, 369 (1991).

[56] P. Moin, *Fundamentals of engineering numerical analysis* (Cambridge University Press, Cambridge, 2010).

[57] S. Laizet, J. Nedić, and J. C. Vassilicos, "Influence of the spatial resolution on fine-scale features in DNS of turbulence generated by a single square grid," Comput. Fluids (submitted).

[58] X. Wu and P. Moin, "A direct numerical simulation study on the mean velocity characteristics in turbulent pipe flow," J. Fluid Mech. **608**, 81 (2008).

[59] A. A. Townsend, *The Structure of Turbulent Shear Flows* (Cambridge University Press, Cambridge, 1956).

[60] S. Komori and K. Nagata, "Effects of molecular diffusivities on counter-gradient scalar and momentum transfer in strongly stable stratification," J. Fluid Mech. **326**, 205 (1996).

[61] S. Komori, K. Nagata, T. Kanzaki, and Y. Murakami, "Measurements of Mass Flux in a Turbulent Fluid Flow with a Chemical Reaction," AIChE J. **39**, 1611 (1993).

[62] P. C. Valente and J. C. Vassilicos, "The non-equilibrium region of grid-generated decaying turbulence," J. Fluid Mech. **744**, 5 (2014).

[63] A. Tsinober, E. Kit, and T. Dracos, "Experimental investigation of the field of velocity gradients in turbulent flows," J. Fluid Mech. **242**, 169 (1992).

[64] D. K. Bisset, J. C. R. Hunt, and M. M. Rogers, "The turbulent/nonturbulent interface bounding a far wake," J. Fluid Mech. **451**, 383 (2002).

[65] C. B. da Silva and J. C. F. Pereira, "Invariants of the velocity-gradient, rate-of-strain, and rate-of-rotation tensors across the turbulent/nonturbulent interface in jets," Phys. Fluids **20**, 055101 (2008).

[66] A. Ooi, J. Martin, J. Soria, and M. Chong, "A study of the evolution and characteristics of the invariants of the velocity-gradient tensor in isotropic turbulence," J. Fluid Mech. **381**, 141 (1999).

[67] H. Blackburn, N. Mansour, and B. Cantwell, "Topology of fine-scale motions in turbulent channel flow," J. Fluid Mech. **310**, 269 (1996).

[68] J. Soria, R. Sondergaard, B. Cantwell, M. Chong, and A. Perry, "A study of the fine-scale motions of incompressible time-developing mixing layers," Phys. Fluids **6**, 871 (1994).

[69] R. Onishi, Y. Baba, and K. Takahashi, "Large-scale forcing with less communication in finite-difference simulations of stationary isotropic turbulence," J. Comput. Phys. **230**, 4088 (2011).

[70] Y. Dubief and F. Delcayre, "On coherent-vortex identification in turbulence," J. Turbul. **1**, N11 (2000).

[71] N. Okamoto, K. Yoshimatsu, K. Schneider, M. Farge, and Y. Kaneda, "Coherent vortices in high resolution direct numerical simulation of homogeneous, isotropic turbulence: A wavelet viewpoint," Phys. Fluids **19**, 115109 (2007).

[72] R. Rogallo, "Numerical experiments in homogeneous turbulence," NASA Tech. Memo. **176**, 81315 (1981).

[73] E. Johnsen, J. Larsson, A. V. Bhagatwala, W. H. Cabot, P. Moin, P. S. Rawat, S. K. Shankar, B. Sjogreen, H. C. Yee, X. Zhong, and S. K. Lele, " Assessment of high-resolution methods for numerical simulations of compressible turbulence with shock waves," J. Comput. Phys. **229**, 1213 (2010).

[74] M. Klein, A. Sadiki, and J. Janicka, "A digital filter based generation of inflow data for spatially developing direct numerical or large eddy simulations," J. Comput. Phys. **186**, 652 (2003).

[75] S. Lee, S. K. Lele, and P. Moin, "Simulation of spatially evolving turbulence and the applicability of Taylors hypothesis in compressible flow," Phys. Fluids A **4**, 1521 (1992).

[76] J. S. Wu and G. M. Faeth, "Sphere wakes at moderate Reynolds numbers in a turbulent environment," AIAA J. **32**, 535 (1994).

[77] J. S. Wu and G. M. Faeth, "Effect of ambient turbulence intensity on sphere wakes at intermediate Reynolds numbers," AIAA J. **33**, 171 (1995).

[78] D. Legendre, A. Merle, and J. Magnaudet, "Wake of a spherical bubble or a solid sphere set fixed in a turbulent environment," Phys. Fluids **18**, 048102 (2006).

[79] Z. Amoura, V. Roig, F. Risso, and A. M. Billet, "Attenuation of the wake of a sphere in an intense incident turbulence with large length scales," Phys. Fluids **22**, 055105 (2010).

[80] I. Eames, P. B. Johnson, V. Roig, and F. Risso, "Effect of turbulence on the downstream velocity deficit of a rigid sphere," Phys. Fluids **23**, 095103 (2011).

[81] I. Eames, C. Jonsson, and P. B. Johnson, "The growth of a cylinder wake in turbulent flow, J. Turbul. **12**, N39 (2011).

[82] E. Rind and I. P. Castro, Direct numerical simulation of axisymmetric wakes embedded in turbulence," J. Fluid Mech. **710**, 482 (2012).

[83] J. Martín, A. Ooi, S. Chong, and J. Soria, "Dynamics of the velocity gradient tensor invariants in isotropic turbulence," Phys. Fluids **10**, 2336 (1998).

[84] A. Ooi, J. Martin, J. Soria, and M. Chong, "A study of the evolution and characteristics of the invariants of the velocity gradient tensor in isotropic turbulence," J. Fluid Mech. **381**, 141 (1999).

[85] B. Lüthi, M. Holzner, A. Tsinober, "Expanding the Q-R space to three dimensions," J. Fluid Mech. **641**, 497 (2009).

[86] G. E. Elsinga and I. Marusic, "Evolution and lifetimes of flow topology in a turbulent boundary layer," Phys. Fluids **22**, 015102 (2010).

[87] C. Atkinson, S. Chumakov, I. Bermejo-Moreno, and J. Soria, "Lagrangian evolution of the invariants of the velocity gradient tensor in a turbulent boundary layer," Phys. Fluids **24**, 105104 (2012).

[88] Y. B. Chu and X. Y. Lu "Topological evolution in compressible turbulent boundary layers," J. Fluid Mech. **733**, 414 (2013).